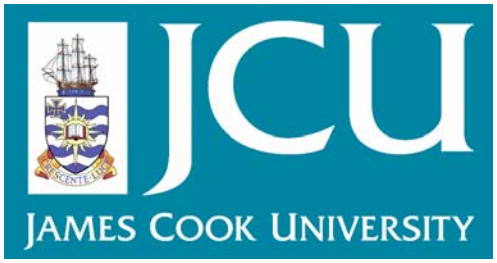

AN ANALYTICAL AND EXPERIMENTAL INVESTIGATION OF ACTIVE VIBRATION CONTROL TECHNIQUES ON COUPLED PLATE STRUCTURES

Thesis submitted by

John Keir BEng(Hons) QLD

in June 2004

For the degree of Doctor of Philosophy

In the School of Engineering

James Cook University

STATEMENT OF ACCESS

I, the undersigned, the author of this thesis, understand that James Cook University will make it available for use within the University Library and, via the Australian Digital Thesis network, for use elsewhere.

I understand that, as an unpublished work, a thesis has significant protection under the Copyright Act and;

I do not wish to place any further restriction on access to this work.

…….. ……..……...

Signature Date

STATEMENT OF SOURCES

DECLARATION

I declare that this thesis is my own work and has not been submitted in any form for another degree or diploma at any university or other institution of tertiary education. Information derived from the published or unpublished work of others has been acknowledged in the text and a list of references given.

…….. ……..……...

Signature Date

ELECTRONIC COPY

I, the undersigned, the author of this work, declare that the electronic copy of this thesis provided to the James Cook University Library is an accurate copy of the print thesis submitted, within the limits of the technology available.

…….. ……..……...

Signature Date

CONTRIBUTIONS

Financial support for this work from the Australian Research Council, Australian Defence Science and Technology Organisation, Maritime Platforms Division and NQEA are gratefully acknowledged.

ACKNOWLEDGEMENTS

Firstly I would like to thank my entire family for their support and encouragement during my entire schooling life. Without it I would not be where I am today. Thank you so much.

I am also greatly indebted to my supervisor Dr Nicole Kessissoglou. I would like to thank her for her continuous help over the last few years with my study.

Finally I would like to thank Stu Peterson for his help with the experimental set-up.

ABSTRACT

This PhD thesis presents a theoretical and experimental investigation using active control to attenuate the vibration responses associated with coupled plate structures. Three plate structures were examined, which corresponded to an L, T and X shaped plate. The plate theory used to determine the dynamic and controlled responses of the coupled plate structures is presented for a generic structure consisting of four finite plates joined together at right angles in a X-shape. The theory for active vibration control of the coupled plate using single and multiple control actuators and error sensors is also presented for both dependent and independent control.

The use of multiple actuators and error sensors in various arrangements to attenuate the response of various coupled plate structures is demonstrated. The number and location of the control forces and error sensors are varied, and their effects on the control performance are compared. In addition, the effect of the control forces driven dependently and independently was investigated. For active control at discrete resonance frequencies, the global response of the structure was observed. Experiments were conducted in order to validate theoretical results on the active control of the global response at a low resonance frequency. The results showed excellent correlation, validating the effectiveness of the active control application.

An energy method to predict the vibrational response and its transmission between coupled structures in the medium to high frequency ranges is Statistical Energy Analysis (SEA). In

this thesis, SEA is used to model several built-up structures and estimate their vibrational response using energy flow relationships. Energy levels of the L, T, X-shaped plates, and a 7-plate structure, predicted from the exact analytical waveguide model are compared with those of conventional SEA models. A hybrid approach between the two techniques is also presented. The hybrid method uses the analytical waveguide method to estimate the input power and coupling loss factors used in the conventional SEA equations. The energy levels in individual plate subsystems using the exact analytical method, SEA, and the hybrid technique are compared.

TABLE OF CONTENTS

LIST OF TABLES

LIST OF FIGURES

Figure 4.35. Contour plot of the controlled response at 53.13Hz for one control force at (x_{s1}, y_{s1}) = (0.371, 0.31) and an error sensor located on plate 2 at (x_{e1}, y_{e1}) = (0.43, 0.375).

Figure 4.36. Contour plot of the controlled response at 53.13Hz for two dependently driven control forces at (x_{s1}, y_{s1}) = (0.371, 0.25), (x_{s2}, y_{s2}) = (0.371, 0.31) and two error sensors located on plate 2 at (x_{e1}, y_{e1}) = (0.23, 0.19) and (x_{e2}, y_{e2}) = (0.23, 0.31).

Figure 4.37. Contour plot of the controlled response at 53.13Hz for two dependently driven control forces at (x_{s1}, y_{s1}) =(0.371, 0.25), (x_{s2}, y_{s2}) = (0.371, 0.31) and two error sensors located on plate 2 at (x_{e1}, y_{e1}) = (0.23, 0.25) and (x_{e2}, y_{e2}) = (0.28, 0.25).

Figure 4.38. Contour plot of the controlled response at 53.13Hz for two independently driven control forces at (x_{s1}, y_{s1}) = (0.371, 0.25), (x_{s2}, y_{s2}) = (0.371, 0.31) and two error sensors located on plate 2 at (x_{e1}, y_{e1}) = (0.23, 0.25) and (x_{e2}, y_{e2}) = (0.28, 0.25).

Figure 4.39. Primary (solid line) and controlled frequency responses for the X-shaped plate using primary and control forces located at (x_p, y_p) = (0.371, 0.19) and (x_{s1}, y_{s1}) = (0.371, 0.31) respectively, for an error sensor located on plate 2 at (x_{e1}, y_{e1}) = (0.23, 0.25) (dashed line), or two error sensors located on plate 2 at (x_{e1}, y_{e1}) = (0.36, 0.4) and (x_{e2}, y_{e2}) = (0.23, 0.25) (dotted line).

LIST OF SYMBOLS

ω	Angular frequency	[rad/s]
ρ	Material density	[kg/m^3]
v	Poisson's ratio	
η	Structural loss factor	
η_{ij}	Coupling loss factor	
$n(\omega)$	Modal density	[modes.s/rad]
σ	Plate thickness ratio	
$\langle \tau_{ij} \rangle$	Power transmission coefficient	
$[\alpha_p]$, $[\alpha_s]$	Matrices of the primary and secondary flexural displacements	
$[\mathbf{X}]$	Coefficient matrix	
$[\mathbf{F_p}]$, $[\mathbf{F_s}]$	Force matrices	
A_i, B_i, C_i, D_i	Coefficients of the plate flexural propagating and near field waves for forced vibration	
c_B	Phase velocity	[m/s]
c_L	Longitudinal wave speed	[m/s]
c_g	Group velocity	[m/s]
D	Flexural rigidity of the plate	[Nm]
E	Young's modulus	[N/m^2]
E	Energy stored in the subsystem.	[J]
E_k	Kinetic energy	[Nm]
f	Frequency	[Hz]
F_p	Magnitude of the primary force	[N]
F_s	Magnitude of the secondary force	[N]
$F_s\|_{opt}$	Optimal control force amplitude	[N]
G_p, G_s	Primary and secondary transfer functions	[m/N]
h	Plate thickness	[m]
k_x, k_y, k_n, k_p,	Wave numbers	[1/m]
L	Length of the junction line	[m]

L_a	Acceleration level, reference level $a_{ref} = 10^{-6}$ m/s^2	[dB]
L_{xi}	Length of the plate along the x-axis	[m]
L_y	Length of the plate along the y-axis	[m]
m, m'	Mode number	
M	Mass of each individual plate	[kg]
M_x	Bending moment	[Nm]
M_{xy}	Twisting moment	[Nm]
N_x	Longitudinal force	[N]
P_{in}	Input power	[J]
P_{dis}	Dissipated energy	[J]
P_{ij}	Energy flow from subsystem i to subsystem j	[J]
Q_x	Net vertical shear force	[N]
F_x	Bending shear force	[N]
S_i	Surface area of the subsystem i	[m^2]
u	Longitudinal displacement of the plate	[m]
w_p	Displacement due to primary force	[m]
w_s	Displacement due to secondary force	[m]
w_{tot}	Total displacement due to primary and secondary forces	[m]
x_e	x co-ordinate for the error sensor	[m]
x_p	x co-ordinate for the primary force	[m]
x_s	x co-ordinate for the secondary force	[m]
y_e	y co-ordinate for the error sensor	[m]
y_p	y co-ordinate for the primary force	[m]
y_s	y co-ordinate for the secondary force	[m]
Z	Impedance of an infinite plate	[kg/s]

CHAPTER 1

INTRODUCTION AND LITERATURE REVIEW

1.1 Introduction

Structural vibration control is an important concern in engineering industries such as the automotive, aerospace and maritime industries, and in refineries and manufacturing plant. The basic idea of vibration control is to reduce or modify the vibration of a mechanical system. Reducing vibration can lead to a lowering of noise and dynamic stress of a system. Dynamic stress can lead to problems such as fatigue or failure of the structure or machine, energy dissipation, reduced reliability, and poor performance. Vibrations in simple structures such as beams and plates can travel as flexural, extensional or torsional waves, or combinations thereof. These waves transfer energy to other components of the system coupled to the structure. This may result in an undesirable system response or structure-borne sound radiation. Simple beam, plate and shell type structures are common components in many engineering systems such as ship hulls, building structures, aeroplanes, machine casing and various other mechanical equipment. In the aerospace industry, the reduction of structure-borne interior cabin noise allows for greater passenger comfort, and can be achieved by reducing the vibrations along the aircraft panelling, which is predominantly made up of thin curved plates. In the case of maritime vessels, the propulsion system and on-board machinery such as the diesel engines and gearboxes, generate substantial vibrations, which are then transmitted through the ship's hull. These vibrations may result in structural fatigue, damage to onboard equipment, and significant noise radiation. The characteristics of the

vibration transmission and active vibration control can be studied by investigating coupled plate structures.

This PhD thesis presents a theoretical and experimental investigation using active control to attenuate the responses associated with coupled plate structures. The use of multiple actuators and error sensors in various arrangements to attenuate the response of various coupled plate structures is demonstrated. The number and location of the control forces and error sensors are varied, and their effects on the control performance are compared. In addition, the effect of the control forces driven dependently and independently was investigated. For active control at discrete resonance frequencies, the global response of the structure was observed. Experiments were conducted in order to validate theoretical results on the active control of the global response at a low resonance frequency. Numerical results of the vibration levels obtained from the exact analytical waveguide method were compared with those of the conventional statistical energy analysis (SEA) model. A hybrid approach between the two methods is also introduced.

1.2 Research Overview

Chapter 1 presents a literature review on the dynamic response and active control of various engineering structures. Material from the literature relating to various experimental configurations used for active control and optimisation techniques for the control force and error sensor numbers and locations is also presented. Chapter 1 also gives a brief overview of statistical energy analysis and its importance in vibration control.

Chapter 2 presents the theory for the dynamic and controlled response of a variety of coupled plate structures subject to point force excitation. The theory is presented for a generic structure consisting of four finite plates joined together at right angles in a cross-shape. Active control of plate structures using single and multiple control actuators and error sensors is also presented for independent and dependent control.

Chapter 3 presents an experimental study of the dynamic response and active control of the thin rectangular coupled plates as described in Chapter 2. This chapter initially deals with the basic principles of a feedforward active control arrangement. The experimental procedure including rig and apparatus used are also detailed.

Chapter 4 presents the results from the computational modelling of the plate structures using the theory introduced in Chapter 2. Matlab programs are used to determine the response of the structures subject to a point force excitation and for various active control arrangements. Analytical results are compared to experimentally obtained results.

Chapter 5 outlines the basic principles of statistical energy analysis (SEA). A hybrid approach incorporating the waveguide method and SEA techniques is also introduced.

Finally, Chapter 6 is a summary of the work presented in this thesis. The scope for future work in this field of study is also discussed.

1.3 Literature Review

A vast amount of work has been carried out in the analysis of structure vibration as well as methods of attenuating the vibrational response and radiated noise. Literature ranging from 1936 to the present day has been reviewed. The dynamic response of thin plates under free and forced vibration, and for various boundary conditions is well documented in several texts [1-4] and will not be covered further in this literature review. The literature review has been separated into three sections with the first part dealing with the dynamic response of coupled plates. The second part deals with the active control of various engineering structures, including a review on various active control experiments and optimisation of the control force and error sensor numbers and locations. The final section gives an overview of the use of SEA to estimate the energy levels in coupled structures. This technique provides a simple model to analyse the mid to high frequency vibrational response of a structure.

1.3.1 Wave propagation in plate structures

In the past few decades, considerable attention has been given to the study of wave propagation through coupled plate structures in an L, T or cross configuration as they are commonly found in ship hulls and buildings [5-14]. Budrin and Nikiforov [5] investigated the transmission of flexural and extensional waves normally incident to the corner junction in T and cross-shaped plates. The energy reflection and transmission coefficients, and the frequency response for the coupled plates were determined. It was shown that as the frequency is increased, the extensional reflection coefficient decreased. Therefore, the amount of energy transmitted through the joint as flexural and

extensional waves increased. Boisson *et al.* [6] investigated the energy transmission in a finite L-shaped plate structure. The effect of thickness ratio, surface areas, damping, type and position of excitation parameters on the energy transmission were investigated. It was found that the energy transmission changed considerably depending on these parameters. Cremer *et al.* [7] used an analytical wave propagation approach to analyse the incident to transmitted energy ratio through the junction of an infinite L-shaped plate. Using continuity equations for bending, longitudinal and shearing affects at the corner junction, wave transmission and reflection coefficients were obtained. Langley and Heron [8] used the propagating elastic waves to investigate waves that were partially reflected and transmitted at structural discontinuities such as plate junctions and stiffeners. By determining the transmission coefficients at the structural joints, they were able to obtain the coupling loss factors for an SEA model.

Kim *et al.* [9] used a modal analysis method to investigate the bending wave transmission in inter-connected rectangular plates in the mid to high frequency ranges. The global system was separated into individual plates, which were coupled together by continuity of the kinematic parameters and equilibrium of the kinetic parameters. The transmission of bending waves in multi-connected plates in the mid or high frequency ranges were studied by using deterministic methods such as modal and mobility analyses. In a further study, Kim *et al.* [10] analytically investigated the effect of in-plane modes on structure-borne noise propagation in ship structures. Using the boundary conditions, continuity equations and taking into account the bending, shearing and longitudinal effects at the corner junction, the wave amplitudes were determined.

Cuschieri and McCollum [11] presented a model for the coupling of thick plates in an L-shape using Mindlin theory, which includes the effect of rotary inertia and shear deformation. Flexural, in-plane longitudinal and in-plane shear vibration were considered, and results up to 100 kHz were presented. Farag and Pan [12] presented a mathematical model to predict the dynamic response and power flow at the coupling edge of two finite plates joined together at an arbitrary angle. The coupling at the joint edge considered bending, shear and in-plane longitudinal vibration. The flexural mode shapes and resonance frequencies for rectangular plate panels with one free edge and the other edges simply supported were derived. The forced flexural response due to point force and moment excitations were expressed in the form of modal receptance functions.

1.3.2 Active vibration control

While vibrations occur in the low to high frequency ranges, the low range frequencies are the most difficult to attenuate. Structural vibration may be attenuated using either passive or active vibration control techniques. The use of passive control techniques involves modifying the physical characteristics such as stiffness, mass or damping. The use of passive elements such as rubber isolators is not practical in the low frequency range in many systems such as in maritime vessels, where size and mass constraints are important. Hence, active control techniques may be a more effective means of vibration attenuation.

Active vibrational control is a technique that electronically generates an additional vibrational field to cancel the unwanted vibration. A typical active control system is a

combination of three fundamental components, corresponding to actuators and sensors coupled by a controller. In contrast to passive vibration control, active vibration control systems require external assistance such as a power supply. Although the basic concepts of active control and the use of superposition to attenuate vibration levels have been known for sometime [15], it has only recently been applied in practical applications. This is primarily due to immense advances in microprocessor and transducer technology.

The concept of active control was initiated and patented by Lueg [15]. His invention was used to attenuate the noise produced in an air duct by a driving fan. Lueg proposed that by using the principle of superposition, a sound signal might be nullified by introducing an identical secondary sound signal 180 degrees out of phase. It was shown that the source of the sound may be detected and then converted into an electrical signal. This signal was then fed into a loud speaker to produce an anti-phase signal that cancelled the original sound.

Redman-White *et al.* [16] presented experimental work on active methods of reducing the magnitude of the vibrational power flow associated with the propagation of flexural waves in elastic structures. The experimental results demonstrated that two closely spaced piezoelectric (PZT) actuators used as the secondary force inputs can be used to absorb the energy associated with the propagation of flexural waves in a uniform thin beam. The PZT actuators can be bonded directly to the structural surface or in some cases actually embedded in the material. Crawley and de Luis [17], Bailey and Hubbard [18], and Fanson and Chen [19] have all investigated vibration control with the use of piezoelectric actuators.

Active control has been successfully used both theoretically and experimentally to reduce vibration transmission and sound radiation from a thin panel [20,21]. The sound transmission through and radiation from the vibrating structure was controlled by the application of active forces applied directly to the structure. This approach is known as active structural acoustic control (ASAC). It was shown that using only one or two point forces reduced the vibration levels over a wide range of test frequencies.

Wang *et al.* [22] compared the effect of piezoelectric and point force control actuators on the attenuation of noise transmission in a simply supported plate. The control force was applied using both point force actuators and piezoelectric patches separately. The results show that a reduction of sound transmission through the plate is dependent on the size, number, and position of piezoelectric or point force actuators. The results also indicated that the point force control arrangement produced higher attenuation levels. However, it was shown that the patches have significantly more potential in the noise control field due to their low weight and low cost. Lee and Chen [23] investigated active control techniques on a plate clamped at the edges and excited by an external force at a resonant frequency. Two PZTs were used as the actuators, and an FIR filter LMS algorithm was selected for the control set-up. The results demonstrated that more error sensors should be used at different positions on the plate to obtain better control effectiveness. Park and Baz [24] investigated the fundamentals of active vibration control of plates theoretically and experimentally using the active constrained layer damping (ACLD) method. Particular emphasis was placed on controlling the first two bending modes of vibration in plates. These were treated fully with ACLD methods, using proportional and derivative control laws. Finite element models were developed to describe the dynamics of the ACLD. These models were validated by experiments at

various operating conditions. The results indicated the potential of the ACLD as a highly effective means for damping structural vibrations.

Clark and Fuller [25] experimentally studied the active structural control of sound radiation using a vibrating simply supported test plate mounted in a rigid steel frame. The simply supported boundary conditions were achieved by attaching thin shim spring steel to the boundaries of the plate via a sealing compound and setscrews. The shims were then mounted to the rigid steel frame that restricted out of plane motion at the boundaries, but still allowed the plate to bend relatively freely. A signal generator was used to create a harmonic disturbance and the signal was amplified to drive the electrodynamic shaker, which in turn drove the plate. Two identical plates were constructed for testing. The number and position of the actuators were changed for each case to highlight the effect on distributed control. The experimental tests included both on and off resonance disturbance. The following important results were obtained from the experimental study:

1. increasing the number of control piezoelectric actuators will only slightly improve sound attenuation for on resonance cases;
2. for off resonance cases, improvements in sound attenuation were observed when increasing the number of control piezoelectric actuators;
3. the location at which the control actuators were placed on the plate affected the sound attenuation.

Similar work carried out by Guigou *et al.* [26] using a semi-infinite beam with a clamped edge confirmed that the attenuation is dependent on the actuator position rather than actuator type.

Elliott and Billet [27] investigated both analytical and experimental broadband active control of flexural waves propagating along a beam. A simple practical arrangement consisting of a single error sensor (an accelerometer) whose signal output was used to drive a single secondary force via a feedforward controller. The experiments were performed on a steel beam, where each end of the beam was placed in a sand box to make the beam anechoic above 200Hz. Attenuations in the bending wave amplitudes of between 10 and 30dB were measured in the experiments over a frequency range from 100Hz to 600Hz. Clark *et al.* [28] also experimentally investigated active control of multiple wave types in a semi-infinite beam. Active control of two flexural waves and one extensional wave in a thick beam was achieved using a multichannel adaptive LMS algorithm implemented in a digital signal processor. It was found that to successfully control multiple wave types in a structure, error sensors and actuators capable of observing and controlling independent wave types are required.

Pan and Hansen [29] analytically investigated the feedforward active control of harmonic vibratory power transmission along a semi-infinite plate of finite width. One end of the plate was free while the other end was terminated anechoically. The remaining two sides were simply supported. Primary and control driving force configurations incorporating multiple sources were arranged in a line across the plate, and single sources were arranged at various locations. The reduction in power transmission from a simple harmonic primary excitation was in excess of 15 dB for a single point control force. This reduction was dependent on positioning of the control force. The active control system's performance decreased rapidly as the control force was moved from the optimum location. Vibratory power transmission reductions in

excess of 50 dB over a wide frequency range were achieved when three or more independently driven control forces in a row across the plate were used.

Kessissoglou [30] analytically investigated the use of active control of an L-shaped plate to attenuate the flexural energy transmitted from one plate to the other. The flexural wave coefficients were determined using the boundary conditions, and continuity equations at the driving force location and corner junction. Bending and longitudinal effects were taken into account at the corner junction. It was shown that the control performance was dependent on the excitation frequency when the error sensor and the control force were arbitrarily located. When both error sensor and control force were optimally located with respect to the simply supported plate edges, the control performance was maximized and independent of the excitation frequency.

Active control techniques were used by Young and Hansen [31,32] on stiffened plates and cylindrical shells. The equations of motion were solved for each structure to determine the vibration response of the structure to a range of force and moment excitations. The number of control sources and error sensors required for optimal vibration reduction was calculated for the plate and cylinder cases. The vibrations in the stiffened beams, plates and cylinders were actively controlled using stack actuators placed between the flange of a stiffener and the structure surface and accelerometer error sensors.

Sergent and Duhamel [33] demonstrated that the optimisation of the placement of secondary sources and error sensors can enhance the efficiency of active vibration control, and may be achieved using the cost function known as the “minimax” criterion.

The criterion is based on the minimisation of the largest squared pressures at a number of distributed points and is adapted to find the most suitable placement of sources and sensors. Other researchers to use numerical optimisation techniques include Liu and Onoda [34]. The optimal sensor/actuator problem was addressed in the framework of integrated control structure design. Perez and Devasia [35] optimised several cost functions on vibration reduction by tuning the position and size of a collocated piezoelectric sensor bonded on the structure. Jemai *et al.* [36] used the independent modal strategy control (IMSC) for active structural control. The structure under consideration consisted of three shaped plates, which were soldered together, and the distributed sensors and actuators were PZT ceramics. Numerical methods were used to optimise shape and location of the sensors and actuators on the structure, and to minimise the effect on unwanted modes. Experimental results were obtained and the vibration reduction was compared to the results obtained from a finite element analysis. The authors listed in this paragraph all employ a model based control design method to obtain the optimal error sensor and actuator placement. Hiramoto *et al.* [37] considered an optimal sensor/actuator placement problem for flexural structures. They showed that several gradient-based algorithms might be used to formulate the optimal placement problem with significantly less computational complexity than the modal-based method previously mentioned.

In numerous active control laboratory experiments a digital signal processor (DSP) hosted by a personnel computer controls the system. Signals from the error sensors are transferred to the DSP board. The controller processes this information and produces a control signal that is fed to the control actuators. These signals are commonly calculated based in a filtered-X adaptive LMS algorithm. Elliott *et al.* [38] explain this algorithm

and its use for active vibration and noise control in detail. The steepest gradient descent method employed by the algorithm minimises the least mean square of the error signals by converging on the set of optimal weighting coefficients for the adaptive filters. Clark and Fuller [25] have also implemented this control algorithm for noise control from plates. For resonance cases, it was found that only marginal improvement was achieved by increasing the number of control forces. For off-resonance conditions, an increase in the number of control actuators resulted in a significant improvement in sound attenuation.

As outlined in the previous paragraphs, active control has received an enormous amount of research attention in the last decade. Initially it appeared very promising as a novel control technique for attenuation of vibration and its transmission, and radiation as noise. However, there are still enormous problems associated with its practical application due to environmental uncertainties, stability issues, lack of robustness, complexity with the electronics and transducers, cost of application and also high maintenance costs. These problems however are being addressed with the developments in transducers, namely inertial and reactive actuators [39,40].

1.3.3 Statistical energy analysis

There is an enormous quantity of literature on statistical energy analysis (SEA), as demonstrated in References 41 to 60. This section aims to give a brief overview on the literature available and the basic principles behind SEA. SEA provides a simple framework to analyse high frequency structural noise and vibration in complex built up structures. The modelling procedure uses energy flow relationships between various

coupled subsystems, such as plates, beams, stiffeners and acoustic spaces within the system. SEA is most commonly used in the high frequency regions where a deterministic or exact analysis of the vibration is not practical due to the high number of resonant modes.

SEA applies an energy balance principle to the system, where the system is made up from coupled subsystems [41,42]. In SEA, a complex structure is divided into a number of component subsystems, each corresponding to a certain wave type, and exchanging energy with others through coupling characterised by coupling loss factors. The energy flow into a system (input power), the energy flow out of a system (dissipated power), the energy flow between subsystems (coupling power) and the energy within the subsystem are all considered. The power and energies are averaged over time, space and frequency, and greater accuracy is obtained with a greater population of modes [42].

Tratch [43] applied SEA to study vibration transmissions in multi-plate structures. The study included identification of the sub-systems, determination of the various SEA parameters and employing the power balance equation to estimate energy ratios of each subsystem. Analytical expressions were also formulated to determine the average transmission coefficients between up to four plates coupled at a common joint. The predicted flexural energy levels were compared with those obtained from experimental testing with good results.

Generally, SEA is only accurate when there is weak coupling between the subsystems. Many deterministic studies have been conducted to determine the degree of validity of

this statement [44-46]. The deterministic methods were carried out on simple structures such as beams or rods coupled by springs and coupled plates. Exact energy flow relationships between two hinged beams coupled by springs were calculated by Davies [44]. Remington and Manning [45] investigated the effect of increasing coupling spring stiffness on the energy flow between two axially vibrating rods connected end to end.

For the SEA model to be successful, various parameters must be accurately estimated. These parameters are the modal density, damping loss factors and coupling loss factors. The determination of the coupling loss factor is a central and difficult problem for SEA models [47]. A popular method to obtain the SEA parameters is FEM [48-53]. Hynnä *et al.* [51] presents a method to predict the structure-borne sound transmission in a large welded ship structure using SEA and FEM. Employing FEM substantially reduced the modelling work. Fredö [52] also employed a finite element method combined with a statistical energy analysis-like flow balance method to derive the power transmission between two thin plates. Other methods to obtain the SEA parameters include the empirical formulations [54]. Yan *et al.* [55] calculated the direct coupling loss factors between several test plates in the mid frequency range using an impedance approach.

Luzzato and Ortola [56] showed significant energy flow paths between subsystems using coupling loss factors so that the most energetic subsystems may be isolated. Possible paths of energy flow between two subsystems were identified and assigned transmission coefficients, comprised from the coupling and internal loss factors of the subsystems, to gauge their importance in energy transfer.

A wave approach was used by Webster and Mace [57] in the statistical energy analysis of a system comprised of two edge-coupled, simply supported rectangular plates. An ensemble of plate systems is defined, and analytical expressions are found for the ensemble average input and coupling powers that result from "rain-on-the-roof" excitation of one of the plates. The energy balance equations used in SEA are briefly described in their work accompanied by details of the plate system and wave component model. The exact coupling loss factor, found by a wave approach based on ensemble average coupling power and subsystem energies, was determined. It was found that this estimate of the coupling loss factor tends to be higher than the actual coupling loss factor in most cases of practical interest, except when the coupling is weak. Another hybrid modelling strategy was employed by Lande *et al.* [58] to predict the SEA energy levels in a beam-plate structure. The SEA power input to the plate subsystem was calculated by adding a power absorbing plate impedance matrix to the regular beam network impedance matrix in the FEM formulation.

Mace and Rosenberg [59] considered a system comprising two edge-coupled plates. Theoretical predictions of the coupling power and coupling loss factors using SEA were made. These results were then compared to numerical estimates of the frequency average powers and coupling loss factors found from FE models over the whole system. A wide variety of plate shapes were investigated as well as different levels of damping. It was demonstrated that the response is independent of the shape of the plates if the damping is large enough. When the damping is smaller, the plate's response was found to depend more on its geometry and the coupling power is considerably less than that predicted by SEA.

Langley and Shorter [60] present a general methodology for calculating the wave transmission coefficients and coupling loss factors between components that are coupled together at a point. Examples for infinite plates and semi-infinite beam components were presented and it was found that the coupling loss factors satisfy reciprocity.

1.4 Contribution to Research

Much work has been conducted in the field of active control on single beam and plate structures. In contrast, very little work has been conducted on the vibrational response and its control in complex structures. This thesis aims to contribute to the dynamic response characteristics in coupled plate structures, typically found in a ship hull. The main theme of this thesis is to use active control techniques to attenuate the vibrational responses in L, T and X-shaped plates. Travelling wave solutions are used to describe the bending wave motion in the plates. A further section of this thesis investigates an approach to predict the vibration transmission in a complex built up plate structure in the mid frequency range. To achieve this, a hybrid approach between the analytical travelling wave method used in the main theme of the thesis, and an energy approach known as Statistical Energy Analysis is developed.

CHAPTER 2

ANALYTICAL MODELLING OF THE DYNAMIC RESPONSE AND ACTIVE CONTROL OF CONNECTED PLATES

2.1 Introduction

This chapter outlines the plate theory used to determine the dynamic and controlled response of a coupled plate structure. The theory is presented for a generic structure consisting of four finite plates joined together at right angles in an X-shape. The plate material is assumed to be homogenous and isotropic. The theory for active vibration control of the coupled plate using single and multiple control actuators and error sensors is presented for both independent and dependent control.

2.2 Plate Theory

The geometry of the plates and the alignment of the co-ordinate system are shown in Figure 2.1. For mathematical simplicity, all four plates are simply supported along edges $y = 0$ and $y = L_y$ and are free at the other ends corresponding to $x_i = L_{xi}$ for i = 1 to 4. The junction of the four plates coincides with $x_i = 0$.

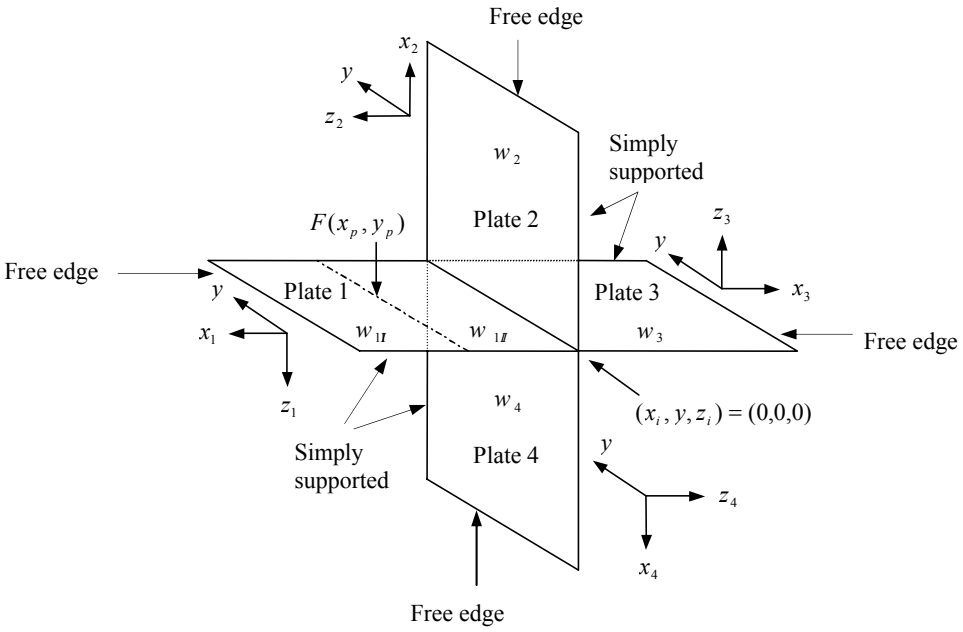

Figure 2.1. Finite X-shaped plate under point force excitation, showing the five regions of the coupled structure, the boundary conditions and the sign convention.

As the plate is simply supported along $y = 0$ and L_y, a modal solution is used to describe the structural response in the $y-$direction. Due to the free edges, a travelling wave solution is used to describe the displacement in the $x-$direction. A point force excitation of amplitude F_p was applied on plate 1 at (x_p, y_p) to model the external disturbance. The forcing function can be described by the Dirac delta function:

$$F(x,y,t) = F_p \delta(x - x_p)\delta(y - y_p)e^{j\omega t}. \tag{2.1}$$

The plate flexural displacements are governed by the classical equation of motion [4]:

$$D\nabla^4 w(x,y,t) + \rho h \frac{\partial^2 w(x,y,t)}{\partial t^2} = F(x,y,t) \tag{2.2}$$

where $\nabla^4 = \nabla^2\nabla^2$ and $\nabla^2 = \frac{\partial^2}{\partial x^2} + \frac{\partial^2}{\partial y^2}$ is the Laplace operator. $D = Eh^3/12(1-\nu^2)$ is the plate flexural rigidity, where E is Young's Modulus, ν is Poisson's ratio, ρ is the density, and h is the plate thickness. Since the plate displacement is time harmonic with radian frequency ω, the time dependent factor $e^{j\omega t}$ can be omitted in the proceeding analysis.

The X-shaped plate can be separated into five sections, as shown in Figure 2.1. Note that on plate 1, the primary displacement $w_{p1}(x_1, y)$ is separated into two components $w_{p1I}(x_1, y)$ for $(x_p \le x_1 \le L_{x1})$ and $w_{p1II}(x_1, y)$ for $(0 \le x_1 \le x_p)$ due to the external driving force. The plate primary flexural displacement in the various sections can be described by:

$$w_{pi}(x_i, y) = \sum_{m=1}^{\infty} (A_i^p e^{-jk_x x_i} + B_i^p e^{jk_x x_i} + C_i^p e^{-k_n x_i} + D_i^p e^{k_n x_i}) \sin k_y y \qquad i = 1 \text{ to } 4 \tag{2.3}$$

where A_i^p and B_i^p are coefficients of the propagating waves, and C_i^p and D_i^p are coefficients of the near-field decay waves. $k_x = \sqrt{k_p^2 - k_y^2}$ is the propagating wave number in the $x-$direction, and $k_n = \sqrt{k_p^2 + k_y^2}$ is the wave number in the $x-$direction for the decay waves. $k_p = \sqrt{\omega}(\rho h/D)^{1/4}$ is the plate bending wave number. $k_y = m\pi/L_y$ is the

wave number in the $y-$direction due to the simply supported boundary conditions, where $m = 1$, 2, 3,…, ∞ is the mode number. For plates of the same material properties, lengths and thicknesses, the various structural wave numbers are the same for each plate. For a T-shaped structure, plate 4 and $w_{p4}(x_4, y)$ are eliminated, and similarly, for an L-shaped plate, plates 3 and 4, and therefore $w_{p3}(x_3, y)$ and $w_{p4}(x_4, y)$ are not required.

It is evident that if the structural response is to be calculated for the L, T and X plate configuration then 12, 16 and 20 unknown constants must be evaluated respectively. These can be found using boundary equations at the free edges, and the continuity equations at the driving force location and junction of the plates. At the free edges corresponding to $x_i = L_{xi}$, the bending moment and net vertical shear force are zero [2]. The net vertical shear force and bending moment are respectively given by:

$$Q_{xi} = -D\left(\frac{\partial^3 w_{pi}}{\partial x_i^{\,3}} + (2-v)\frac{\partial^3 w_{pi}}{\partial x_i \partial y^2}\right) \tag{2.4}$$

$$M_{xi} = -D\left(\frac{\partial^2 w_{pi}}{\partial x_i^{\,2}} + v\frac{\partial^2 w_{pi}}{\partial y^2}\right). \tag{2.5}$$

At the driving force location of (x_p, y_p), four coupling equations are used to describe the continuity of the plate response under forced excitation [27]. The continuity relationships

correspond to the continuity of the plate displacement, slope, moment and shear force. These are respectively given by:

$$w_{p1I} = w_{p1II} \tag{2.6}$$

$$\frac{\partial w_{p1I}}{\partial x_1} = \frac{\partial w_{p1II}}{\partial x_1} \tag{2.7}$$

$$\frac{\partial^2 w_{p1I}}{\partial x_1^{\,2}} = \frac{\partial^2 w_{p1II}}{\partial x_1^{\,2}} \tag{2.8}$$

$$\frac{\partial^3 w_{p1I}}{\partial x_1^{\,3}} - \frac{\partial^3 w_{p1II}}{\partial x_1^{\,3}} = \frac{2F_p}{L_y D}\sin(k_y y_p)\sin(k_y y) \tag{2.9}$$

The boundary conditions at the structural junction of the coupled plates corresponding to $(x_i, z_i)=(0,0)$ must also satisfy continuity of plate displacement, slope, moment and shear force. Using the sign convention outlined in Figure 2.1, equations (2.10) and (2.11) correspond to the continuity of the plate displacement while equation (2.12) corresponds to the continuity of the slope at the junction. Equations (2.13) to (2.15) describe the equilibrium of forces and moments at the junction.

$$-w_{p1II} = u_2 = w_{p3} = -u_4 \tag{2.10}$$

$$-u_1 = -w_{p2} = u_3 = w_{p4} \tag{2.11}$$

$$\frac{\partial w_{p1II}}{\partial x_1} = \frac{\partial w_{p2}}{\partial x_2} = \frac{\partial w_{p3}}{\partial x_3} = \frac{\partial w_{p4}}{\partial x_4} \tag{2.12}$$

$$Q_{x1} - N_{x2} - Q_{x3} + N_{x4} = 0 \tag{2.13}$$

$$N_{x1} + Q_{x2} - N_{x3} - Q_{x4} = 0 \tag{2.14}$$

$$M_{x1} + M_{x2} + M_{x3} + M_{x4} = 0 \tag{2.15}$$

Note that at the junction of the plates, Q_{xi} and M_{xi} in plate 1 are functions of $w_{p\,1II}$. u_i is the in-plane longitudinal displacement in the $x-$direction. The in-plane longitudinal force N_{xi} can be written in terms of u_i using the impedance formula $u_i = -N_{xi}/j\omega\rho hc_L$ [7], where for each plate, u_i is acting in the opposite direction to N_{xi}. c_L is the longitudinal wave speed and is given by $c_L = \sqrt{E/\rho(1-\nu^2)}$. For the L and T-shaped structures, the boundary conditions are obtained by eliminating components associated with the removed plates.

Using the boundary and continuity conditions, and the general solutions for the plate displacements described by equation (2.3), a matrix equation is obtained of the form

$[\alpha_p][\mathbf{X}] = [\mathbf{F_p}]$. The coefficient matrix $[\mathbf{X}]$ and the force matrix $[\mathbf{F_p}]$ for the cross-shaped plate are given by equations (2.16) and (2.17) respectively.

$$[\mathbf{X}] = \left[A_{1I}^P\ B_{1I}^P\ C_{1I}^P\ D_{1I}^P\ A_{1II}^P\ B_{1II}^P\ C_{1II}^P\ D_{1II}^P\ A_2^P\ B_2^P\ C_2^P\ D_2^P\ A_3^P\ B_3^P\ C_3^P\ D_3^P\ A_4^P\ B_4^P\ C_4^P\ D_4^P\right]^T \quad (2.16)$$

$$[\mathbf{F_p}] = \left[0\ \ 0\ \ 0\ \ 0\ \ 0\ \ 0\ \ 0\ \ 0\ \ 0\ \ 0\ \ 0\ \ \frac{2F_p}{L_y}\sin k_y y_p\ \ 0\ \ 0\ \ 0\ \ 0\ \ 0\ \ 0\ \ 0\ \ 0\right]^T. \quad (2.17)$$

A solution for the unknown coefficients of column vector $[\mathbf{X}]$ may be obtained by $[\mathbf{X}] = [\alpha_p]^{-1}[\mathbf{F_p}]$. For the L, T and X-shaped plates, $[\alpha_p]$ corresponds to a 12×12, 16×16 and 20×20 matrix respectively. The $[\alpha_p]$ matrices associated with the L, T and X-shaped plates are given in Appendices A, B and C respectively. In the $[\alpha_p]$ matrix, $k_L = \omega/c_L$ is the longitudinal wave number.

For the active control modelling, it is more convenient to describe the plate flexural displacements in terms of the product of the external force amplitude and a transfer function [27]. Hence, the primary plate flexural displacement in the various sections can also be described by $w_p(x,y) = F_p\, G_p(x,y)$. $G_p(x,y)$ is the primary transfer function and is given by:

$$G_{pi}(x,y)=\sum_{m=1}^{\infty}\frac{2}{L_y D}\sin(k_y y_p)\left[\alpha_p\right]^{-T}_{n,12}\left[E^i_p\right]\sin(k_y y) \tag{2.18}$$

where i = 1 to 2 for an L-shaped plate, i = 1 to 3 for a T-shaped plate, and i = 1 to 4 for a cross-shaped plate. As the forcing matrix [$\mathbf{F_p}$] has one non-zero element only, the inverse transpose matrix $[\alpha_p]^{-T}$ can be expressed using a single column of the matrix $[\alpha_p]$. For the X-shaped plate, $[\alpha_p]^{-T}_{n,12}$ corresponds to the twelfth column of the inverse matrix $[\alpha_p]^{-T}$ where n = 1 to 20 corresponds to the number of rows. For the X-shaped plate, $[E_i^p]$ is described as:

$$[E_{1I}^p] = [\,e^{-jk_x x_1}\;\; e^{jk_x x_1}\;\; e^{-k_n x_1}\;\; e^{k_n x_1}\;\; 0\;0\;0\;0\;0\;0\;0\;0\;0\;0\;0\;0\;0\;0\,]^T \quad x_p \le x_1 \le L_{x1} \tag{2.19}$$

$$[E_{1II}^p] = [\,0\;0\;0\;0\;\; e^{-jk_x x_1}\;\; e^{jk_x x_1}\;\; e^{-k_n x_1}\;\; e^{k_n x_1}\;\; 0\;0\;0\;0\;0\;0\;0\;0\;0\,]^T \quad 0 \le x_1 \le x_p \tag{2.20}$$

$$[E_2^p] = [\,0\;0\;0\;0\;0\;0\;0\;0\; e^{-jk_x x_2}\;\; e^{jk_x x_2}\;\; e^{-k_n x_2}\;\; e^{k_n x_2}\;\; 0\;0\;0\;0\;0\;0\;0\;0\,]^T \quad 0 \le x_2 \le L_{x2} \tag{2.21}$$

$$[E_3^p] = [\,0\;0\;0\;0\;0\;0\;0\;0\;0\;0\;0\;0\;0\;0\; e^{-jk_x x_3}\;\; e^{jk_x x_3}\;\; e^{-k_n x_3}\;\; e^{k_n x_3}\;\; 0\;0\;0\;0\,]^T \quad 0 \le x_3 \le L_{x3} \tag{2.22}$$

$$[E_4^p] = [\,0\;0\;0\;0\;0\;0\;0\;0\;0\;0\;0\;0\;0\;0\;0\;0\;0\;0\; e^{-jk_x x_4}\;\; e^{jk_x x_4}\;\; e^{-k_n x_4}\;\; e^{k_n x_4}\,]^T \quad 0 \le x_4 \le L_{x4}. \tag{2.23}$$

2.3 Active Control

A secondary point force of amplitude F_s is applied at a position on plate 1 corresponding to (x_s, y_s). The secondary flexural displacement can also be described by both a travelling wave solution in the $x-$direction and a modal solution in the $y-$direction. In the active control case, the general solution for the secondary displacement is given by $w_s(x,y) = F_s\, G_s(x,y)$, where G_s is of a similar form to G_p, except $[\alpha_p]$, $[E_i^p]$ and y_p are replaced with $[\alpha_s]$, $[E_i^s]$ and y_s respectively. G_s is now a summation over all modes m'. The total flexural displacement is obtained by adding the plate displacement induced by the primary force and the secondary flexural waves generated by the control source:

$$w_{tot}(x,y) = w_p(x,y) + w_s(x,y). \tag{2.24}$$

A cost function is developed so that the total squared plate displacement due to the primary and control inputs at an error sensor location (x_e, y_e) is minimised. The controller implemented is based on a feedforward LMS algorithm [61]. It is expressed as a quadratic function in terms of the complex control force amplitude:

$$w_{tot}(w_{tot})^* = F_s^* A_\Pi F_s + F_s^* B_\Pi F_p + F_s B_\Pi^* F_p^* + F_p^* C_\Pi F_p \tag{2.25}$$

where the asterisk * denotes the complex conjugate, and $A_\Pi = G_s^* G_s$, $B_\Pi = G_s^* G_p$ and $C_\Pi = G_p^* G_p$. The optimal control force amplitude that results in the minimisation of the

cost function is determined by setting the partial derivatives of the cost function with respect to the real and imaginary parts of the control force to zero. That is, $\frac{\partial w_{tot}(w_{tot})^*}{\partial F_{s\,real}}=0$ and $\frac{\partial w_{tot}(w_{tot})^*}{\partial F_{s\,imag}}=0$. The optimal control force can then be obtained as:

$$F_s\big|_{opt} = F_{s\ real} + j\,F_{s\ imag} = -F_p\frac{B_\Pi}{A_\Pi}. \tag{2.26}$$

The expression given in equation (2.26) remains the same for the various control configurations using either a single control force, or multiple dependently driven control forces. In the case of multiple dependently driven control forces, the control forces are driven in phase and with the same complex amplitude F_s. However, the quadratic terms A_Π, B_Π and C_Π change depending on the number of control forces and error sensors, and are given for several different control configurations in the proceeding sections.

2.3.1 Active control using a single control force and multiple error sensors

When multiple error sensors are considered, the total squared plate displacement is minimised at all error sensor locations simultaneously:

$$w_{tot}(w_{tot})^{*} = \sum_{e=1}^{n}\Big(w_p(x_e,y_e) + w_s(x_e,y_e)\Big)\Big(w_p(x_e,y_e) + w_s(x_e,y_e)\Big)^{*}$$

$$= \sum_{e=1}^{n}\Big(F_p\, G_p(x_e,y_e) + F_s\, G_s(x_e,y_e)\Big)\Big(F_p\, G_p(x_e,y_e) + F_s\, G_s(x_e,y_e)\Big)^{*} \qquad (2.27)$$

where $e=1$ to n represents the number of error sensors. The cost function terms in equation (2.25) now become:

$$A_{\Pi} = \sum_{e=1}^{n} G_s^{*}(x_e,y_e)\, G_s(x_e,y_e) \qquad (2.28)$$

$$B_{\Pi} = \sum_{e=1}^{n} G_s^{*}(x_e,y_e)\, G_p(x_e,y_e) \qquad (2.29)$$

$$C_{\Pi} = \sum_{e=1}^{n} G_p^{*}(x_e,y_e)\, G_p(x_e,y_e). \qquad (2.30)$$

2.3.2 Active control using multiple control forces driven dependently and a single error sensor

For multiple dependently driven control forces, there is still only one optimal complex control force amplitude F_s to be determined. The total plate displacement due to the primary and control forces at the error sensor location is given by:

$$w_{tot} = w_p(x_e, y_e) + \sum_{j=1}^{N} w_{sj}(x_e, y_e) = F_p G_p\left(x_e, y_e\right) + F_s \sum_{j=1}^{N} G_{sj}(x_e, y_e). \tag{2.31}$$

G_{sj} represents the secondary transfer function for the j^{th} control force, where $j = 1$ to N represents the number of control forces. The cost function terms in equation (2.25) now become:

$$A_{\Pi} = \sum_{j=1}^{N} G_{sj}^{*}(x_e, y_e) \sum_{j=1}^{N} G_{sj}(x_e, y_e) \tag{2.32}$$

$$B_{\Pi} = \sum_{j=1}^{N} G_{sj}^{*}(x_e, y_e) G_p(x_e, y_e) \tag{2.33}$$

$$C_{\Pi} = G_p^{*}(x_e, y_e) G_p(x_e, y_e). \tag{2.34}$$

2.3.3 Active control using multiple control forces driven dependently and multiple error sensors

When multiple dependently driven control forces and multiple error sensors are used for the active control, the cost function to be minimised is the total squared plate displacement due to all forces at all the error sensor locations simultaneously:

$$w_{tot}(w_{tot})^* = \sum_{e=1}^{n}\left(w_p(x_e,y_e) + \sum_{j=1}^{N} w_{sj}(x_e,y_e) \right)\left(w_p(x_e,y_e) + \sum_{j=1}^{N} w_{sj}(x_e,y_e) \right)^*$$

$$= \sum_{e=1}^{n}\left(F_p\, G_p(x_e,y_e) + F_s \sum_{j=1}^{N} G_{sj}(x_e,y_e) \right)\left(F_p\, G_p(x_e,y_e) + F_s \sum_{j=1}^{N} G_{sj}(x_e,y_e) \right)^* \quad (2.35)$$

where n is the number of error sensors and N is the number of control forces. The quadratic function terms in the cost function in equation (2.25) become:

$$A_{\Pi} = \sum_{e=1}^{n}\left(\sum_{j=1}^{N} G_{sj}^*(x_e,y_e) \sum_{j=1}^{N} G_{sj}(x_e,y_e) \right) \quad (2.36)$$

$$B_{\Pi} = \sum_{e=1}^{n}\left(\sum_{j=1}^{N} G_{sj}^*(x_e,y_e) G_p(x_e,y_e) \right) \quad (2.37)$$

$$C_{\Pi} = \sum_{e=1}^{n} G_p^*(x_e,y_e) G_p(x_e,y_e). \quad (2.38)$$

2.3.4 Active control using multiple control forces driven independently and a single error sensor

Using a control configuration consisting of independently driven control forces, the total displacement at the error sensor location (x_e, y_e) is given by the sum of the displacements due to the primary force and the secondary forces:

$$w_{tot} = w_p(x_e, y_e) + \sum_{j=1}^{N} w_{sj}(x_e, y_e) = F_p G_p(x_e, y_e) + \sum_{j=1}^{N} F_{sj} G_{sj}(x_e, y_e) \tag{2.39}$$

where F_{sj} are the complex control force amplitudes to be optimised. In the case of two independently driven control forces, there are two control force amplitudes, corresponding to F_{s1} and F_{s2} to be optimised. To find the optimal control force amplitudes, the partial derivatives of the total squared plate displacement with respect to the real and imaginary parts of the control forces are set to zero as described in section 2.3, resulting in:

$$\frac{\partial w_{tot} (w_{tot})^*}{\partial F_{s1\ real}} = 2G_{s1}^* G_{s1} F_{s1\ real} + G_{s1} G_{s2}^* F_{s2}^* + G_{s1}^* G_{s2} F_{s2} + F_p G_p G_{s1}^* + F_p^* G_p^* G_{s1} = 0 \tag{2.40}$$

$$\frac{\partial w_{tot} (w_{tot})^*}{\partial F_{s1\ imag}} = 2G_{s1}^* G_{s1} F_{s1\ imag} + jG_{s1} G_{s2}^* F_{s2}^* - jG_{s1}^* G_{s2} F_{s2} - jF_p G_p G_{s1}^* + jF_p^* G_p^* G_{s1} = 0 \tag{2.41}$$

$$\frac{\partial w_{tot} (w_{tot})^*}{\partial F_{s2\ real}} = 2G_{s2}^* G_{s2} F_{s2\ real} + G_{s2} G_{s1}^* F_{s1}^* + G_{s2}^* G_{s1} F_{s1} + F_p G_p G_{s2}^* + F_p^* G_p^* G_{s2} = 0 \tag{2.42}$$

$$\frac{\partial w_{tot} (w_{tot})^*}{\partial F_{s2\ imag}} = 2G_{s2}^* G_{s2} F_{s2\ imag} + jG_{s2} G_{s1}^* F_{s1}^* - jG_{s2}^* G_{s1} F_{s1} - jF_p G_p G_{s2}^* + jF_p^* G_p^* G_{s2} = 0\,. \tag{2.43}$$

Combining the real and imaginary components of the control forces in equations (2.40) to (2.43) results in:

$$G_{s1}^{*}G_{s1}F_{s1} + G_{s1}^{*}G_{s2}F_{s2} = -F_{p}G_{s1}^{*}G_{p} \tag{2.44}$$

$$G_{s2}^{*}G_{s1}F_{s1} + G_{s2}^{*}G_{s2}F_{s2} = -F_{p}G_{s2}^{*}G_{p}\,. \tag{2.45}$$

Equations (2.44) and (2.45) may be rearranged into matrix form to obtain the set of optimal independently driven control forces:

$$\begin{bmatrix} F_{s1} \\ F_{s2} \end{bmatrix} = -F_{p}\begin{bmatrix} G_{s1}^{*}G_{s1} & G_{s1}^{*}G_{s2} \\ G_{s2}^{*}G_{s1} & G_{s2}^{*}G_{s2} \end{bmatrix}^{-1}\begin{bmatrix} G_{s1}^{*}G_{p} \\ G_{s2}^{*}G_{p} \end{bmatrix}. \tag{2.46}$$

For N independently driven control forces, the optimal control force amplitudes can be obtained by:

$$\begin{bmatrix} F_{s1} \\ \vdots \\ \vdots \\ F_{sN} \end{bmatrix} = -F_{p}\begin{bmatrix} G_{s1}^{*}G_{s1} & \cdots & \cdots & G_{s1}^{*}G_{sN} \\ \vdots & \ddots & & \vdots \\ \vdots & & \ddots & \vdots \\ G_{sN}^{*}G_{s1} & \cdots & \cdots & G_{sN}^{*}G_{sN} \end{bmatrix}^{-1}\begin{bmatrix} G_{s1}^{*}G_{p} \\ \vdots \\ \vdots \\ G_{sN}^{*}G_{p} \end{bmatrix}. \tag{2.47}$$

2.3.5 Active control using multiple control forces driven independently and multiple error sensors

When multiple error sensors and multiple independently driven control forces are used, the total plate displacement at the error sensor locations becomes:

$$w_{tot} = \sum_{e=1}^{n} \left(w_p(x_e, y_e) + \sum_{j=1}^{N} w_s(x_e, y_e) \right) = \sum_{e=1}^{n} \left(F_p G_p(x_e, y_e) + \sum_{j=1}^{N} F_{sj} G_{sj}(x_e, y_e) \right) \tag{2.48}$$

where n is the number of error sensors and N is the number of independently driven control forces. Following the procedure in the preceding section, the optimal control force amplitudes can be obtained by:

$$\begin{bmatrix} F_{s1} \\ \vdots \\ \vdots \\ F_{sN} \end{bmatrix} = -F_p \begin{bmatrix} \sum_{e=1}^{n} \left(G_{s1}^* G_{s1} \right) & \cdots & \cdots & \sum_{e=1}^{n} \left(G_{s1}^* G_{sN} \right) \\ \vdots & \ddots & & \vdots \\ \vdots & & \ddots & \vdots \\ \sum_{e=1}^{n} \left(G_{sN}^* G_{s1} \right) & \cdots & \cdots & \sum_{e=1}^{n} \left(G_{sN}^* G_{sN} \right) \end{bmatrix}^{-1} \begin{bmatrix} \sum_{e=1}^{n} \left(G_{s1}^* G_p \right) \\ \vdots \\ \vdots \\ \sum_{e=1}^{n} \left(G_{sN}^* G_p \right) \end{bmatrix}. \tag{2.49}$$

2.4 Kinetic Energy

The total kinetic energy of the coupled plates can be used to compare the difference in attenuation levels for the various error sensor and control force arrangements. Global attenuation of the plate structures can be assessed by examining the difference between the primary and controlled kinetic energy levels. The kinetic energy for each plate can be written as:

$$E_k = \frac{1}{2} M v^2 \tag{2.50}$$

where M is the mass of each individual plate and $v = \dot{w} = j\omega w$ is the velocity. The total kinetic energy of the system is required to determine the attenuation levels achieved for each control set up. The time-averaged vibrational kinetic energy for a single resonance frequency can be written as [61]:

$$E_k(\omega) = \frac{M\omega^2}{4}[\mathbf{X}][\mathbf{X}]^H \tag{2.51}$$

where $[\mathbf{X}]$ is the coefficient matrix of the plate displacement, and the superscript H denotes the complex conjugate and transpose. The total kinetic energy of the system is found by adding the kinetic energies of each of the plates together.

CHAPTER 3

EXPERIMENTAL SET-UP

3.1 Introduction

Chapter 3 is an experimental study of the dynamic response and active control of the thin rectangular coupled plates presented in Chapter 2. This chapter initially deals with the basic principles of a feedforward active control arrangement. Details of the experimental set up, including construction of the test rig and the equipment used, are described.

3.2 Basic Principles of Active Control

Figure 3.1 is a schematic of a typical feedforward active control system used to reduce the vibrational levels of a plate. In a feedforward control application, a reference signal that is used to drive the primary shaker is fed into the controller. The error signal detected by an accelerometer is also fed into the controller. The primary signal is filtered using a device adapted to minimise a cost function. This filtered signal is then used to drive a control shaker, which generates secondary waves in the structure such that the total response or cost function at the error sensor location is minimised.

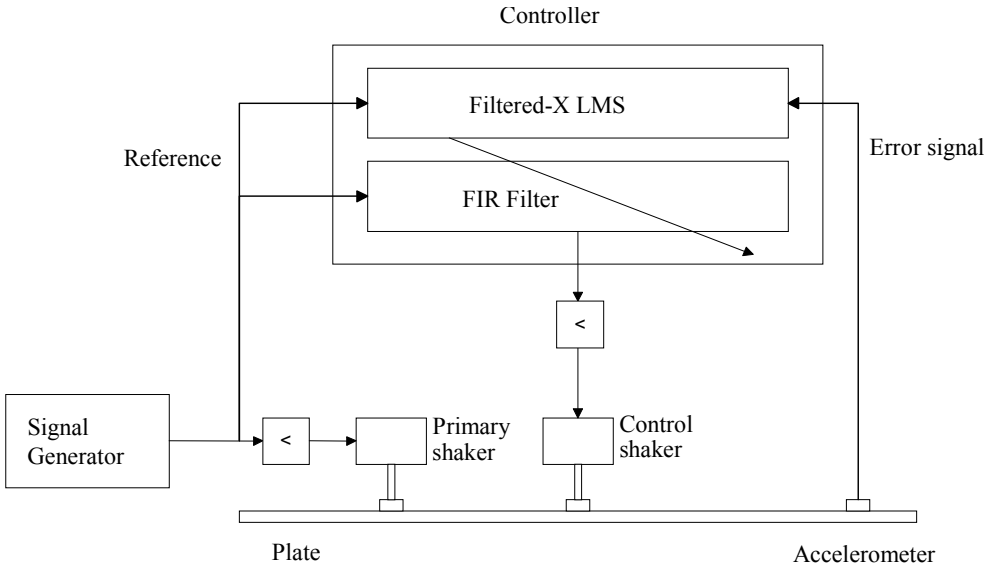

Figure 3.1. Schematic diagram of an active control system used for active vibration control of a plate.

3.3 Description of the Experimental Rig and Equipment

An experimental test rig consisting of two aluminium plates connected at a right angle in an L-shape was constructed. This rig was then converted to a T-shaped plate by welding a third plate to the L-shaped plate. Photos of the L and T shaped plate test rigs are shown in Figures 3.2 and 3.3 respectively. The plate structures were formed by welding together 600mm × 500mm plates along a common 500mm edge. Each plate had a thickness of 2mm. The boundary conditions of the plates were constructed to simulate simply supported conditions on two parallel sides. The plate ends parallel to the L and T junctions were free.

Figure 3.2. Experimental set-up with primary and control shakers attached to the L-shaped plate.

Figure 3.3. Experimental set-up with primary and control shakers attached to the T-shaped plate.

The simply supported boundary conditions were achieved by screwing the edges of the plate to Z-sections at regular intervals of 25mm. The Z-sections needed to be flexible and were constructed of 0.8mm thick aluminium. The lower flange edges of the Z-sections were clamped between concrete blocks. This construction has been previously shown to approximate simply supported boundary conditions, as the Z-sections are stiff for in-plane vibration, but are sufficiently flexible for rotation [62]. Figure 3.4 shows the Z-section attached to the top of the panel by screws and the bottom flange clamped between the concrete blocks.

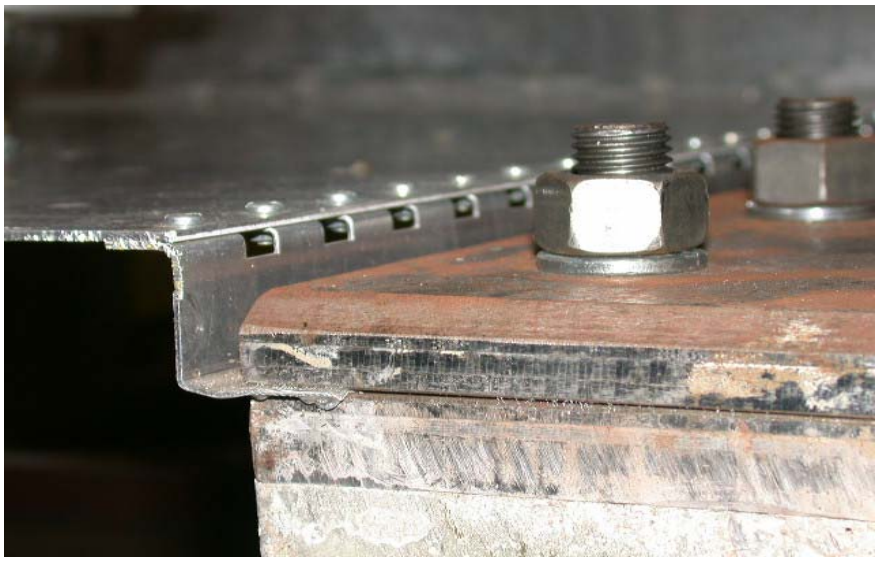

Figure 3.4. Z-section used to simulate the simply-supported boundary conditions.

The primary disturbance shaker and the control shaker, both LDS Type V203 mini shakers, were positioned on plate 1 so that only flexural vibration in the plate was generated. The shakers were mounted vertically over the plate as shown in Figures 3.2 and 3.3. The second control shaker for the multiple control force experiments was mounted on a stand and placed under plate 1. The stand allowed for the force to be

applied vertically. The stand and shaker mounting are shown in Figure 3.5. The error sensors used in the experiments were 2 gram Brüel & Kjær Type 4375 accelerometers. The minimal weight ensured that the effect of mass loading incurred by the accelerometer could be neglected. The accelerometer was attached to the plate using specially formulated beeswax.

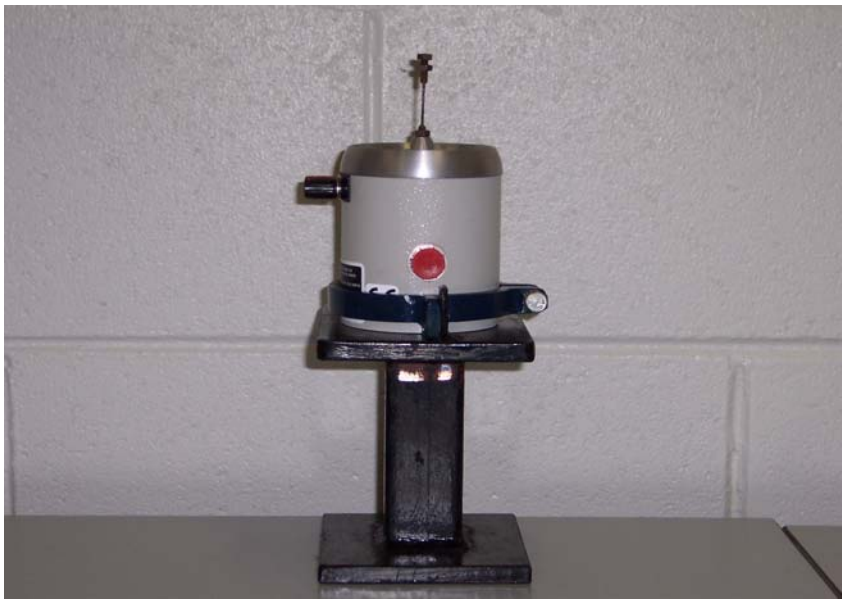

Figure 3.5. Stand and mounting for the second control force for the multiple control force experiments.

3.4 Description of the Active Controller

An EZ-ANC active controller was used in the experiments [63]. The EZ-ANC is an adaptive feedforward active control system that uses an algorithm based on a filtered-X version of the adaptive least-mean-square (LMS) algorithm. Figure 3.6 displays a block

diagram of the adaptive feedforward control system. It can be seen that a measure of the system output is used to adjust the control system to provide maximum attenuation.

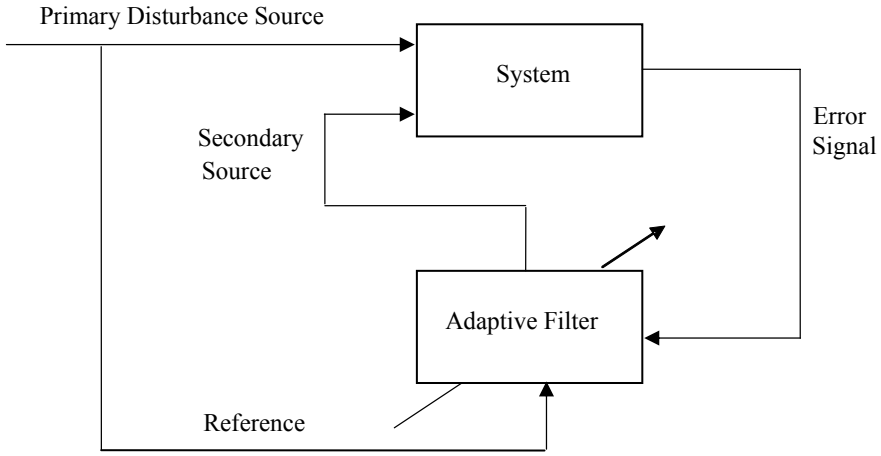

Figure 3.6. Block diagram of the adaptive feedforward control system.

The controller is menu driven and the user interface enables easy modifications of the system parameters. The parameters used in the EZ-ANC controller are presented and adjusted through a software package. Through this menu modifications to the EZ-ANC system and the adaptive algorithm can be changed to increase the efficiency of the control performance. The adaptive algorithm is the part of the active control system that modifies the weights of the digital filters such that the attenuation of the unwanted vibrational disturbance is maximised.

Table 3.1 shows a complete list of the type and model of the equipment used in the experiments.

Table 3.1 Experimental equipment.

Type of equipment	Name	Type
Accelerometer	Miniature Accelerometer	Brüel & Kjær Type 4375
Signal Analyser	Dual Channel Signal Analyser	Brüel & Kjær Type 2034
Active Controller	EZ-ANC Active controller	Beta 1.13
Personal Computer	Dell Laptop	Inspiron
Shakers	Mini Shaker	LDS Type V203
Signal conditioning amplifier	The NEXUS™ Conditioning Amplifier	Brüel & Kjær Type 2692
Wax	Beeswax	Brüel & Kjær YJ-0216

3.5 Experimental Procedure

The experimental analysis consisted of an active control investigation of the rectangular plate structures. The primary shaker was driven by the Brüel & Kjær dual channel signal analyser source, to generate random noise over a specified frequency range. The shaker was placed on plate 1 at a fixed location (in metres) of (x_p, y_p) = (0.371, 0.19), which resulted in simultaneous excitation of all the structural modes. The response was measured by an accelerometer, and the signal sent to the signal analyser via a charge conditioning amplifier. From the frequency response function of the plate, the natural frequencies could be obtained by zooming in on the peaks. By driving the plate at one of its resonance frequencies, the corresponding operational deflection at this frequency could be obtained. It was assumed that excitation at a single frequency predominantly excites a single mode, and that the forced response or operational deflection at this

frequency represents a single mode. This was achieved by driving the primary shaker using the Variable Sine output in the signal generator. The response of the plate was measured by using a mapping accelerometer. Acceleration measurements were taken at 50-mm intervals in both *x*- and *y*-directions. This mesh allowed for an adequate number of points to be used to obtain an accurate surface plot. Figure 3.7 depicts a schematic diagram of the typical experimental apparatus layout for the uncontrolled experiments.

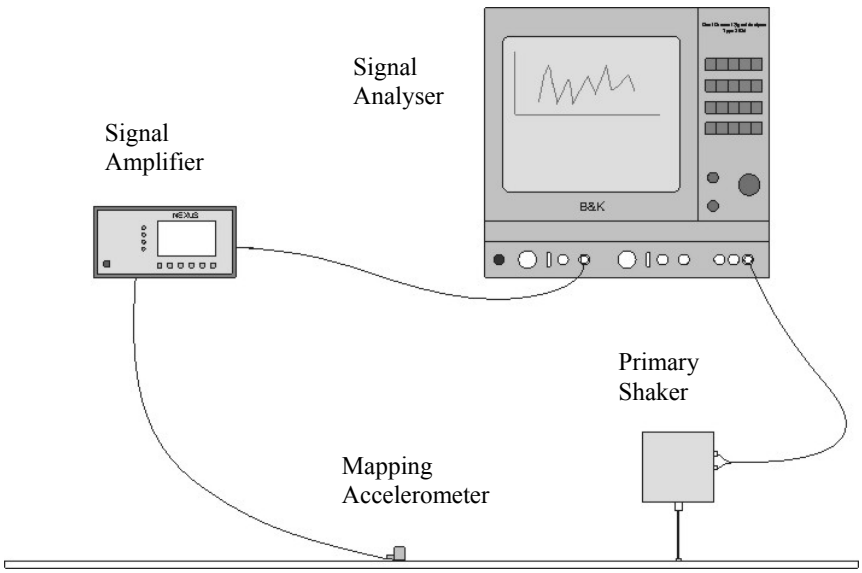

Figure 3.7. Set-up for the experiments performed with only the primary excitation.

In the active control experiments, the primary shaker remained at its fixed location of (x_p, y_p) = (0.371, 0.19). The position of the secondary shaker varied depending on which control arrangement was being investigated. The signal generated by the signal analyzer, which was used to drive the primary shaker, was also fed into the active controller. This input served as a reference signal. An error sensor position was chosen at a location where the plate vibration was to be minimised. An error signal from the

reference accelerometer was fed into the controller. The output signal from the controller was used to drive the secondary shaker. A second "mapping" accelerometer was then used to map the vibration levels of the plate. Accelerometer readings were taken when the active controller was switched off (uncontrolled response) and on (controlled response). Measurements were taken at 50-mm intervals in the *y*-direction and 50-mm intervals in the *x*-direction to obtain an accurate surface plot.

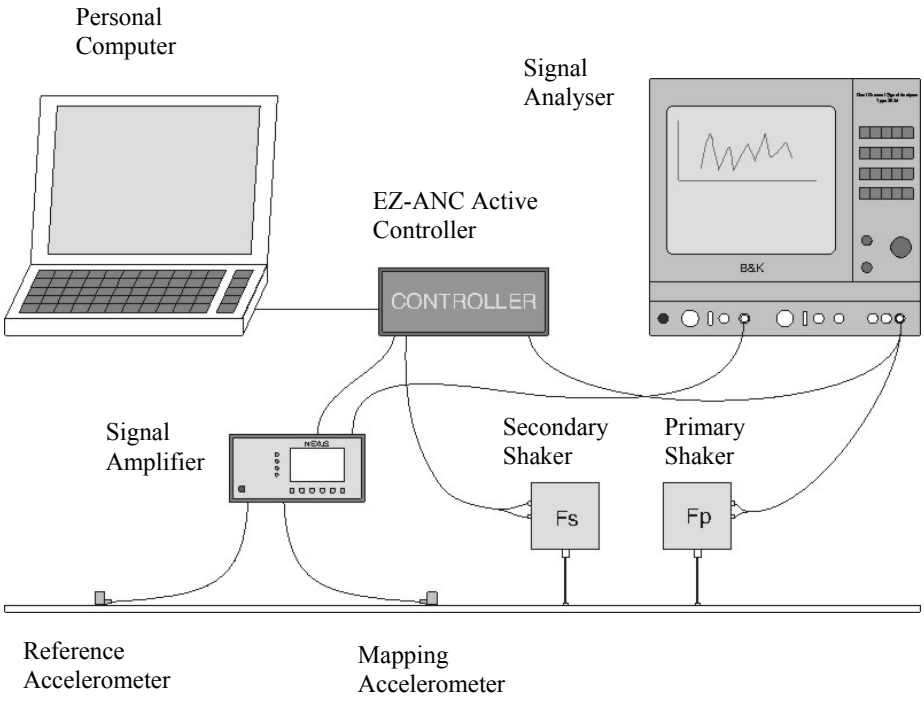

Figure 3.8. Set-up for the active control experiments.

The active control experiment work involved investigating the effect of changing the number and location of the error sensors and secondary forces on the active control performance. During the active control experiments, it was noted that the algorithm stability decreased as the number of control forces and error sensors increased. This in turn decreased the speed of convergence of the system. The system stability and

convergence speed was adjusted by changing the convergence coefficient. The following rules were used in order to choose the optimum value of the convergence coefficient [63]:

- The initial value was small (approximately 100), and gradually increased so that the system did not overload automatically.
- For lower frequency reference signals, the convergence coefficient was less than for the same control set-up with a higher frequency reference signal.
- If any gains in the system were increased, the convergence coefficient value was decreased.
- If the number of control forces or error sensors was increased, the value of the convergence coefficient was decreased.
- If the distance between sources and error sensors was increased, the value of the convergence coefficient was decreased.

For each active control arrangement that was experimentally investigated, the system parameters were adjusted to allow for the optimal control performance for that particular set-up.

CHAPTER 4

RESULTS AND DISCUSSION

4.1 Introduction

Chapter 4 presents the analytical and experimental results obtained for the primary dynamic response and active control of the joined plate structures. Controlled results are initially presented for active control of the coupled plates using a single control force and a single error sensor. Multiple actuators and error sensors in various arrangements are then used to attenuate the response of the plate structures. The number and location of the control forces and error sensors were investigated, and their effects on the control performance were compared. In addition, the effect of the control forces driven dependently and independently was investigated. Both analytical and experimental results are presented for active control of the entire plate response at a low resonance frequency.

A valid comparison of the results for the various control arrangements can only be made if the conditions of the theoretical models accurately reflect those in the physical apparatus. The material parameters of aluminium used in the modelling are density ρ = 2700kg/m^3, Young's modulus $E = 7.1 \times 10^{10}$N/m^2 and Poisson's ratio ν = 0.3. Hysteretic damping in the structure was included by using a complex Young's modulus $E(1 + j\eta)$, where η=0.001 is the structural loss factor. The same dimensions were used as for the experiments, corresponding to $L_x = 600\text{mm}$, $L_y = 500\text{mm}$ and $h = 2\text{mm}$. In each

control case, the primary shaker was placed on plate 1 at a fixed location (in metres) of (x_p, y_p) = (0.371, 0.19), which resulted in simultaneous excitation of all the structural modes. When one control force was used, it was always positioned in line with the primary force in the $x-$direction on plate 1, and in a symmetrical arrangement along the plate width, at (x_{s1}, y_{s1}) = (0.371, 0.31). Results are presented in terms of acceleration levels (in dB). The acceleration was converted to dB using $L_a = 10\log(a/a_{ref})^2$, where $a_{ref} = 10^{-6}$ m/s^2 is the internationally accepted reference value [42]. The primary acceleration distributions in each control case are measured at a location (x_{e1}, y_{e1}) = (0.23, 0.19) on plate 2 which results in simultaneous measurement of all the structural modes.

4.2 L-Shaped Plate Results

Figure 4.1 shows a frequency response plot obtained analytically for the primary and controlled acceleration distributions for a frequency range up to 400Hz, for the L-shaped plate when a single error sensor was placed on plate 2 at (x_{e1}, y_{e1}) = (0.23, 0.25) (dotted line), or at (x_{e1}, y_{e1}) = (0.36, 0.4) (dashed line). The solid line shows the response for an accelerometer location on plate 2 of (x_{e1}, y_{e1}) = (0.23, 0.19), and a primary force location on plate 1 of (x_p, y_p) = (0.371, 0.19). When the error sensor is placed on plate 2 at the first control set-up corresponding to (x_{e1}, y_{e1}) = (0.23, 0.25), it can be seen that the control performance achieved is relatively uniform over the frequency range. This is due to the symmetry of the primary and control force locations with respect to the simply supported

boundary conditions, and the location of the error sensor at the midway point along the width of the plate. The control performance deteriorates when the error sensor is shifted from the midway point of $y_e = L_y / 2 = 0.25$ m, as shown by the controlled results when the error sensor was moved to $(x_{e1}, y_{e1}) = (0.36, 0.4)$. The corresponding optimum control force amplitudes for the two control arrangements in Figure 4.1 are presented in Figure 4.2. Under the symmetrical control arrangement, the control force amplitude is always unity. When the control arrangement is not symmetrical with respect to the primary force location, the optimal control force amplitude varies with frequency.

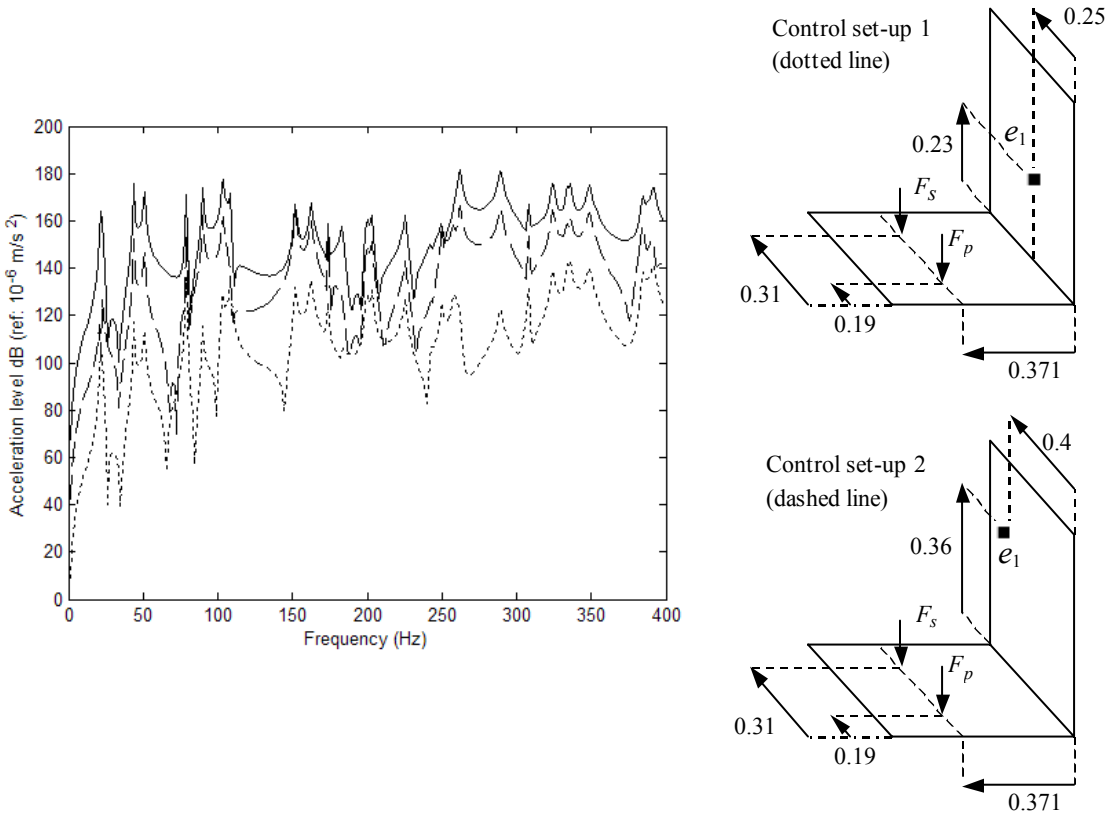

Figure 4.1. Primary (solid line) and controlled frequency responses for the L-shaped plate for an error sensor located on plate 2 at $(x_{e1}, y_{e1}) = (0.23, 0.25)$ (dotted line), or $(x_{e1}, y_{e1}) = (0.36, 0.4)$ (dashed line).

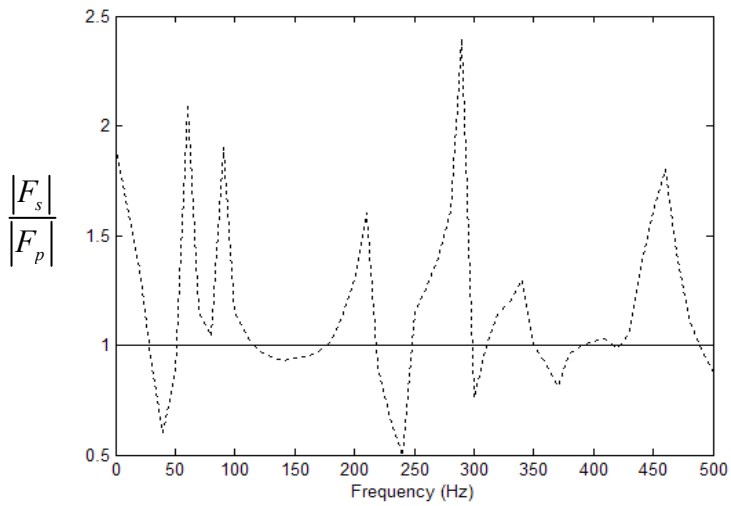

Figure 4.2. Optimal control force amplitude using a single control force located at (x_{s1}, y_{s1}) = (0.371, 0.31) on plate 1 and a single error sensor located on plate 2 at (x_{e1}, y_{e1}) = (0.23, 0.25) (solid line), or (x_{e1}, y_{e1}) = (0.36, 0.4) (dotted line).

Figure 4.3 again shows the primary and controlled acceleration distributions for a frequency range up to 400Hz for the L-shaped plate. The dashed line shows the controlled response when a single error sensor was placed on plate 2 at (x_{e1}, y_{e1}) = (0.23, 0.19). The dotted line shows the controlled response when two error sensors were placed on plate 2 at (x_{e1}, y_{e1}) = (0.23, 0.19) and (x_{e2}, y_{e2}) = (0.23, 0.31). The results indicate that control performance deteriorates when one control force and multiple error sensors are used. This is due to the fact that the single control force has to divide its efforts between the two error signals such that the total squared plate displacement at each error sensor location is minimised. The same trend will be shown for the T and X-shaped plates.

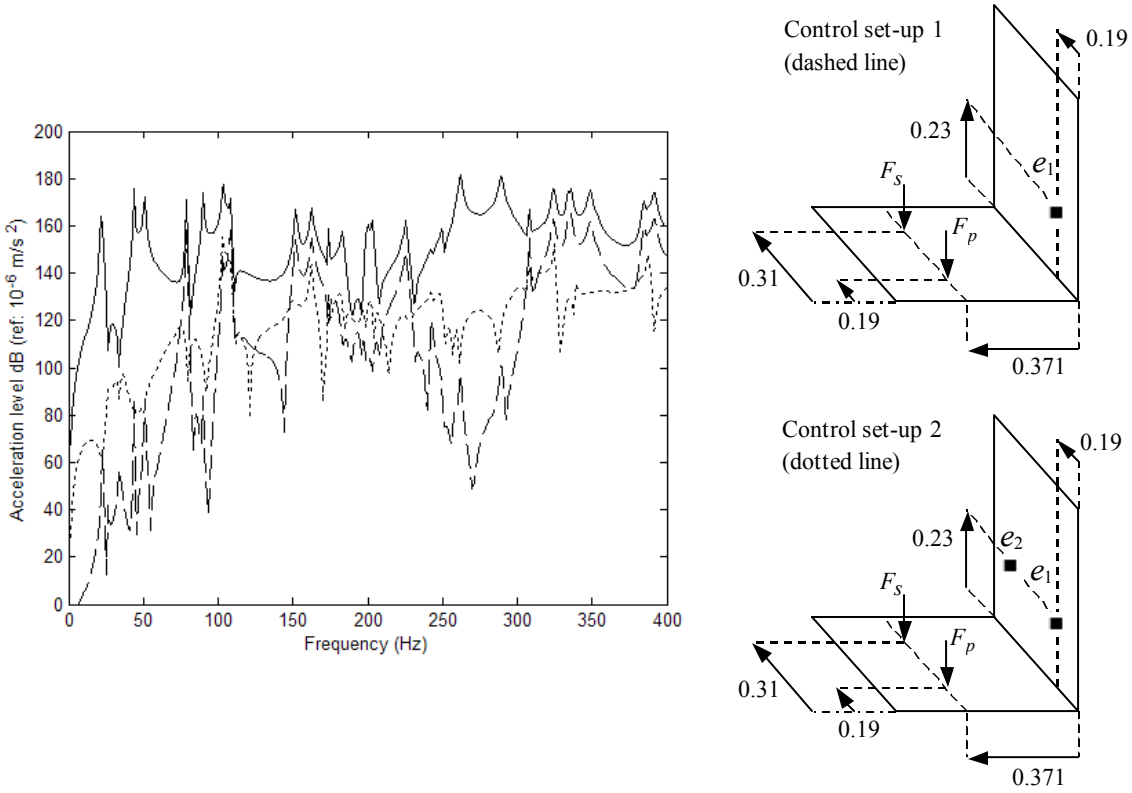

Figure 4.3. Primary (solid line) and controlled frequency response for the L-shaped plate using primary and control forces located at $(x_p, y_p) = (0.371, 0.19)$ and $(x_{s1}, y_{s1}) = (0.371, 0.31)$ respectively, and for an error sensor located on plate 2 at $(x_{e1}, y_{e1}) = (0.23, 0.19)$ (dashed line) and two error sensors located on plate 2 at $(x_{e1}, y_{e1}) = (0.23, 0.19)$ and $(x_{e2}, y_{e2}) = (0.23, 0.31)$ (dotted line).

Figure 4.4 presents the primary and controlled acceleration distributions for two error sensors positioned on plate 2 at $(x_{e1}, y_{e1}) = (0.28, 0.32)$, $(x_{e2}, y_{e2}) = (0.32, 0.45)$, (dotted line), and $(x_{e1}, y_{e1}) = (0.23, 0.25)$, $(x_{e2}, y_{e2}) = (0.28, 0.25)$ (dashed line). The results show that aligning the error sensors at the midway point along the width of the plate

corresponding to $y_e = L_y / 2 = 0.25\,\text{m}$ produces a better control performance than when the error sensors were randomly placed on the plate, and is attributed to the symmetry of the control application.

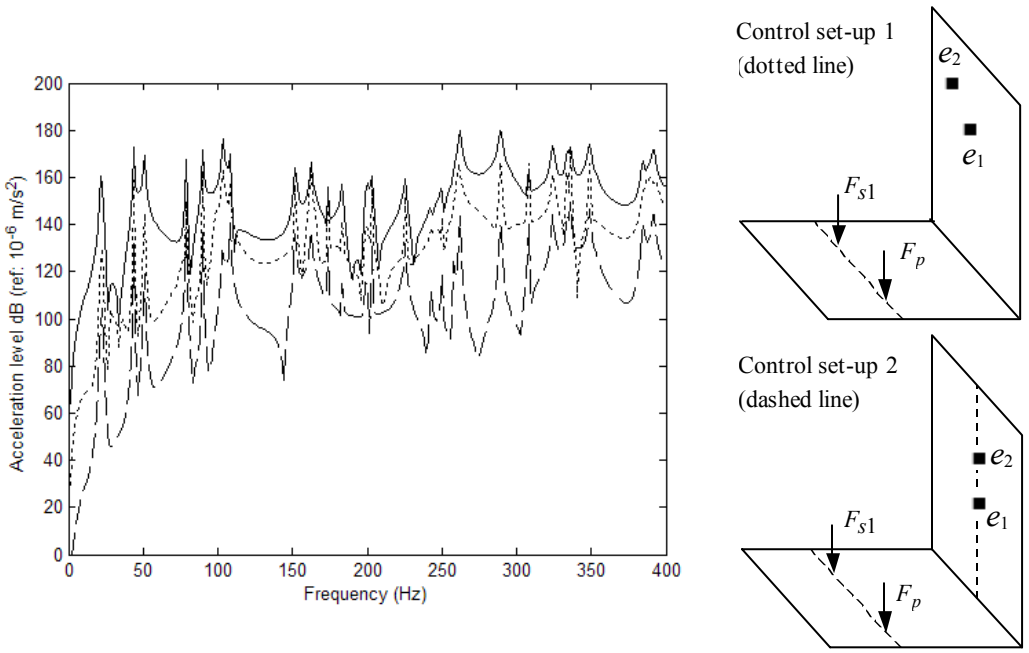

Figure 4.4. Primary (solid line) and controlled frequency responses for the L-shaped plate using two error sensors located on plate 2 at (x_{e1}, y_{e1}) = (0.28, 0.32) (x_{e2}, y_{e2}) = (0.32, 0.45), (dotted line), and (x_{e1}, y_{e1}) = (0.23, 0.25), (x_{e2}, y_{e2}) = (0.28, 0.25) (dashed line).

In order to investigate the effect of active control on the global response of the coupled plates, several modes of vibration were examined. For the L-shaped structure, the uncontrolled and controlled responses for two resonance frequencies were investigated. The analytical vibrational responses were examined at resonance frequencies of

202.95Hz and 224.89Hz. At 224.89Hz the uncontrolled response has only one nodal line running along the $x-$direction at the midway point in the $y-$direction ($y=0.25\,\text{m}$) (Figure 4.5). This corresponds to mode (4,2) of each plate.

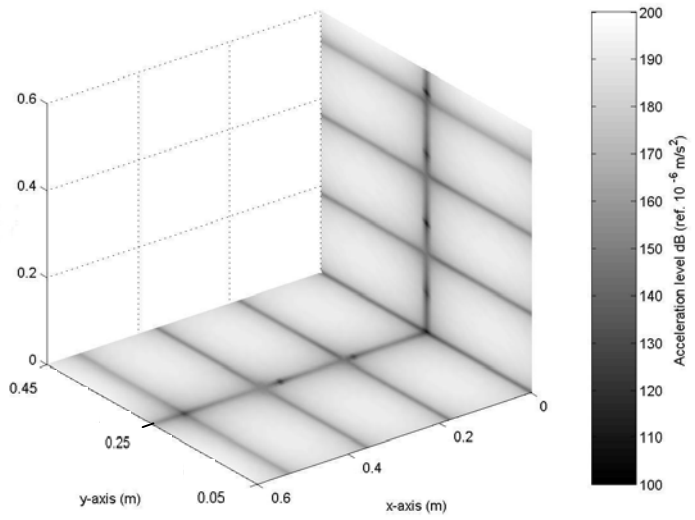

Figure 4.5. Contour plot of the uncontrolled response at 224.89Hz (analytical).

Figures 4.6 and 4.7 respectively show the controlled response using a single control force when the error sensor was located on the nodal line at $(x_{e1}, y_{e1}) = (0.3, 0.25)$ on plate 2, and at an anti-nodal location of $(x_{e1}, y_{e1}) = (0.3, 0.125)$ on plate 2. Figure 4.6 shows that when the error sensor was positioned on a nodal line, attenuation is achieved mainly along the nodal line at $y = 0.25\text{m}$, which corresponds to the midway location in the $y-$direction. The significant attenuation at $y = 0.25\text{m}$ is attributed to the symmetrical arrangement of the primary and control application. When the error sensor was located on an anti-nodal position of $(x_{e1}, y_{e1}) = (0.3, 0.125)$, global attenuation of around 40dB is achieved (Figure 4.7).

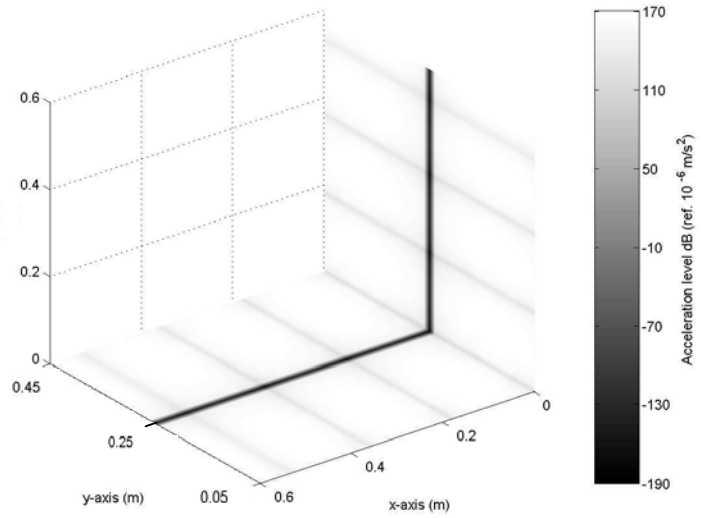

Figure 4.6. Contour plot of the controlled response at 224.89Hz using a single control force at (x_{s1}, y_{s1}) = (0.371, 0.31) and an error sensor located on plate 2 at (x_{e1}, y_{e1}) = (0.3, 0.25).

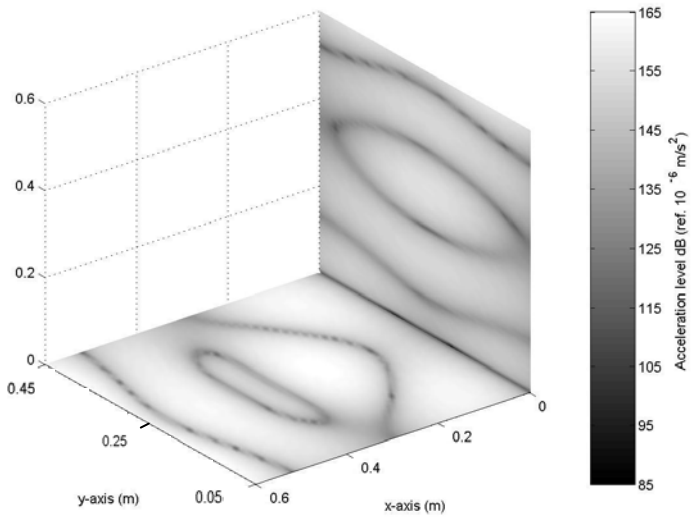

Figure 4.7. Contour plot of the controlled response at 224.89Hz using a single control force at (x_{s1}, y_{s1}) = (0.371, 0.31) and an error sensor located on plate 2 at (x_{e1}, y_{e1}) = (0.3, 0.125).

Active control experiments were carried out on the L-shaped plate to verify the results of the global response obtained analytically. Figure 4.8 shows the uncontrolled contour plot for a resonance frequency of 221.63Hz. This corresponds to mode (4,2) of each plate. The same control arrangements were used in the experiments as for the analytical investigation. Figures 4.9 and 4.10 show the controlled responses obtained experimentally at the natural frequency of 221.63Hz, for the fixed control force location, and an error sensor located on the nodal line at $(x_{e1}, y_{e1}) = (0.3, 0.25)$ on plate 2 (Figure 4.9), and at an anti-nodal location of $(x_{e1}, y_{e1}) = (0.3, 0.125)$ on plate 2 (Figure 4.10). As expected, better attenuation levels were achieved for the anti-nodal control set-up.

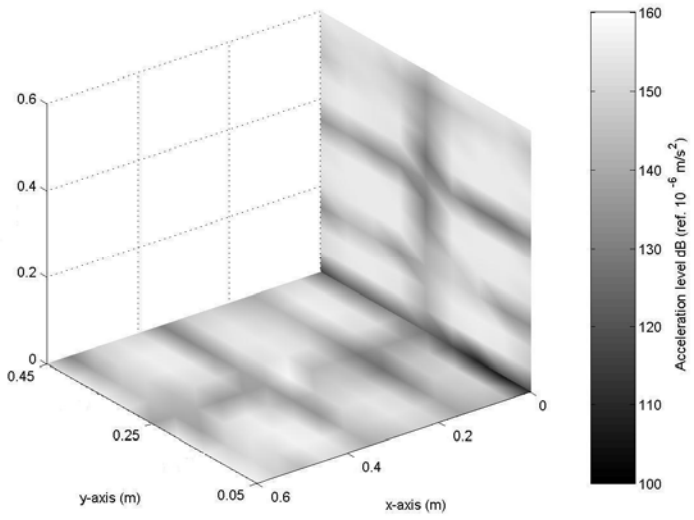

Figure 4.8. Experimental contour plot of the uncontrolled response at 221.63Hz.

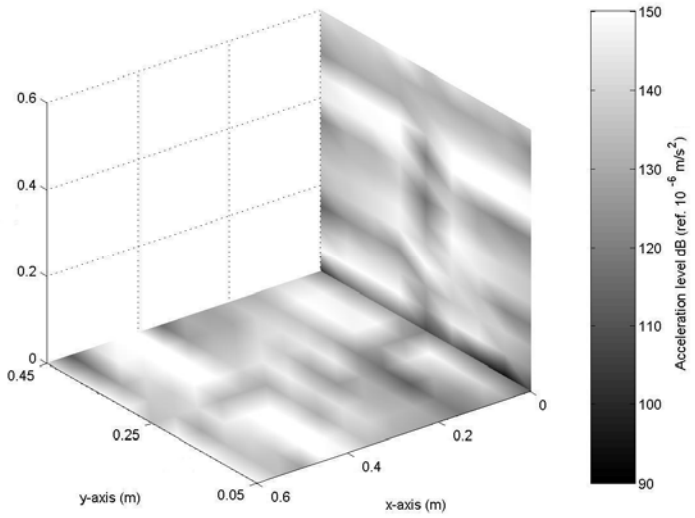

Figure 4.9. Experimental contour plot of the controlled response at 221.63Hz f using a single force at $(x_{s1}, y_{s1}) = (0.371, 0.31)$ and an error sensor located on plate 2 at $(x_{e1}, y_{e1}) = (0.3, 0.25)$.

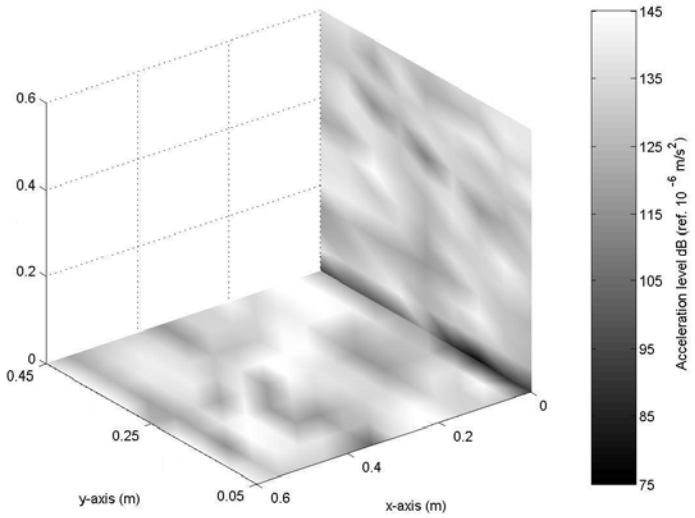

Figure 4.10. Experimental contour plot of the controlled response at 221.63Hz using a single force at $(x_{s1}, y_{s1}) = (0.371, 0.31)$ and an error sensor located on plate 2 at $(x_{e1}, y_{e1}) = (0.3, 0.125)$.

At 202.95Hz, the uncontrolled response obtained analytically has two nodal lines running along the $x-$direction (Figure 4.11). This corresponds to mode (2,3) of each plate. Figure 4.12 shows the controlled response at the resonance frequency of 202.95Hz when the error sensor was positioned on plate 1 at $(x_{e1}, y_{e1}) = (0.2, 0.25)$. This corresponds to an anti-nodal location and is also midway between and downstream of the primary and control actuators. Figure 4.12 shows that global attenuation in both plates is achieved, with up to 45dB attenuation at the anti-nodal locations. Similar attenuation levels were achieved when the error sensor was positioned at any $x-$location on plates 1 and 2, and $y_e = 0.25$. That is, the control performance is independent of the $x-$location for an error sensor at the midway point in the $y-$direction of $y_e = 0.25$. The optimal control performance is attributed to the symmetrical arrangement of the control force and the error sensor with respect to the primary force location. At error sensor locations away from $y_e = 0.25$, the control performance was shown to deteriorate. When the error sensor was located at the intersection of a nodal point in both the $x-$ and $y-$directions, for example, at $(x_{e1}, y_{e1}) = (0.425, 0.34)$, no attenuation of the primary response was achieved.

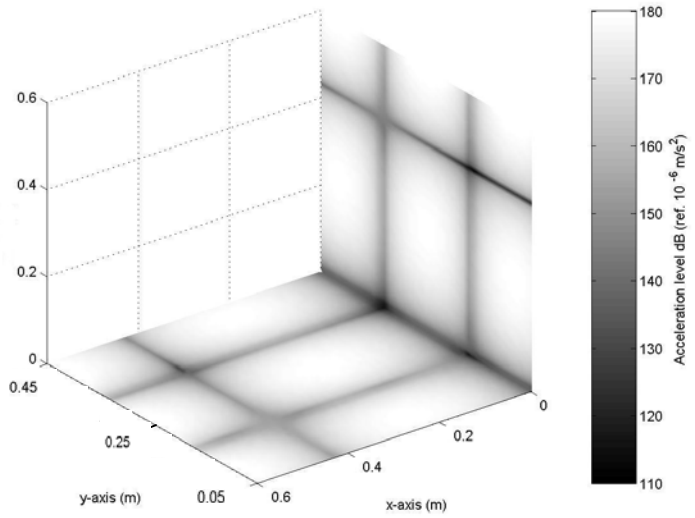

Figure 4.11. Contour plot of the uncontrolled response at 202.95Hz (analytical).

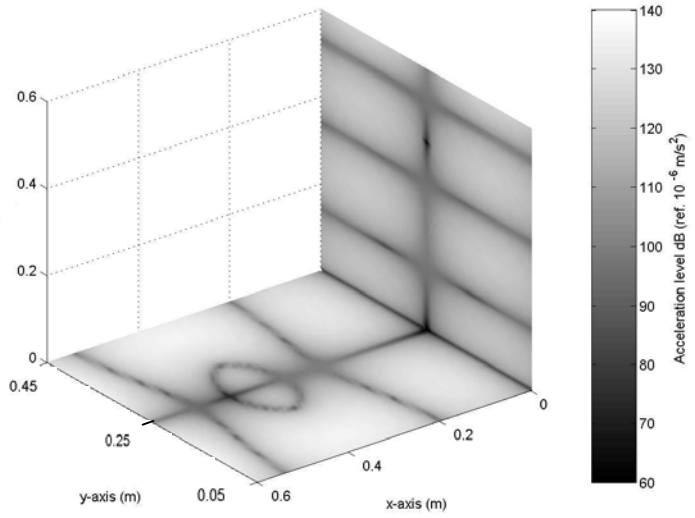

Figure 4.12. Contour plot of the controlled response at 202.95Hz using a single force at (x_{s1}, y_{s1}) = (0.371, 0.31) and an error sensor located on plate 1 at (x_{e1}, y_{e1}) = (0.2, 0.25).

Figures 4.13 and 4.14 show the contour plots of the attenuation levels using two control forces located on plate 1 which are driven dependently and independently respectively, at locations of (x_{s1}, y_{s1}) = (0.371, 0.25) and (x_{s2}, y_{s2}) = (0.371, 0.31), and two error sensors positioned on plate 2 at (x_{e1}, y_{e1}) = (0.3, 0.25) and (x_{e2}, y_{e2}) = (0.4, 0.25). In each case, global attenuation was achieved, however the independently driven control forces achieved significantly better overall attenuation levels than the dependently driven control forces. The dependently driven control forces are equivalent to a single distributed control force, and hence the performance is expected to be less than that of a system with two independently driven control forces.

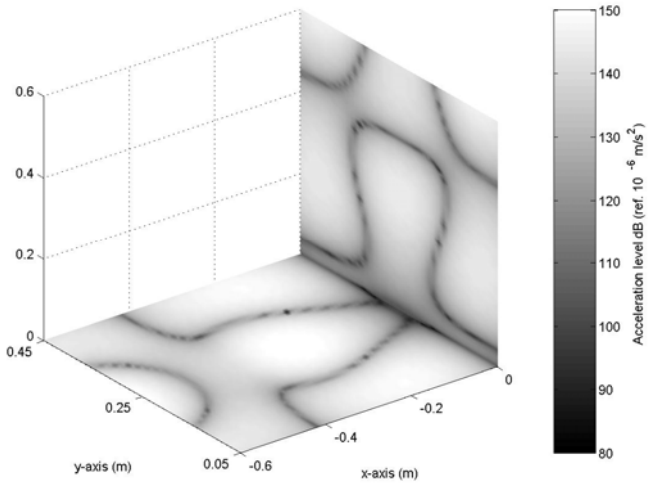

Figure 4.13. Contour plot of the controlled response at 202.95Hz using two dependently driven control forces at (x_{s1}, y_{s1}) = (0.371, 0.31), (x_{s2}, y_{s2}) = (0.371, 0.25) and two error sensors located on plate 2 at (x_{e1}, y_{e1}) = (0.3, 0.25) and (x_{e2}, y_{e2}) = (0.4, 0.25).

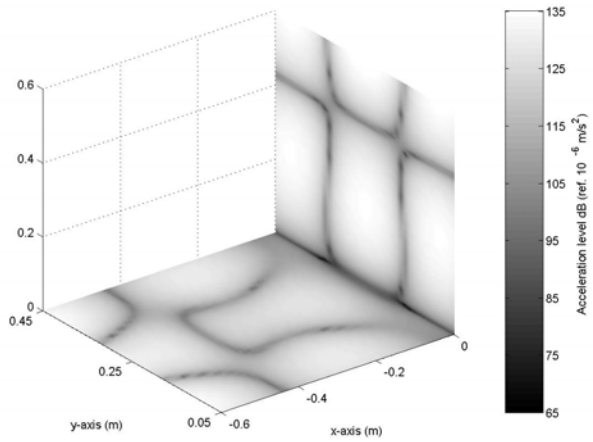

Figure 4.14. Contour plot of the controlled response at 202.95Hz using two independently driven control forces at (x_{s1}, y_{s1})= (0.371, 0.31), (x_{s2}, y_{s2})= (0.371, 0.25) and two error sensors located on plate 2 at (x_{e1}, y_{e1}) = (0.3, 0.25) and (x_{e2}, y_{e2}) = (0.4, 0.25).

Experiments were conducted to confirm the results of the global response obtained analytically, by examining the primary response with two nodal lines running along the $x-$direction, at a resonance frequency of 191.25Hz. This corresponds to mode (1,3) of each plate as shown in Figure 4.15.

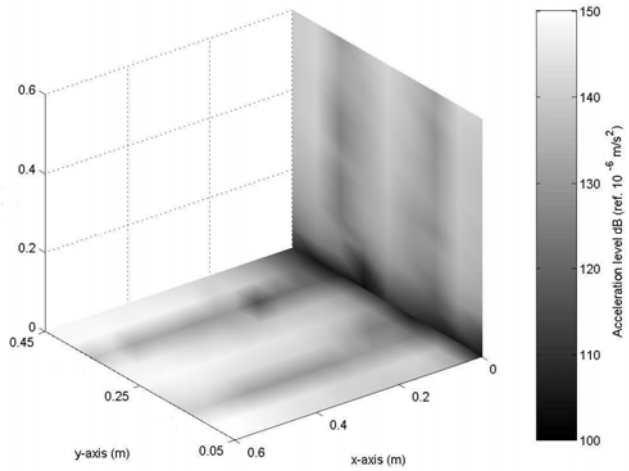

Figure 4.15. Experimental contour plot of the uncontrolled response at 191.25Hz.

Figure 4.16 shows the controlled responses obtained experimentally at the resonance frequency of 191.25Hz using a single control force and a single error sensor optimally located at the midway point along the width of the plate at (x_{e1}, y_{e1}) = (0.2, 0.25) on plate 1. Global attenuation of approximately 15dB was experienced over the entire L-shaped plate surface. Figure 4.17 shows the contour plot of the controlled response at 191.25Hz for one control force at (x_{s1}, y_{s1}) = (0.371, 0.31) and two error sensors located on plate 2 at (x_{e1}, y_{e1}) = (0.3, 0.25) and (x_{e2}, y_{e2}) = (0.4, 0.25). The control performance deteriorates when a single control force and multiple error sensors are used. This is again due to the fact that the single control force has to divide its efforts between the two error signals such that the acceleration at each error sensor location is minimised.

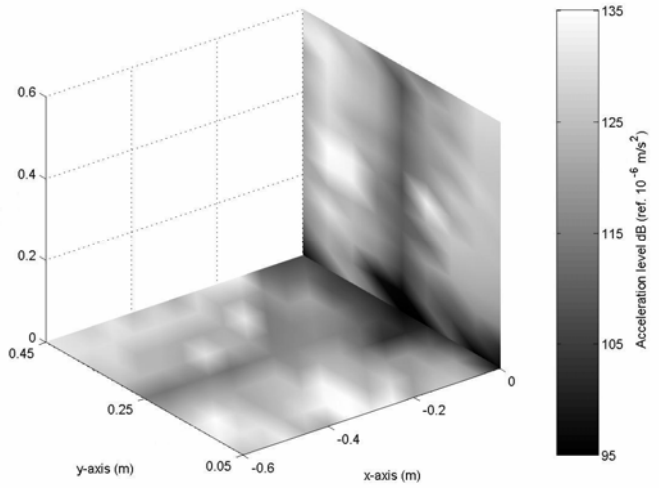

Figure 4.16. Contour plot of the controlled response at 191.25Hz using a single force at (x_{s1}, y_{s1}) = (0.371, 0.31) and an error sensor located on plate 1 at (x_{e1}, y_{e1}) = (0.2, 0.25).

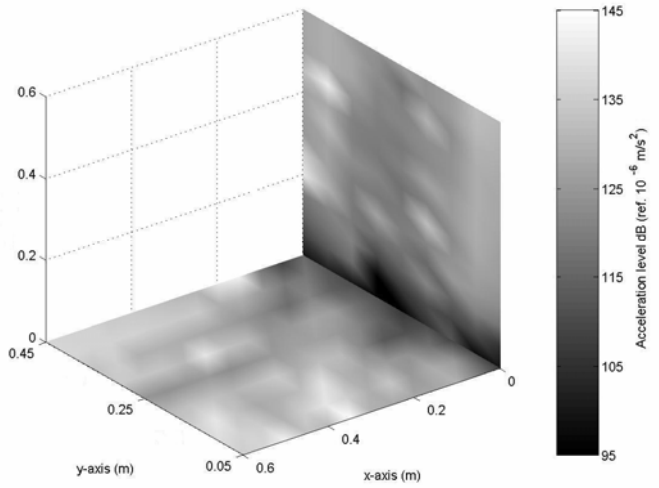

Figure 4.17. Contour plot of the controlled response at 191.25Hz using a single force at (x_{s1}, y_{s1}) = (0.371, 0.31) and two error sensors located on plate 1 plate 2 at (x_{e1}, y_{e1}) = (0.3, 0.25) and (x_{e2}, y_{e2}) = (0.4, 0.25).

Figures 4.18 and 4.19 respectively show the experimental contour plot of the controlled response at 191.25Hz, for two dependently and two independently driven control forces

at (x_{s1}, y_{s1}) = (0.371, 0.25), (x_{s2}, y_{s2}) = (0.371, 0.31), and two error sensors positioned on plate 2 at (x_{e1}, y_{e1}) = (0.3, 0.25), (x_{e2}, y_{e2}) = (0.4, 0.25). Global attenuation of the L-shaped plate is achieved in both cases, although slightly better overall attenuation levels are achieved using independently driven control forces than the dependently driven control forces.

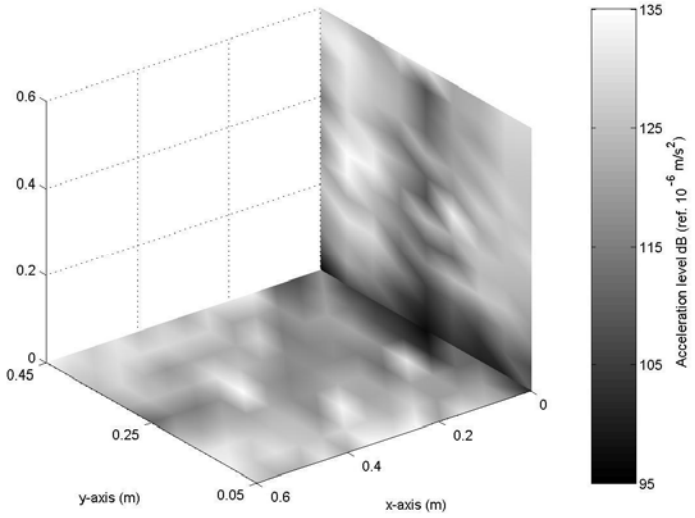

Figure 4.18. Contour plot of the controlled response at 191.25Hz using two dependently driven control forces at (x_{s1}, y_{s1}) = (0.371, 0.31), (x_{s2}, y_{s2}) = (0.371, 0.25) and two error sensors located on plate 2 at (x_{e1}, y_{e1}) = (0.3, 0.25) and (x_{e2}, y_{e2}) = (0.4, 0.25).

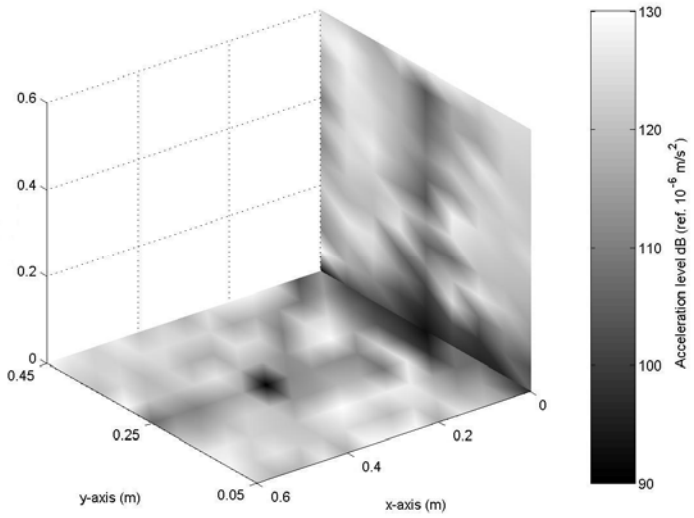

Figure 4.19. Contour plot of the controlled response at 191.25Hz using two independently driven control forces at (x_{s1}, y_{s1})= (0.371, 0.31), (x_{s2}, y_{s2})= (0.371, 0.25) and two error sensors located on plate 2 at (x_{e1}, y_{e1}) = (0.3, 0.25) and (x_{e2}, y_{e2}) = (0.4, 0.25).

4.3 T-Shaped Plate Results

The following section presents the analytical and experimental results for the T-shaped plate. Very similar trends to the L-shaped plate control results can be observed for the T-shaped plate control results.

Figure 4.20 presents the primary and controlled acceleration distributions for a frequency range up to 400Hz for the T-shaped plate, using a single control force, and a single error sensor on plate 2 at (x_{e1}, y_{e1}) = (0.23, 0.25) (dotted line), or at (x_{e1}, y_{e1}) = (0.36, 0.4) (dashed line). In the first control set-up corresponding to (x_{e1}, y_{e1}) = (0.23, 0.25), it can be

shown that the control performance achieved is relatively uniform over the frequency range.

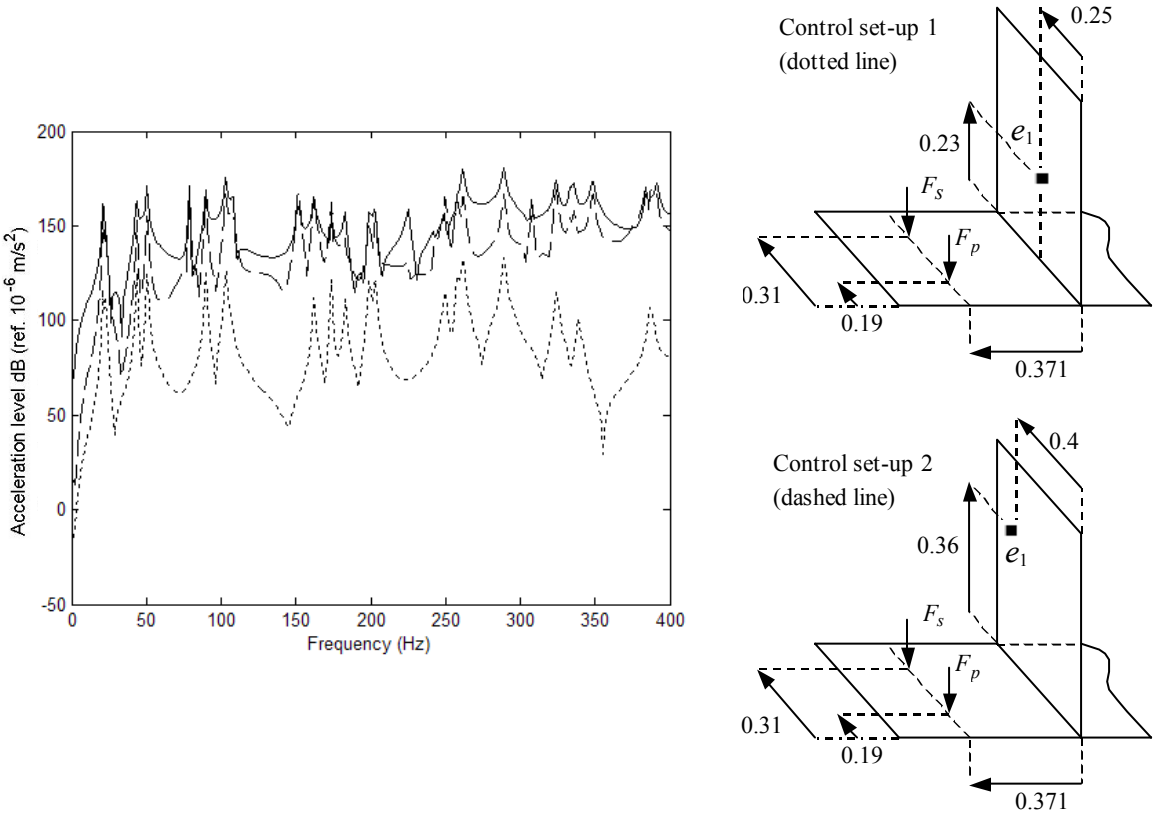

Figure 4.20. Primary (solid line) and controlled frequency responses for the T-shaped plate using primary and control forces located at $(x_p, y_p) = (0.371, 0.19)$ and $(x_{s1}, y_{s1}) = (0.371, 0.31)$ respectively, for an error sensor located on plate 2 at $(x_{e1}, y_{e1}) = (0.23, 0.25)$ (dotted line), or $(x_{e1}, y_{e1}) = (0.36, 0.4)$ (dashed line).

This control performance is attributed to the symmetry of the control force and error sensor locations with respect to the primary force location. The control performance

deteriorates when the error sensor is shifted from the midway point along the width of the plate at $y_e = L_y / 2 = 0.25\,\text{m}$. Under the symmetrical control arrangement, the control force amplitude is always unity. These control results are also confirmed when the error sensor was placed at a midway point of y_e = 0.25m on plates 1 and 3. When the control arrangement is not symmetrical with respect to the primary force location, the control force amplitude fluctuates with frequency, and the control performance deteriorates.

Figure 4.21 compares the primary and controlled acceleration distributions for a frequency range up to 400Hz for the T-shaped plate when a single error sensor was placed on plate 2 at (x_{e1}, y_{e1}) = (0.23, 0.19) (dashed line), and two error sensors were placed on plate 2 at (x_{e1}, y_{e1}) = (0.23, 0.19) and (x_{e2}, y_{e2}) = (0.23, 0.31) (dotted line). It can be seen that that the control performance deteriorates when one control force and multiple error sensors are used. This is due to the fact that the single control force has to divide its efforts between the two error signals such that the total squared plate displacement at each error sensor location is minimised.

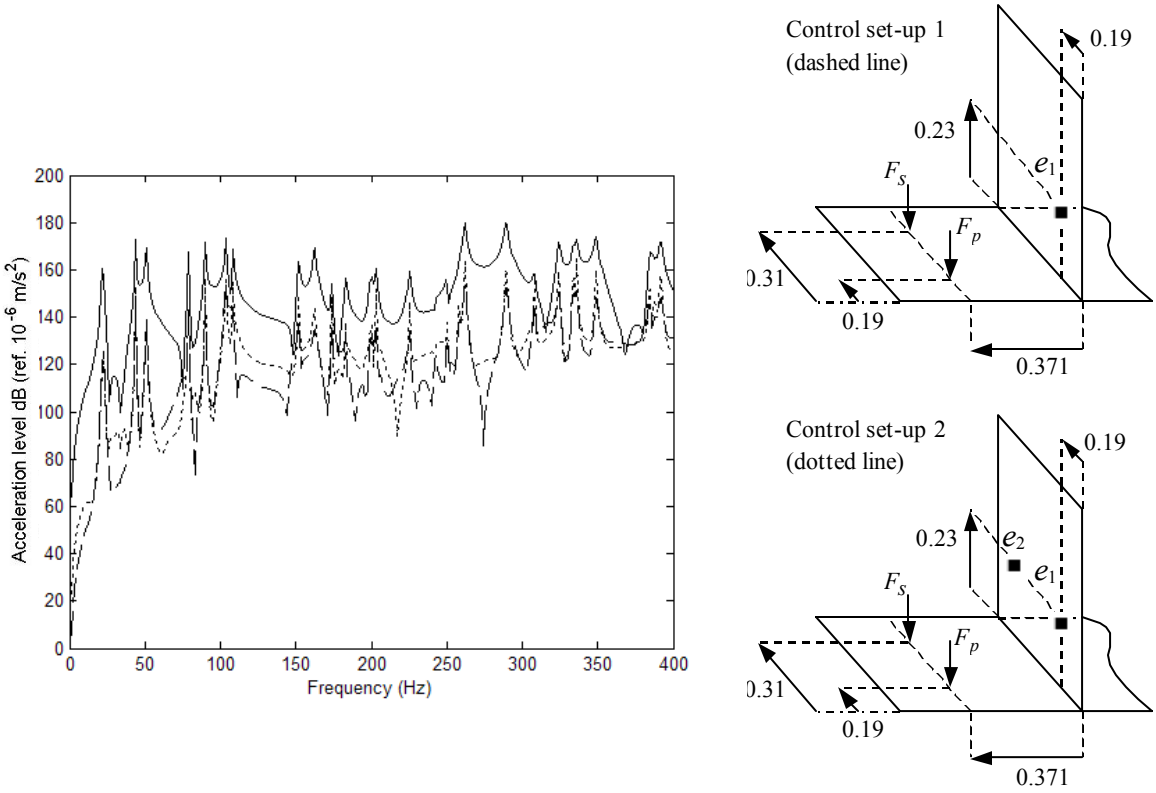

Figure 4.21. Primary (solid line) and controlled frequency response for the T-shaped plate using primary and control forces located at $(x_p, y_p) = (0.371, 0.19)$ and $(x_{s1}, y_{s1}) = (0.371, 0.31)$ respectively, and for an error sensor located on plate 2 at $(x_{e1}, y_{e1}) = (0.23, 0.19)$ (dashed line) and two error sensors located on plate 2 at $(x_{e1}, y_{e1}) = (0.23, 0.19)$ and $(x_{e2}, y_{e2}) = (0.23, 0.31)$ (dotted line).

The effect of the error sensor locations was initially investigated using two dependently driven control forces to simultaneously minimise the response at two error sensors. Figure 4.22 presents the primary and controlled acceleration distributions for a frequency range up to 400Hz for the T-shaped plate. The two control forces are fixed on plate 1 at

the same $x-$location as the primary force at (x_{s1}, y_{s1}) = (0.371, 0.25) and (x_{s2}, y_{s2}) = (0.371, 0.31). Two error sensors positioned on plate 2 at (x_{e1}, y_{e1}) = (0.23, 0.19), (x_{e2}, y_{e2}) = (0.23, 0.31) are compared with the sensors located at (x_{e1}, y_{e1}) = (0.23, 0.25), (x_{e2}, y_{e2}) = (0.28, 0.25). The results show that aligning the error sensors at the midway point along the width of the plate corresponding to $y_e = L_y / 2 = 0.25\,\text{m}$ produces better attenuation levels than when the error sensors are moved away from the midway point. This is attributed to the relatively symmetrical arrangement of the locations of the control forces and error sensors with respect to the primary force location.

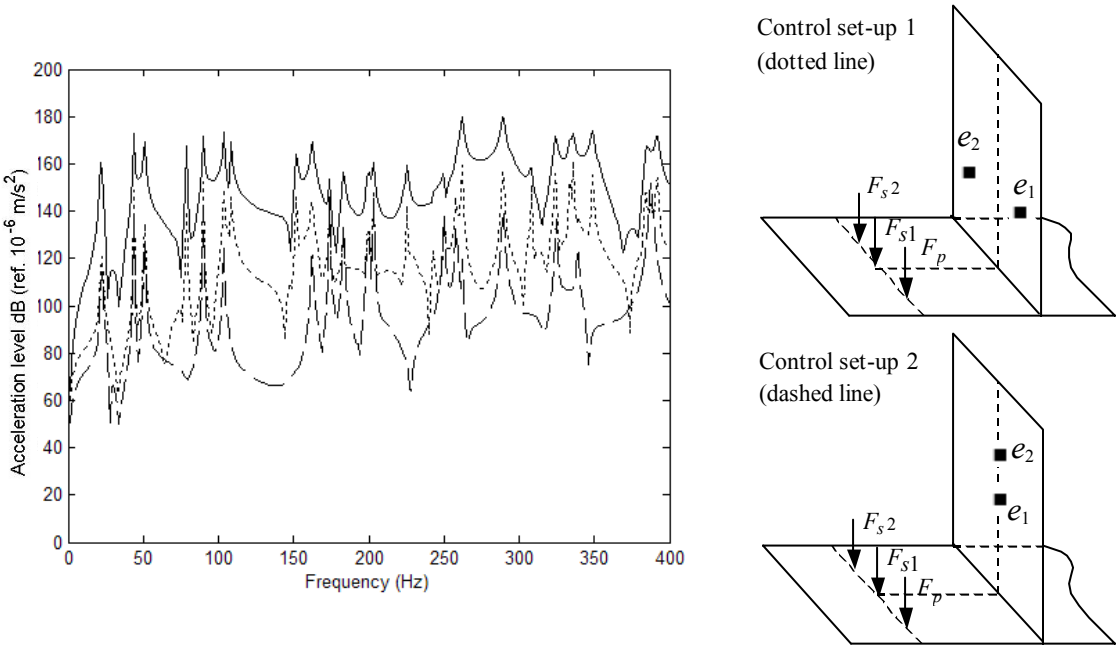

Figure 4.22. Primary (solid line) and controlled frequency responses for the T-shaped plate using two dependently driven control forces and two error sensors located on plate 2 at (x_{e1}, y_{e1}) = (0.23, 0.19), (x_{e2}, y_{e2}) = (0.23, 0.31) (dotted line), and (x_{e1}, y_{e1}) = (0.23, 0.25), (x_{e2}, y_{e2}) = (0.28, 0.25) (dashed line).

The corresponding optimum control force amplitudes are presented in Figure 4.23 for the two combinations. Large control force amplitudes are required at various discrete resonance frequencies when the error sensors were not positioned midway along the width of the plate. When the error sensors are located at the midway point, the control force amplitude for two dependently driven control forces is fairly constant at 0.5. Hence, each control force is being driven at around half the amplitude of the primary force, and is also being driven at around half the amplitude of the optimal control force using the symmetrical control arrangement consisting of a single control force and a single error sensor, as presented in the first control set-up in Figure 4.20.

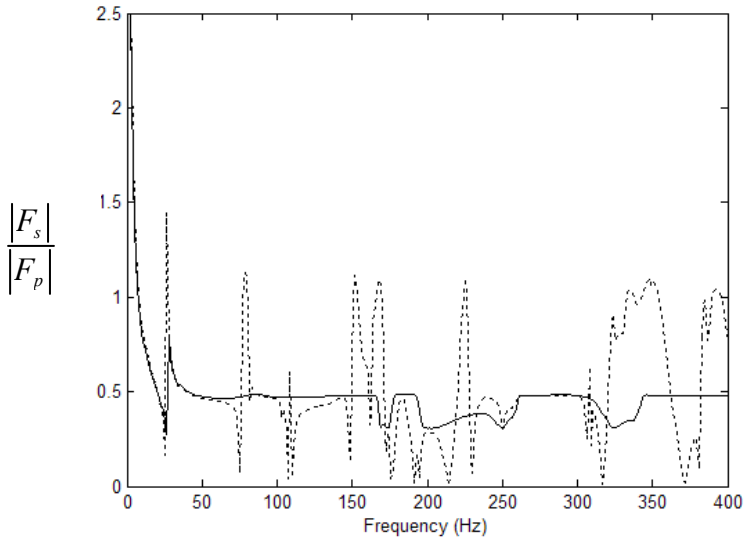

Figure 4.23. Optimal control force amplitude using two dependently driven control forces and two error sensors located on plate 2 at (x_{e1}, y_{e1}) = (0.23, 0.19), (x_{e2}, y_{e2}) = (0.23, 0.31) (dotted line), and (x_{e1}, y_{e1}) = (0.23, 0.25), (x_{e2}, y_{e2}) = (0.28, 0.25) (solid line).

The effect of the control force locations was then investigated for two fixed error sensors located on plate 2 at (x_{e1}, y_{e1}) = (0.23, 0.19), (x_{e2}, y_{e2}) = (0.23, 0.31). Two dependently driven control forces located on plate 1 in line with the primary force along the $x-$direction at (x_{s1}, y_{s1}) = (0.371, 0.25), (x_{s2}, y_{s2}) = (0.371, 0.31), were compared with two arbitrarily located forces at (x_{s1}, y_{s1}) = (0.17, 0.4), (x_{s2}, y_{s2}) = (0.45, 0.29). Figure 4.24 shows that changing the control force locations has very little effect on the control performance. This result was also observed using two independently driven control forces. Hence, the use of two control forces to minimise the response at two error sensor locations will result in global attenuation of the primary frequency response.

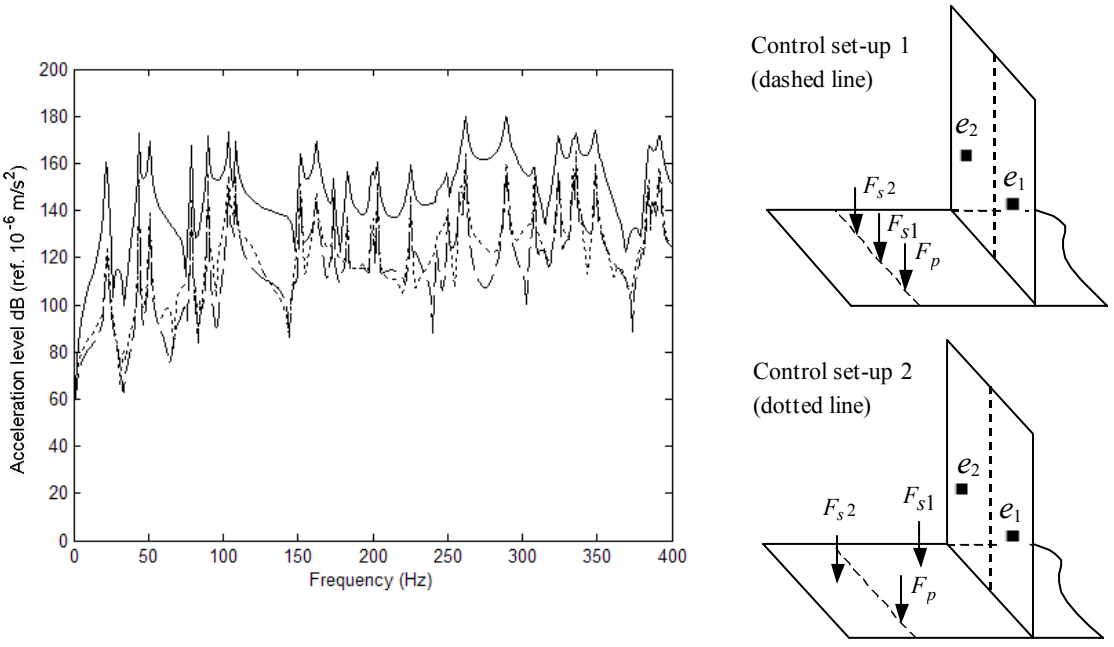

Figure 4.24. Primary (solid line) and controlled frequency responses for the T-shaped plate using two dependently driven control forces located on plate 1 at (x_{s1}, y_{s1}) = (0.371, 0.25), (x_{s2}, y_{s2}) = (0.371, 0.31) (dashed line), and (x_{s1}, y_{s1}) = (0.17, 0.4), (x_{s2}, y_{s2}) = (0.45, 0.29) (dotted line).

The effect of varying the number of dependently driven control forces was then investigated for fixed error sensor positions. Further investigation shows that the use of three control forces and two error sensors produced no significant improvement in the control performance when compared to the two-control force, two-error sensor arrangement. Slightly higher attenuation levels can be achieved using a control set-up consisting of three control forces and three error sensors compared to using two control forces and two error sensors.

Figures 4.25 and 4.26 compare the performance for two control forces driven dependently and independently. In Figure 4.25, the control application is relatively symmetrical with respect to the primary force location, with the control forces located in-line with the primary force on plate 1 at (x_{s1}, y_{s1}) = (0.371, 0.25) and (x_{s2}, y_{s2}) = (0.371, 0.31), and the error sensors are located at the midway point along the width of plate 2 at (x_{e1}, y_{e1}) = (0.23, 0.25), (x_{e2}, y_{e2}) = (0.28, 0.25).

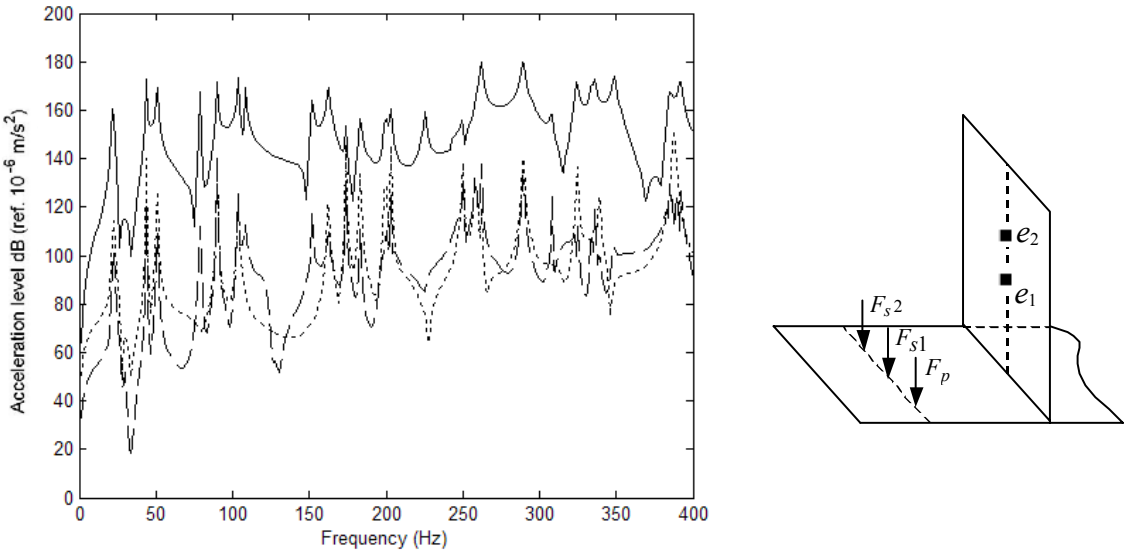

Figure 4.25. Primary (solid line) and controlled frequency responses for the T-shaped plate using two dependently (dotted line) and two independently (dashed line) driven control forces located at (x_{s1}, y_{s1}) = (0.371, 0.25) and (x_{s2}, y_{s2}) = (0.371, 0.31) and two error sensors located on plate 2 at (x_{e1}, y_{e1}) = (0.23, 0.25), (x_{e2}, y_{e2}) = (0.28, 0.25).

In Figure 4.26, the control forces and error sensors are arbitrarily located, with the control forces located in line with the primary force on plate 1 at (x_{s1}, y_{s1}) = (0.17, 0.4) and (x_{s2}, y_{s2}) = (0.45, 0.29), and the error sensors located on plates 2 and 3 respectively at (x_{e1}, y_{e1}) = (0.17, 0.19) and (x_{e2}, y_{e2}) = (0.36, 0.4). With the relatively symmetrical control arrangement (Figure 4.25), the attenuation levels achieved are very similar using dependently or independently driven control forces. However, for any arbitrary control arrangement as shown in Figure 4.26, the independently driven control force arrangement

produces significantly better attenuation levels than the dependently driven control set-up.

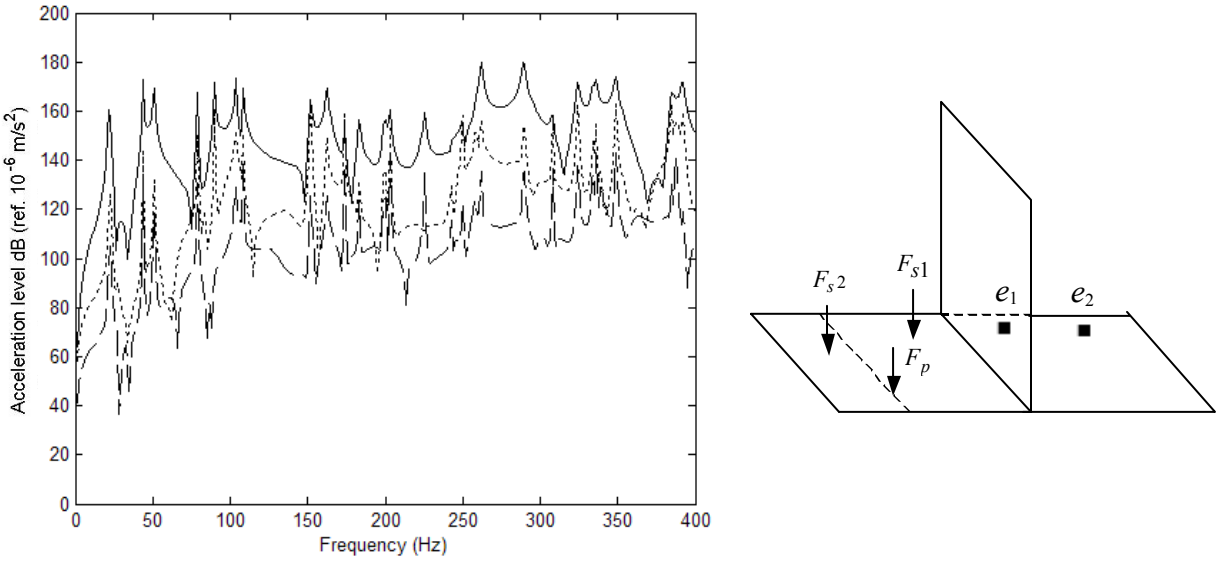

Figure 4.26. Primary (solid line) and controlled frequency responses for the T-shaped plate using two dependently (dotted line) and two independently (dashed line) driven control forces located at (x_{s1}, y_{s1}) = (0.17, 0.4) and (x_{s2}, y_{s2}) = (0.45, 0.29), and two error sensors located on plates 2 and 3 at respectively (x_{e1}, y_{e1}) = (0.17, 0.19) and (x_{e2}, y_{e2}) = (0.36, 0.4).

To investigate the effect of active control on the global response of the T-shaped plate, a low resonance frequency of 90Hz was examined. This is the fourth natural frequency of the T-shaped plate, and corresponds to mode (3,1) of each plate. Various combinations of control force and error sensor arrangements were used, and their effect on control

performance was observed. Figure 4.27 shows that the uncontrolled response for the resonance frequency of 90Hz has no nodal lines running along the $x-$direction.

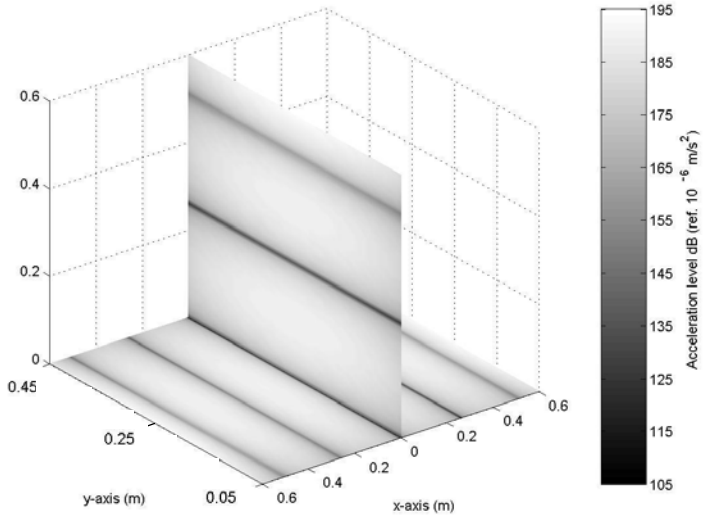

Figure 4.27. Contour plot of the uncontrolled response at 90Hz (analytical).

Figures 4.28 and 4.29 show the controlled responses for the resonance frequency of 90Hz for two different control configurations, each consisting of one error sensor and one control force. In both cases, the control force was placed in-line along the $x-$direction with the primary force at (x_{s1}, y_{s1}) = (0.371, 0.31), and is also in a symmetrical arrangement with respect to the simply supported boundary conditions. Figure 4.28 shows that global attenuation was achieved when the error sensor was placed on plate 2 at (x_{e1}, y_{e1}) = (0.23, 0.25), which corresponds to the midway point along the width of the T-shaped plate. This symmetrical control arrangement with respect to the simply supported boundary conditions produces the best control results for the one control force, one error sensor application. Figure 4.29 displays the controlled response when the error sensor

was randomly placed on plate 2 at (x_{e2}, y_{e2}) = (0.43, 0.375). Global attenuation is still achieved, however the control performance deteriorates once the error sensor is moved away from the symmetrical arrangement of y_e = 0.25 corresponding to the midway point along the plate width.

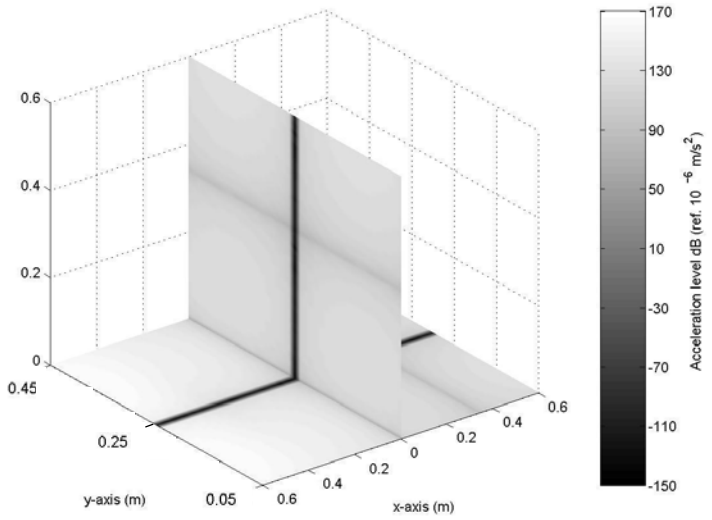

Figure 4.28. Contour plot of the controlled response at 90Hz for one control force at (x_{s1}, y_{s1}) = (0.371, 0.31) and an error sensor located on plate 2 at (x_{e1}, y_{e1}) = (0.23, 0.25).

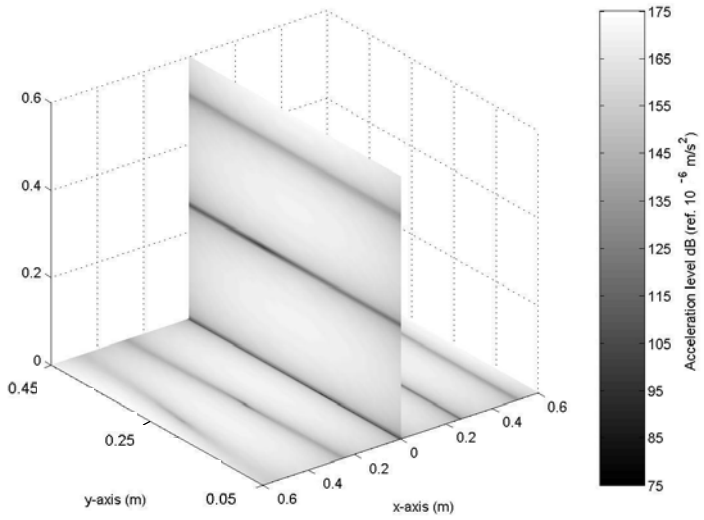

Figure 4.29. Contour plot of the controlled response at 90Hz for one control force at (x_{s1}, y_{s1}) = (0.371, 0.31) and an error sensor located on plate 2 at (x_{e1}, y_{e1}) = (0.43, 0.375).

Figures 4.30 and 4.31 show the contour plots of the attenuation levels using two dependently driven control forces located at (x_{s1}, y_{s1}) = (0.371, 0.25) and (x_{s2}, y_{s2}) = (0.371, 0.31), and two error sensors positioned on plate 2 at (x_{e1}, y_{e1}) = (0.23, 0.19) and (x_{e2}, y_{e2}) = (0.23, 0.31) (Figure 4.30), and (x_{e1}, y_{e1}) = (0.23, 0.25) and (x_{e2}, y_{e2}) = (0.28, 0.25) (Figure 4.31). In each case, global attenuation was achieved, and the control performance is not as dependent on the error sensor locations compared with using a single control force and a single error sensor. The improvement in control performance by using three control forces and multiple error sensors as opposed to two control forces and two error sensors is negligible.

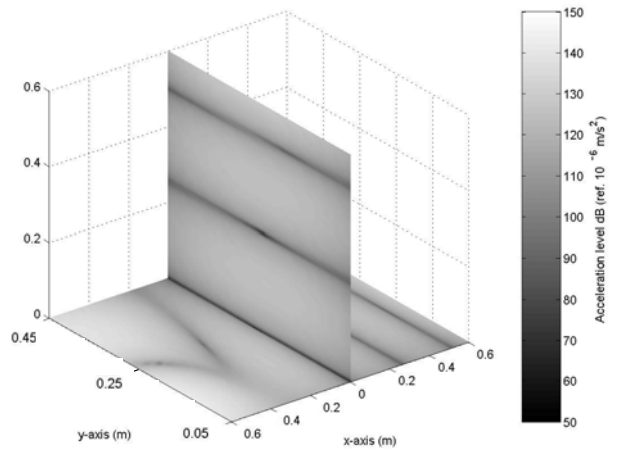

Figure 4.30. Contour plot of the controlled response at 90Hz for two dependently driven control forces at (x_{s1}, y_{s1})= (0.371, 0.31), (x_{s2}, y_{s2})= (0.371, 0.25) and two error sensors located on plate 2 at (x_{e1}, y_{e1}) = (0.23, 0.19) and (x_{e2}, y_{e2}) = (0.23, 0.31).

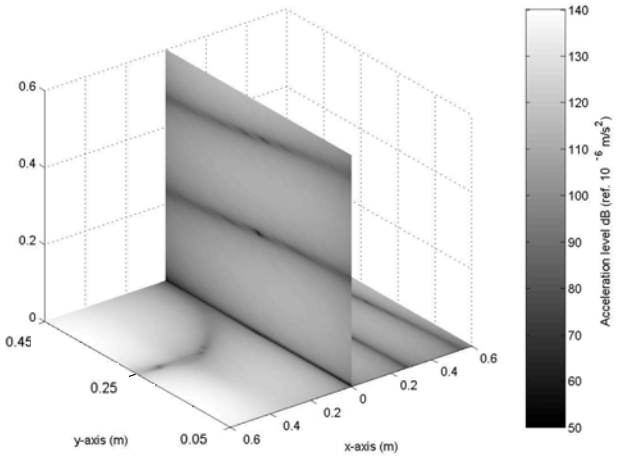

Figure 4.31. Contour plot of the controlled response at 90Hz for two dependently driven control forces at (x_{s1}, y_{s1})= (0.371, 0.31), (x_{s2}, y_{s2})= (0.371, 0.25) and two error sensors located on plate 2 at (x_{e1}, y_{e1}) = (0.23, 0.25) and (x_{e2}, y_{e2}) = (0.28, 0.25).

Figure 4.32 displays the contour plot of the controlled response for the same control arrangement as Figure 4.31, but with the control forces driven independently. Global attenuation was also achieved. The independently driven control forces achieved slightly better overall attenuation levels than the dependently driven control forces. When the control forces and error sensors are arbitrarily located, the attenuation levels using two independently driven control forces are significantly greater than those achieved using dependently driven control forces.

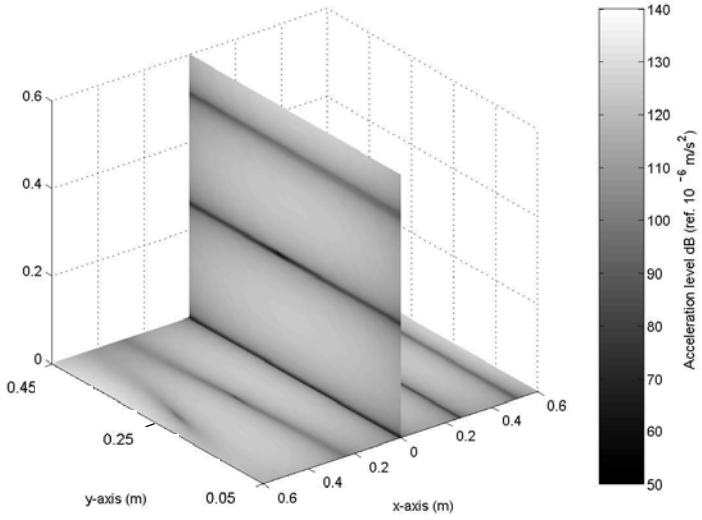

Figure 4.32. Contour plot of the controlled response at 90Hz for two independently driven control forces at (x_{s1}, y_{s1})= (0.371, 0.31), (x_{s2}, y_{s2})= (0.371, 0.25) and two error sensors located on plate 2 at (x_{e1}, y_{e1}) = (0.23, 0.25) and (x_{e2}, y_{e2}) = (0.28, 0.25).

Active control experiments were conducted to confirm the analytical results. The contour plot at a low resonance frequency of 53.13Hz was experimentally obtained (Figure 4.33). This is the second natural frequency of the T-shaped plate, and corresponds to mode (2,1) of each plate.

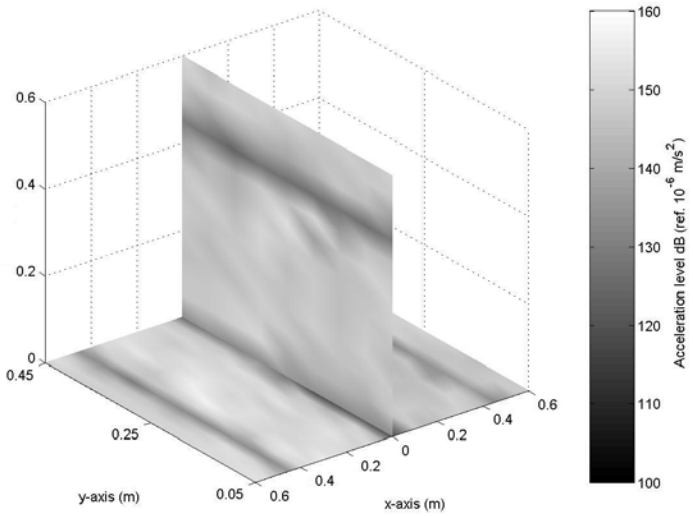

Figure 4.33. Experimental contour plot of the uncontrolled response at 53.13Hz.

The same control arrangements were used in the experiments as the control force and error sensor combinations used in the analytical investigation. Figures 4.34 and 4.35 show the controlled responses obtained experimentally at the resonance frequency of 53.13Hz, for a fixed control force location, and an optimally and arbitrarily located error sensor. Figure 4.34 shows that significantly greater attenuation levels are achieved, around 15dB globally, under the symmetrical control arrangement with respect to the simply supported boundary conditions. This symmetrical control arrangement corresponds to the primary and control forces positioned at the same $x-$location in plate 1 and in a symmetrical arrangement in the $y-$direction (between the simply supported

parallel edges). The error sensor is located in the far-field of the forces, but midway between the forces which corresponds to the midway point along the width of the plate ($y_e = L_y / 2$). The arbitrary error sensor location of (0.43, 0.375) is close to the nodal line on plate 2, and the contour plot of the controlled response shows an increase in the overall vibration levels of the plate (Figure 4.35).

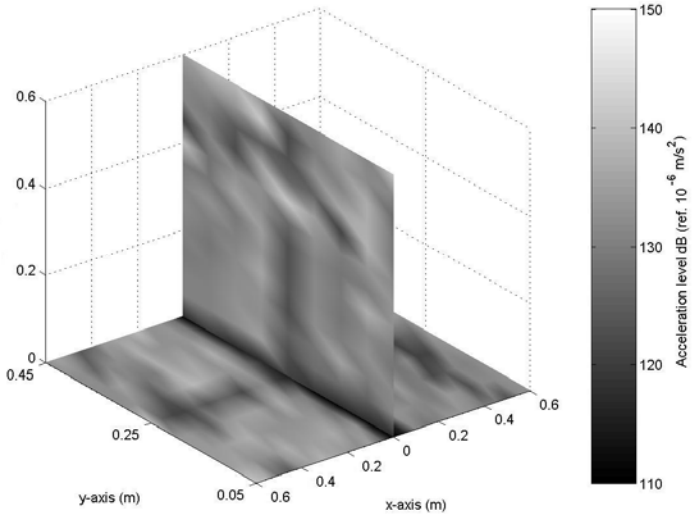

Figure 4.34. Experimental contour plot of the controlled response at 53.13Hz using a single control force at (x_{s1}, y_{s1}) = (0.371, 0.31) and an error sensor located on plate 2 at (x_{e1}, y_{e1}) = (0.23, 0.25).

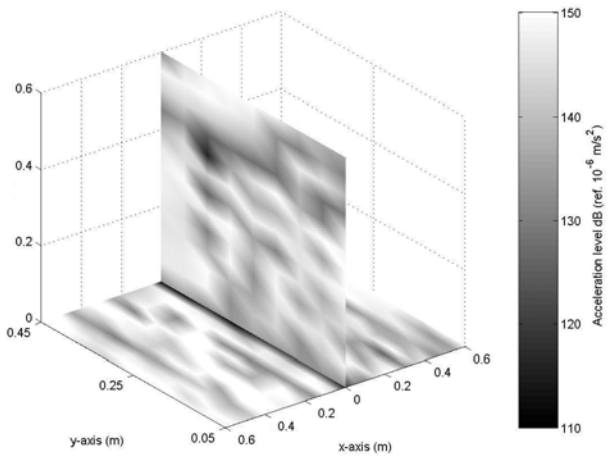

Figure 4.35. Contour plot of the controlled response at 53.13Hz for one control force at (x_{s1}, y_{s1}) = (0.371, 0.31) and an error sensor located on plate 2 at (x_{e1}, y_{e1}) = (0.43, 0.375).

Figures 4.36 and 4.37 show the contour plot of the controlled response obtained experimentally at 53.13Hz, for two dependently driven control forces at (x_{s1}, y_{s1})= (0.371, 0.25), (x_{s2}, y_{s2})= (0.371, 0.31), and two error sensors positioned on plate 2 at (x_{e1}, y_{e1}) = (0.23, 0.19), (x_{e2}, y_{e2}) = (0.23, 0.31) (Figure 4.36) and (x_{e1}, y_{e1}) = (0.23, 0.25), (x_{e2}, y_{e2}) = (0.28, 0.25) (Figure 4.37). Global attenuation of the T-shaped plate is achieved in both cases, although better attenuation is achieved when the error sensors are located along the anti-nodal line, corresponding to the midway point along the width of the plate for this resonance frequency (Figure 4.37). Figure 4.38 shows the contour plot of the controlled response for the same control arrangement as Figure 4.37, but with the control forces driven independently. Significantly better overall attenuation levels are achieved using independently driven control forces than the dependently driven control forces.

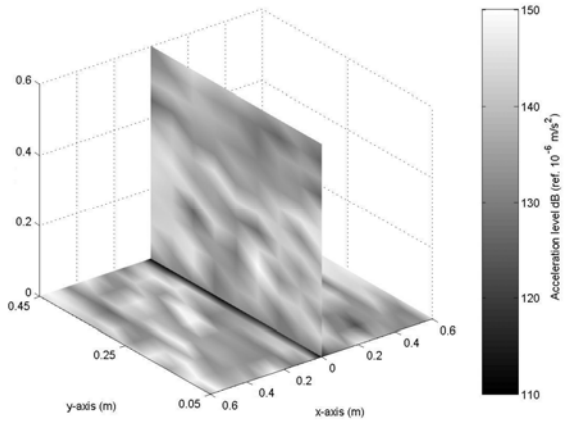

Figure 4.36. Contour plot of the controlled response at 53.13Hz for two dependently driven control forces at (x_{s1}, y_{s1}) = (0.371, 0.25), (x_{s2}, y_{s2}) = (0.371, 0.31) and two error sensors located on plate 2 at (x_{e1}, y_{e1}) = (0.23, 0.19) and (x_{e2}, y_{e2}) = (0.23, 0.31).

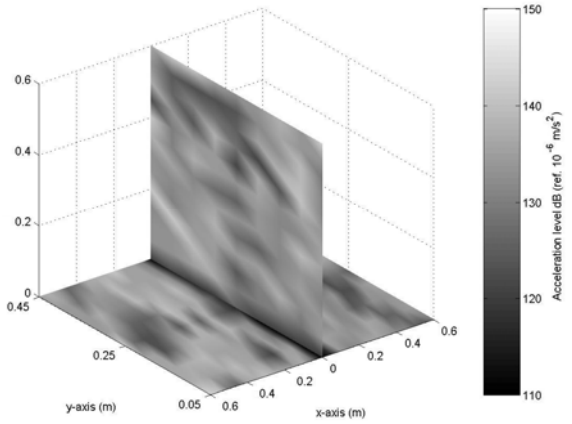

Figure 4.37. Contour plot of the controlled response at 53.13Hz for two dependently driven control forces at (x_{s1}, y_{s1}) =(0.371, 0.25), (x_{s2}, y_{s2}) = (0.371, 0.31) and two error sensors located on plate 2 at (x_{e1}, y_{e1}) = (0.23, 0.25) and (x_{e2}, y_{e2}) = (0.28, 0.25).

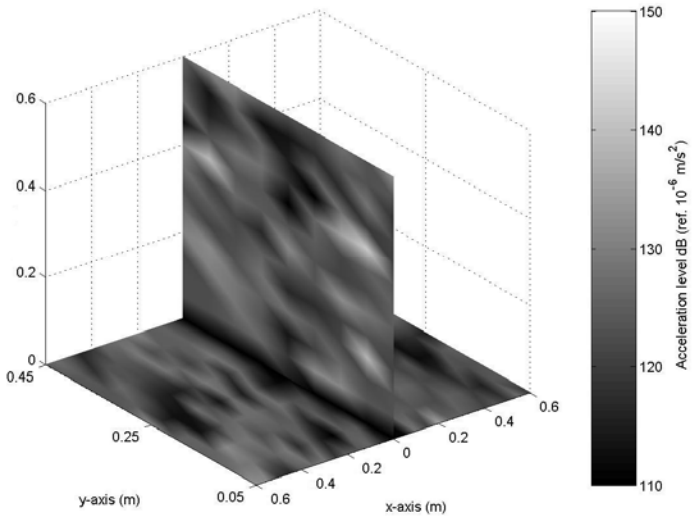

Figure 4.38. Contour plot of the controlled response at 53.13Hz for two independently driven control forces at (x_{s1}, y_{s1}) = (0.371, 0.25), (x_{s2}, y_{s2}) = (0.371, 0.31) and two error sensors located on plate 2 at (x_{e1}, y_{e1}) = (0.23, 0.25) and (x_{e2}, y_{e2}) = (0.28, 0.25).

4.4 X-Shaped Plate Results

In this section, only analytical results are presented for the X-shaped plate, and very similar control trends to the L and T-shaped plates were obtained for the X-shaped plate.

The effect of the error sensor numbers and locations was initially investigated using a single control force and a different number of error sensors. Figure 4.39 presents the primary and controlled acceleration distributions for a frequency range up to 400Hz for the X-shaped plate. The control force was located on plate 1 at the same $x-$location as the primary force at (x_{s1}, y_{s1}) = (0.371, 0.31). The use of a single error sensor located on

plate 2 at (x_{e1}, y_{e1}) = (0.23, 0.25) was compared with using two error sensors located on plate 2 at (x_{e1}, y_{e1}) = (0.36, 0.4) and (x_{e2}, y_{e2}) = (0.23, 0.25). Under the symmetrical control application using the single control force and error sensor, the control performance becomes independent of frequency (dashed line). The control performance deteriorates when one control force and multiple error sensors are used.

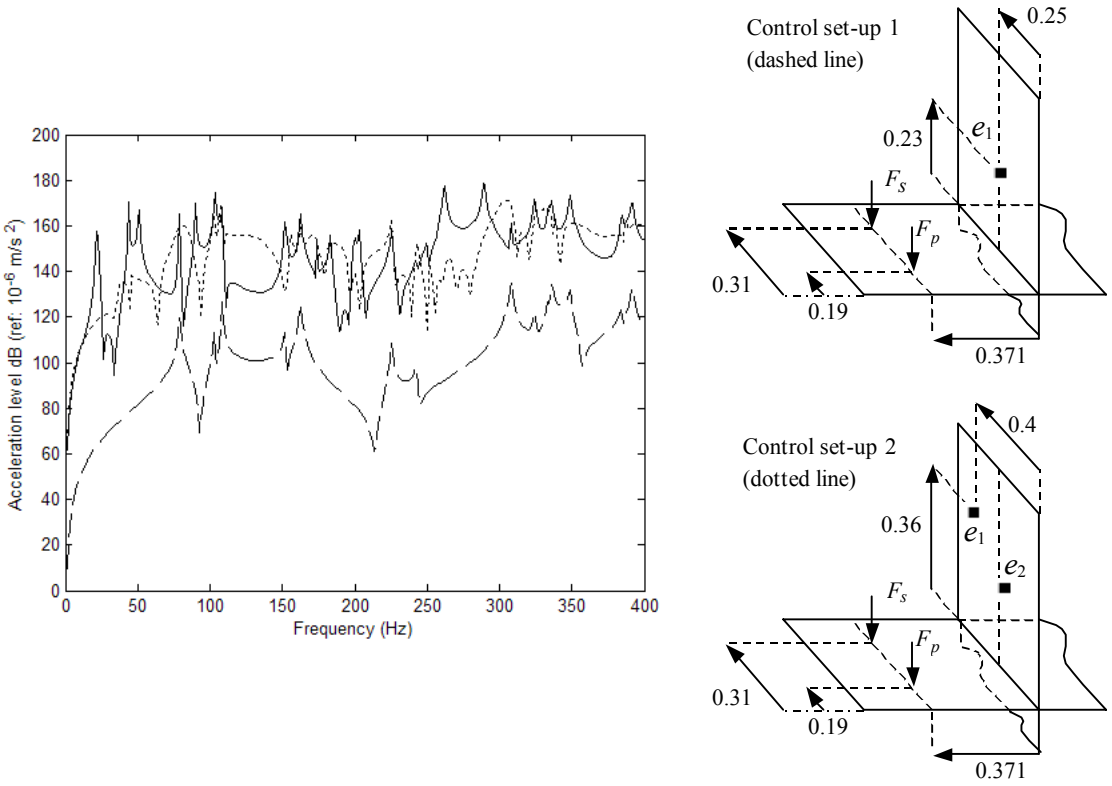

Figure 4.39. Primary (solid line) and controlled frequency responses for the X-shaped plate using primary and control forces located at (x_p, y_p) = (0.371, 0.19) and (x_{s1}, y_{s1}) = (0.371, 0.31) respectively, for an error sensor located on plate 2 at (x_{e1}, y_{e1}) = (0.23, 0.25) (dashed line), or two error sensors located on plate 2 at (x_{e1}, y_{e1}) = (0.36, 0.4) and (x_{e2}, y_{e2}) = (0.23, 0.25) (dotted line).

The effect of changing the locations of the control forces was also investigated for the X-shaped plate configuration. Two fixed error sensors located on plate 2 at (x_{e1}, y_{e1}) = (0.23, 0.19), (x_{e2}, y_{e2}) = (0.23, 0.31) were used. Figure 4.40 displays the primary and controlled acceleration distributions for a frequency range up to 400Hz for the X-shaped plate, using two dependently driven control forces located in line with the primary force at (x_{s1}, y_{s1}) = (0.371, 0.25), (x_{s2}, y_{s2}) = (0.371, 0.31) (dashed line), and two arbitrarily located forces at (x_{s1}, y_{s1}) = (0.15, 0.42), (x_{s2}, y_{s2}) = (0.35, 0.21) (dotted line). All forces were placed on plate 1. Figure 4.40 confirms that using two control forces and two error sensors, changing the control force locations has very little effect on the control performance.

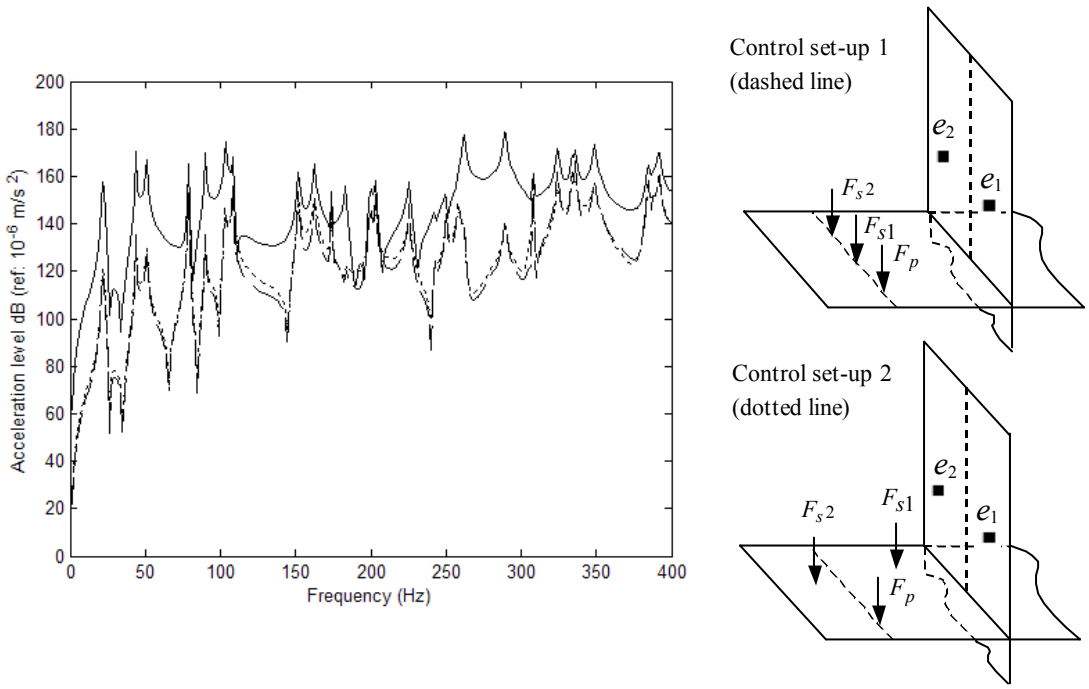

Figure 4.40. Primary (solid line) and controlled frequency responses for the X-shaped plate using two dependently driven control forces located on plate 1 at

(x_{s1}, y_{s1}) = (0.371, 0.25), (x_{s2}, y_{s2}) = (0.371, 0.31) (dashed line), and (x_{s1}, y_{s1}) = (0.15, 0.42), (x_{s2}, y_{s2}) = (0.35, 0.21) (dotted line).

Active control using a single control force and a single error sensor was also analytically investigated for two modes of vibration of the X-shaped plate. Figures 4.41 and 4.43 respectively show contour plots of the uncontrolled responses for two resonance frequencies corresponding to 151.99Hz and 203.45Hz. The 151.99Hz contour plot has a single nodal line running along the $x-$direction at the midway point in the $y-$direction. This corresponds to mode (3,2) of each plate. For the 203.45Hz contour plot, there are two nodal lines running along the $x-$direction, and corresponds to mode (2,3) of each plate. For the resonance frequency of 151.99Hz, the error sensor was located at an anti-nodal position on plate 3 at $(x_{e1}, y_{e1}) = (0.38, 0.125)$, and similarly, for 203.45Hz, the error sensor was positioned on an anti-nodal line on plate 4 at $(x_{e1}, y_{e1}) = (0.3, 0.25)$. The controlled responses for both frequencies are shown in Figures 4.42 and 4.44 respectively. Figure 4.42 shows that global attenuation levels in all four plates of around 35dB were achieved. Figure 4.44 also shows that global attenuation in all four plates is achieved, with attenuation levels of approximately 50dB obtained at the anti-nodal locations. Global attenuation of this magnitude was also reached when the single error sensor was placed at anti-nodal locations on the other plates making up the X-shaped structure. When the error sensor was moved away from the anti-nodal position, the control performance deteriorated.

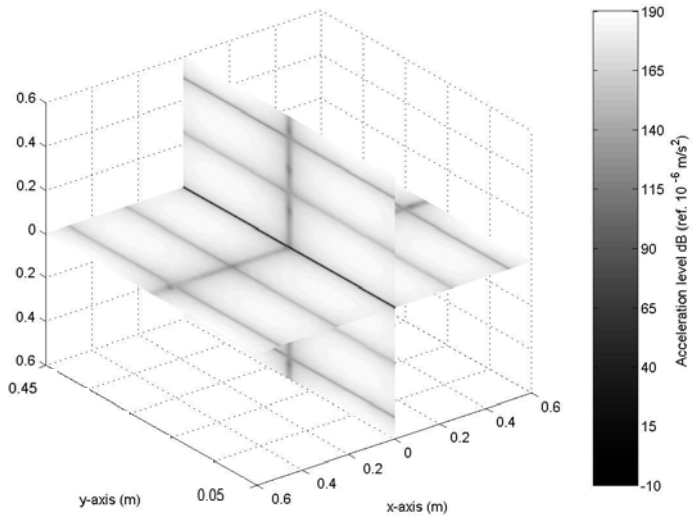

Figure 4.41. Contour plot of the uncontrolled response at 151.99Hz (analytical).

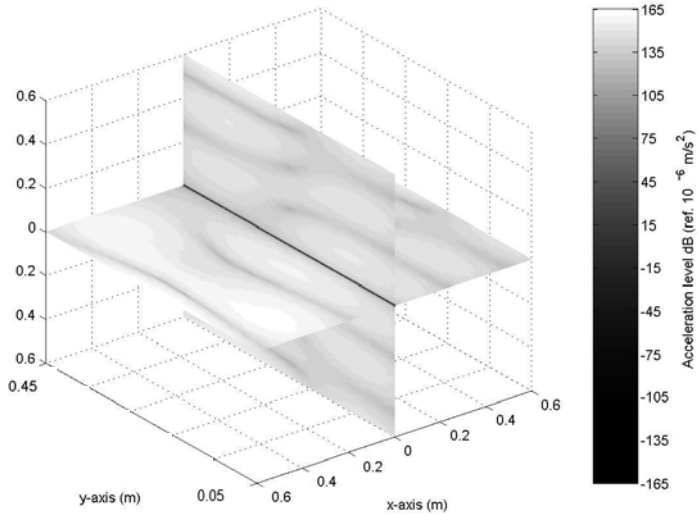

Figure 4.42. Contour plot of the controlled response at 151.99Hz for one control force at (x_{s1}, y_{s1}) = (0.371, 0.31) and an error sensor located on plate 3 at (x_{e1}, y_{e1}) = (0.38, 0.125).

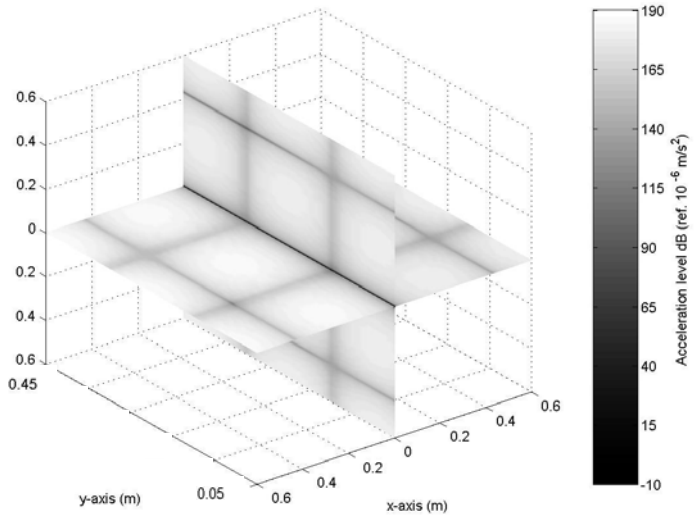

Figure 4.43. Contour plot of the uncontrolled response at 203.45Hz (analytical).

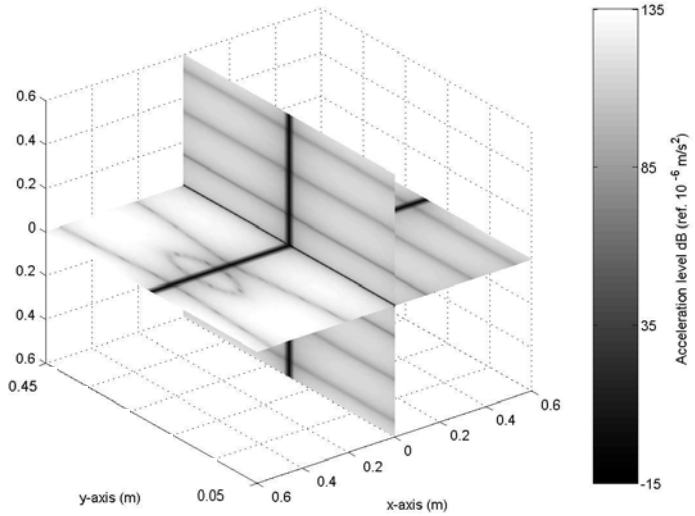

Figure 4.44. Contour plot of the controlled response at 203.45Hz for one control force at (x_{s1}, y_{s1}) = (0.371, 0.31) and an error sensor located on plate 4 at (x_{e1}, y_{e1}) = (0.3, 0.25).

4.5 Kinetic Energy

Another means of determining whether global attenuation of the structure has been achieved is to calculate the kinetic energies of the plates. The following tables show the total kinetic energy levels of the plates under various control applications obtained analytically and experimentally. In each case, the results of the global plate response at a single resonance frequency obtained analytically are compared to those of similar experimental modeshapes. From the results, it can be seen that global kinetic energy levels dropped in all control situations with the best attenuation achieved when independent control was implemented. This was the case for the L, T and X shaped plates both analytically and experimentally.

Table 4.1. Total kinetic energy levels of the uncontrolled and controlled responses for the L-shaped plate for an analytical resonance frequency of 202.95Hz and an experimental resonance frequency of 191.25Hz.

Number of control forces	Number of error sensors	Error sensor locations	Kinetic energy analytical	Kinetic energy experimental
Uncontrolled	-	-	6.53×10^{-3}	3.81×10^{-5}
1	1	(0.2,0.25)	4.55×10^{-5}	1.67×10^{-6}
2	2	(0.3,0.25)	7.32×10^{-4}	1.43×10^{-6}
(Dependent)		(0.4,0.25)		
2	2	(0.3,0.25)	9.41×10^{-5}	9.23×10^{-7}
(Independent)		(0.4,0.25)		

Table 4.2. Total kinetic energy levels of the uncontrolled and controlled responses for the T-shaped plate for an analytical resonance frequency of 90Hz and an experimental resonance frequency of 53.13Hz.

Number of control forces	Number of error sensors	Error sensor locations	Kinetic energy analytical	Kinetic energy experimental
Uncontrolled	-	-	6.02×10^{-2}	3.29×10^{-3}
1	1	(0.23,0.25)	8.37×10^{-4}	1.06×10^{-4}
1	1	(0.43,0.375)	8.25×10^{-3}	2.81×10^{-3}
2	2	(0.23,0.19)	2.31×10^{-3}	9.89×10^{-4}
(Dependent)		(0.23,0.31)		
2	2	(0.23,0.25)	5.12×10^{-4}	1.66×10^{-4}
(Dependent)		(0.28,0.25)		
2	2	(0.23,0.25)	2.98×10^{-4}	2.26×10^{-5}
(Independent)		(0.28,0.25)		

Table 4.3. Total kinetic energy levels of the uncontrolled and controlled responses for the X-shaped plate for an analytical resonance frequency of 151.99Hz.

Number of control forces	Number of error sensors	Error sensor locations	Kinetic energy analytical
Uncontrolled	-	-	1.82×10^{-1}
1	1	(0.38,0.125)	2.02×10^{-3}

Analytical and experimental results have shown that by using two control forces to minimise the vibration response at two error sensors, global attenuation of the primary frequency response can be achieved, as well as global attenuation of the plate structure at a discrete resonance frequency. At arbitrary force and sensor locations, higher attenuation levels were achieved using independently driven control forces compared to dependently driven control forces. The attenuation achieved for the L, T and X-shaped plates were also shown to be strongly dependent on both the error sensor location and resonance frequency. It can also be seen that global attenuation can be achieved using a single control force and a single error sensor if they are positioned symmetrically with respect to the primary force location.

CHAPTER 5

STATISTICAL ENERGY ANALYSIS

5.1 Introduction

Another method to predict the vibrational response and its transmission between coupled structures is Statistical Energy Analysis (SEA). SEA is generally used for high frequency noise and vibration problems, and provides a simple modelling procedure to estimate the vibrational response of complex structures using energy flow relationships. At medium to high frequencies, many hundreds of modes can be excited and it becomes extremely difficult to predict the detailed response of the structure using deterministic methods such as finite element modelling. In this chapter, energy levels of the coupled plates predicted from the exact analytical waveguide model are compared with those of conventional SEA models. A hybrid approach between the two techniques is presented. The hybrid method uses the analytical waveguide method to estimate the input power and coupling loss factors. The energy levels in a subsystem using the exact analytical method, SEA, and the hybrid technique are compared.

5.2 Basic SEA Theory

SEA predicts the average noise and vibration levels using the distribution and flow of vibrational energy through coupled subsystems. Figure 5.1 shows an example set of

coupled subsystems that make up an SEA system. The figure shows a mounted motor in a room that is sending vibrations through the building. The subsystems include the walls, floors and ceiling panels. The structural joints between the walls, floors and ceiling are the coupling points.

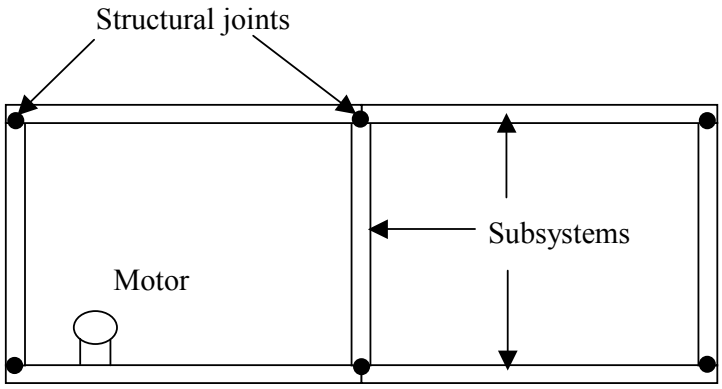

Figure 5.1. A SEA system showing its coupled subsystems.

The physical sub-systems are typically beams, plates, stiffeners, acoustic spaces, etc, which are coupled together to form a system. In SEA, it is also possible to describe a physical sub-system as two or more distinct dynamic sub-systems. For example, a plate in bending vibration, in-plane longitudinal vibration and in-plane shear motion forms three sub-systems.

The vibrational behaviour of a system is described in terms of power and energy. Within a subsystem, there may be three types of energy flows as shown in Figure 5.2 [41]. P_{in} is the input power to the subsystem, P_{dis} is the energy dissipated from the subsystem, and P_{ij} is

the energy flow from subsystem i to subsystem j through the couplings that join subsystems i and j. The energy and power terms are typically averaged over both space and frequency.

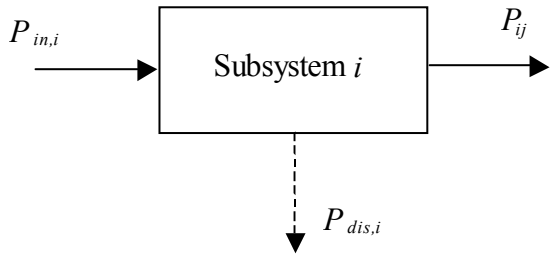

Figure 5.2. Energy flow through a subsystem.

From Figure 5.2, it can be seen that a basic power balance can be applied to the subsystem i:

$$P_{in,i} = P_{dis,i} + P_{ij} . \tag{5.1}$$

For each term shown in equation 5.1, the power P is given by [43]:

$$P = \omega \eta E \tag{5.2}$$

where ω is the radian frequency, η is the loss factor and E is the energy stored in the subsystem. There may be several different loss factors in an energy balance equation. The first one is the internal loss factor, η_i, which represents the energy lost by subsystem i due

to internal damping and radiation to the outside environment. The second is the coupling loss factor, η_{ij}, which determines the power transmitted from subsystem i to subsystem j. Using the internal and coupling loss factors, equation (5.1) can be written as [43]:

$$P_{in,i} = \omega\eta_i E_i + \omega\eta_{ij} E_i . \tag{5.3}$$

In SEA, it is assumed that the couplings between all subsystems are conservative. Therefore, any energy flowing out of one subsystem must flow into another. If two subsystems do not interact, the coupling loss factor is taken as equal to zero.

5.2.1 Modal density

In order to ensure that a sufficient number of modes of a structural element respond in the frequency range of interest, the modal density is examined. The modal density $n(\omega)$ is defined as the number of vibrational modes per unit frequency, and is an important parameter in SEA. For one and two-dimensional structures, the modal density can respectively be written as [41]:

$$n_{1-D} = \frac{l}{\pi c_g} \tag{5.4}$$

$$n_{2-D} = \frac{\omega S}{2\pi c_g c} \tag{5.5}$$

where l is the length of the one-dimensional component, S is the area of the two-dimensional component, c_g is the group velocity, and c is the phase velocity ($c = \omega / k$). For bending vibration in thin plates, the phase velocity is:

$$c_B = \frac{\omega}{k_B} = \sqrt{\omega}\left(\frac{D}{\rho h}\right)^{1/4}. \tag{5.6}$$

The group velocity is twice the phase velocity $c_g = 2c_B$. For a thin plate in bending vibration, equation (5.5) can be written as [41]:

$$n(\omega) = \frac{L_x L_y}{4\pi}\sqrt{\frac{\rho h}{D}}. \tag{5.7}$$

It can be seen in equation (5.7) that the modal density for bending vibration of thin plates becomes independent of frequency.

5.2.2 Internal loss factor

When materials are deformed, energy is absorbed and dissipated by the material. This is accounted for by using a structural loss factor (commonly known as an internal loss factor in SEA applications). As shown in the previous section, there are often analytical solutions available to calculate the modal density. This is not the case for the internal loss factor. The loss factors are usually obtained experimentally by separately measuring the energy dissipation in each of the uncoupled elements. The internal loss factor is dependent on

frequency, but can be assumed constant when examining frequency ranges between 1 kHz and 10 kHz [7]. Internal loss factors for some common materials are given in Table 6.1 of reference 42.

5.2.3 Coupling loss factor

The coupling loss factors relate to the transmission of vibrational energy between coupled subsystems in a built-up system. The coupling loss factor, η_{ij}, is the parameter used to determine the amount of "coupling" between two subsystems i and j. In SEA applications, it is desirable that the subsystems be weakly coupled, which occurs when the material loss factor is greater than the coupling loss factor, that is, $\eta_{ij} < \eta_i$ or $\eta_{ij} < \eta_j$ [64]. For weakly coupled subsystems, energy is lost due to dissipation, and the structural loss factor dominates [7]. For strongly coupled subsystems, energy is lost due to transmission, and hence the coupling loss factor dominates. Analytical expressions are available for coupling between structural elements such as line junctions between coupled plates and plate-cantilever beam junctions, as well as between structural and acoustic volumes [42]. The most widely used method to evaluate the coupling loss factors for systems connected along a line is to use the wave transmission approach [57]. Using the wave approach, the coupling loss factor η_{ij} is derived directly from the power transmission coefficient τ_{ij}, which is defined as the ratio of the transmitted to incident power at the boundary:

$$\tau_{ij} = \frac{\text{Transmitted power}}{\text{Incident power}} = \frac{P_{transmitted}}{P_{incident}}. \tag{5.8}$$

When calculating the power transmission coefficient using the wave transmission method, the subsystems are assumed to be semi-infinite [41]. Therefore, waves impinging on the junction of two coupled subsystems *i* and *j* are reflected (in subsystem *i*) and transmitted (to subsystem *j*), but no reflection at the other boundaries of the subsystems away from the junction is taken into account. Equations (5.9) to (5.14) are the power transmission coefficients for the L, T and X shaped plates for bending waves only [64]. In deriving these expressions, it has been assumed that the group velocities in each plate are the same. All plates are the same material and σ is the plate thickness ratio. For plates of the same thickness ($\sigma = 1$), the power transmission coefficients for the L, T and X-shaped plates are given by the number on the right hand side in equations (5.9) to (5.14).

L-shaped plate:

$$\tau_{12} = 2\left(\sigma^{-5/4} + \sigma^{5/4}\right)^{-2} = 0.5 \tag{5.9}$$

T-shaped plate:

$$\tau_{12} = \left(\sqrt{2}\sigma^{-5/4} + \frac{\sigma^{5/4}}{\sqrt{2}}\right)^{-2} = 0.222 \tag{5.10}$$

$$\tau_{13} = \left(2 + 2\sigma^{5/2} + 0.5\sigma^{5}\right)^{-1} = 0.222 \tag{5.11}$$

X-shaped plate:

$$\tau_{12} = 0.5\left(\sigma^{-5/4} + \sigma^{5/4}\right)^{-2} = 0.125 \tag{5.12}$$

$$\tau_{13} = 0.5\left(1 + 2\sigma^{5/2} + \sigma^{5}\right)^{-1} = 0.125 \tag{5.13}$$

$$\tau_{14} = 0.5\left(\sigma^{-5/4} + \sigma^{5/4}\right)^{-2} = 0.125 \tag{5.14}$$

The general expression used to determine the coupling loss factor for two structures joined along a line in terms of the power transmission coefficient is given by [7,41]:

$$\eta_{ij} = \frac{2c_B L\left\langle \tau_{ij} \right\rangle}{\pi\omega S_i} \tag{5.15}$$

where L is the length of the junction line, ω is the centre frequency of the band of interest, and S_i is the surface area of the subsystem i. The brackets $\langle\ \rangle$ represent averaged over position, as the power transmission coefficient is averaged at all angles of incidence to the junction.

The coupling loss factors satisfy the reciprocity relation of $n_i\eta_{ij} = n_j\eta_{ji}$ where n_i is the modal density of subsystem i. It was shown in equation (5.7) that the modal density for a thin plate in bending vibration is independent of the frequency, and is proportional to the

surface area S of the plate. Hence, for two coupled plates of the same material parameters, the reciprocity relation can be written as $S_i \eta_{ij} = S_j \eta_{ji}$ [43], where S_i and S_j are the surface areas of plates i and j respectively.

5.2.4 Input power

The input power is an important parameter in SEA calculations. If a point force F drives a system, then the total power supplied to the system is given by [42]:

$$P_{in} = \frac{F^2}{2} \mathrm{Re}\left(\frac{1}{Z}\right) \tag{5.16}$$

where Z represents the impedance of an infinite plate. When the power transmission into a plate (in bending vibration) is frequency averaged, it becomes independent of size, shape and boundary conditions, and proportional to the real part of the mobility of an infinite plate [7]. The mobility is equal to the inverse of the impedance. For a thin isotropic plate, the impedance Z is given by [7]:

$$Z = 8\sqrt{D\rho}\,. \tag{5.17}$$

5.3 SEA Modelling of the Coupled Plates

In an SEA model of an L-shaped plate, consisting of two finite plates joined together at right angles along a common edge as shown in Figure 2.1, the plate can be separated into two physical systems corresponding to plate 1 and plate 2. The input power is injected into plate 1 only. The coupling of the SEA subsystems for bending vibration only is shown in Figure 5.3. The power balance equations for the system in bending vibration only are given in matrix form in equation (5.18).

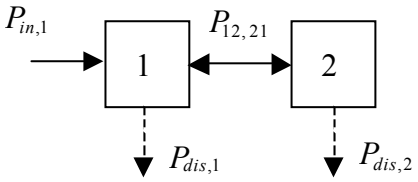

Figure 5.3. SEA power flow for the L-shaped plate in bending vibration only.

$$\begin{Bmatrix} P_{in,1} \\ 0 \end{Bmatrix} = \omega \begin{bmatrix} \eta_1 + \eta_{12} & -\eta_{21} \\ -\eta_{12} & \eta_2 + \eta_{21} \end{bmatrix} \begin{Bmatrix} E_1 \\ E_2 \end{Bmatrix} \tag{5.18}$$

The energies in each plate, E_1 and E_2 can then be determined by:

$$\begin{Bmatrix} E_1 \\ E_2 \end{Bmatrix} = \frac{1}{\omega} \begin{bmatrix} \eta_1 + \eta_{12} & -\eta_{21} \\ -\eta_{12} & \eta_2 + \eta_{21} \end{bmatrix}^{-1} \begin{Bmatrix} P_{in,1} \\ 0 \end{Bmatrix} \tag{5.19}$$

For coupling between multiple subsystems as in the case of the T and X-shaped plates, the SEA power flow equation becomes [42,65]:

$$P_{in,i} = \omega\eta_i E_i + \sum_j \omega\left(\eta_{ij} E_i - \eta_{ji} E_j\right) \tag{5.20}$$

Using the reciprocity relation, Equation (5.20) can be written as:

$$P_{in,i} = \omega\eta_i E_i + \sum_j \omega\eta_{ij} S_i \left(\frac{E_i}{S_i} - \frac{E_j}{S_j}\right) \tag{5.21}$$

In addition to examining SEA in L, T and X-shaped plates, a built up structure consisting of seven plates joined at right angles as shown in Figure (5.4) is examined. The built up structure models a section of a ship hull, and the seven plates are connected to form an L-shaped plate (plates 1 and 2), a X-shaped plate (plates 2 to 5) and a T-shaped plate (plates 5, 6 and 7). Using equation (5.21), the power balance equations for the system can be obtained, where power is injected into subsystem 1 (plate 1) only.

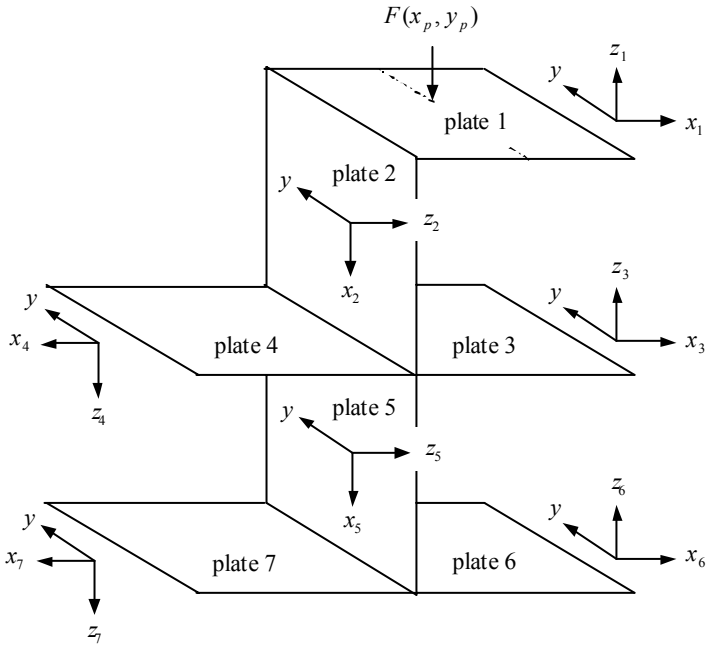

Figure 5.4. The built up structure consisting of seven plates joined together to form L, T and X-shaped configurations.

5.4 Hybrid Approach between the Waveguide Method and SEA

The hybrid approach involves using the analytical waveguide model introduced in Chapter 2 to estimate the input power and coupling loss factors used in the SEA equations. A simple well-known structure corresponding to an L-shaped plate was initially investigated to validate the traditional SEA results. The hybrid method was then used to analyse the T and X-shaped plate structures, and finally the seven-plate structure shown in Figure 5.4.

The input bending power for the SEA model was calculated by averaging the response over all possible excitation locations in the $x-$ and $y-$directions. The time-averaged flexural input power at a given $x-$ location is given by [66]:

$$\langle P_{in} \rangle = -\frac{1}{2}\mathrm{Re}\left[(j\omega w)^{*} F_x - \left(j\omega \frac{\partial w}{\partial x} \right)^{*} M_x - \left(j\omega \frac{\partial w}{\partial y} \right)^{*} M_{xy} \right] \tag{5.22}$$

where the asterisk * denotes the complex conjugate, and the brackets $\langle\ \rangle$ represents average over position. F_x, M_x and M_{xy} are the bending shear force, bending moment and twisting moment respectively. M_x is given by equation (2.5) whilst F_x and M_{xy} are respectively given by:

$$F_x = -D\left(\frac{\partial^3 w}{\partial x^3} + \frac{\partial^3 w}{\partial x \partial y^2} \right) \tag{5.23}$$

$$M_{xy} = -D(1-\nu)\frac{\partial^2 w}{\partial x \partial y}. \tag{5.24}$$

Note that the net vertical shear force given by equation (2.4) is obtained by $Q_x = F_x + \partial M_{xy}/\partial y$. The simply supported boundary conditions allowed the bending power to be averaged in the $y-$direction by integrating the power equation over the width of the plate from 0 to L_y. This results in a factor of 1/2 and removes the dependency of the input power on the $y-$location of the applied force. The input power was then averaged

across the plate in the $x-$direction by driving the structure at a range of $x-$locations and then averaging the response.

The coupling loss factor η_{ij} was determined directly from the power transmission coefficient $\langle \tau_{ij} \rangle$ and using the assumption of infinite plates. The assumption of the infinite boundary conditions was implemented by assuming no reflection from the free plate edges at $x_i = L_{xi}$. In the L-shaped plate, the incident bending power was then found using the following expression for the propagating flexural displacement (in the negative x_1 direction) impinging at the coupling junction ($x_i = 0$):

$$w_1(x_1, y) = \sum_{m=1}^{\infty} B_1 \sin k_y y \tag{5.25}$$

Similarly, the transmitted bending power in plate 2 was found using the following expression for the transmitted propagating flexural waves at the coupling junction ($x_i = 0$):

$$w_2(x_2, y) = \sum_{m=1}^{\infty} A_2 \sin k_y y \ . \tag{5.26}$$

B_1 and A_2 are coefficients of propagating waves in plates 1 and 2 respectively, and have been previously determined in Chapter 2.

The power transmission coefficient was calculated by the ratio of the transmitted bending power to the incident bending power at the junction of the two plates found using equation (5.22). The coupling loss factors were then calculated using equation (5.15). Once the input power and coupling loss factors were found using the analytical waveguide model, the energy levels of each plate were determined.

5.5 Hybrid Results

The energy levels of each plate found using the hybrid approach are compared with those obtained from the analytical waveguide method as well as using the conventional SEA equations. The hybrid results are averaged over every 100Hz frequency band, and the value presented at the centre frequency of each 100Hz band. Three frequency ranges were examined corresponding to up to 1 kHz (low frequency range), 5 to 6 kHz (medium frequency range), and 10 to 11 kHz (high frequency range). A sufficient number of modes were used in the computational modelling to accurately describe the response in the various frequency ranges of interest. This was achieved by ensuring that a sufficient number of modes was chosen in each frequency range such that all the results converged. The power transmission coefficients calculated from the hybrid method are also presented and compared with those given in equations (5.9) to (5.14) from reference 64. The results presented are for bending motion only in the coupled plates, although it could be expected that as the frequency increases, in-plane vibration will begin to have a significant role [67,68]. The same material parameters and plate dimensions given in Chapter 4 were used in the calculations.

5.5.1 L-shaped plate results

Figure 5.5 and 5.6 display the energy levels of plate 1 and plate 2 of the L-shaped structure respectively. The energy levels were found using the hybrid approach, the waveguide analytical method and SEA techniques for a frequency up to 1 kHz. The results indicate that the conventional SEA equations give a poor indication of the mean energy levels at low frequencies, and tends to over predict the energy levels by around 5 to 10 dB. It can be seen that the hybrid approach gives more accurate results over the entire frequency range. Comparing Figures 5.5 and 5.6, there is a slight reduction of energy levels between plate 1 and plate 2 due to the energy lost through transmission at the structural joint.

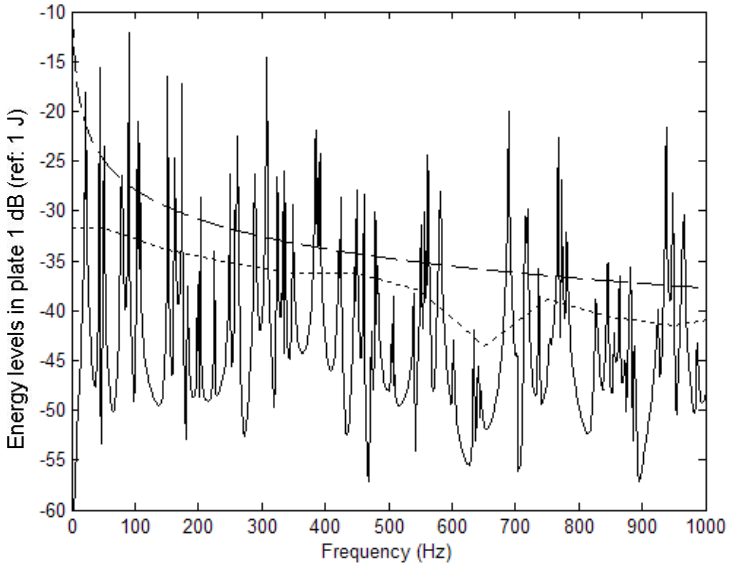

Figure 5.5. Energy levels in plate 1 of the L-shaped plate using the analytical waveguide method (solid line), SEA (dashed line), and the hybrid approach (dotted line), for a frequency range from 1 Hz to 1 kHz.

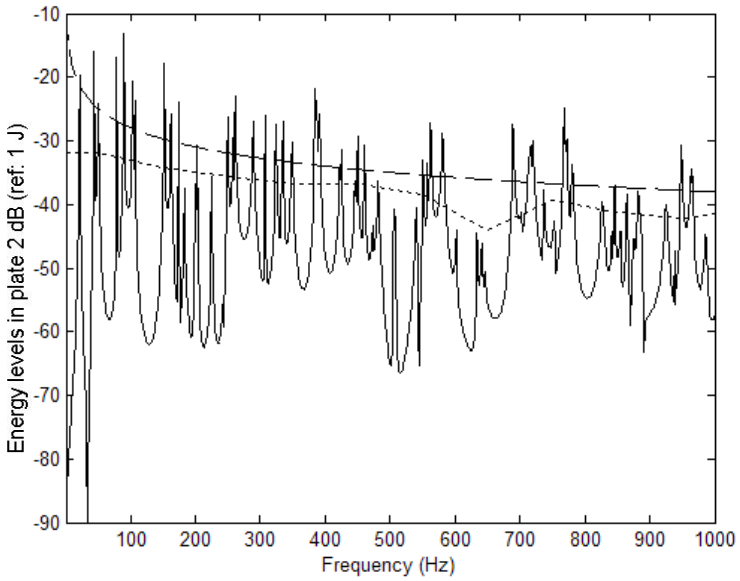

Figure 5.6. Energy levels in plate 2 of the L-shaped plate using the analytical waveguide method (solid line), SEA (dashed line), and the hybrid approach (dotted line), for a frequency range from 1 Hz to 1 kHz.

The energy levels of plates 1 and 2 of the L-shaped plate calculated for a frequency range from 5 to 6 kHz are presented in Figures 5.7 and 5.8 respectively. The results again show that in this mid-frequency band, SEA over predicts the mean energy levels in both plates The figures also show that the energy levels using conventional SEA becomes nearly a straight line (constant with frequency) due to a greater population of modes in this frequency range. The reduction in energy levels from plate 1 to plate 2 increases as the frequency increases.

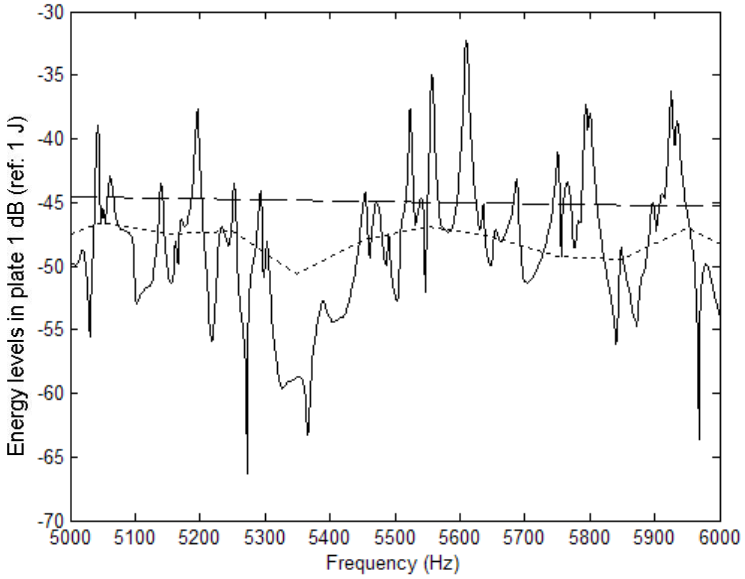

Figure 5.7. Energy levels in plate 1 of the L-shaped plate using the analytical waveguide method (solid line), SEA (dashed line), and the hybrid approach (dotted line), for a frequency range from 5 to 6 kHz.

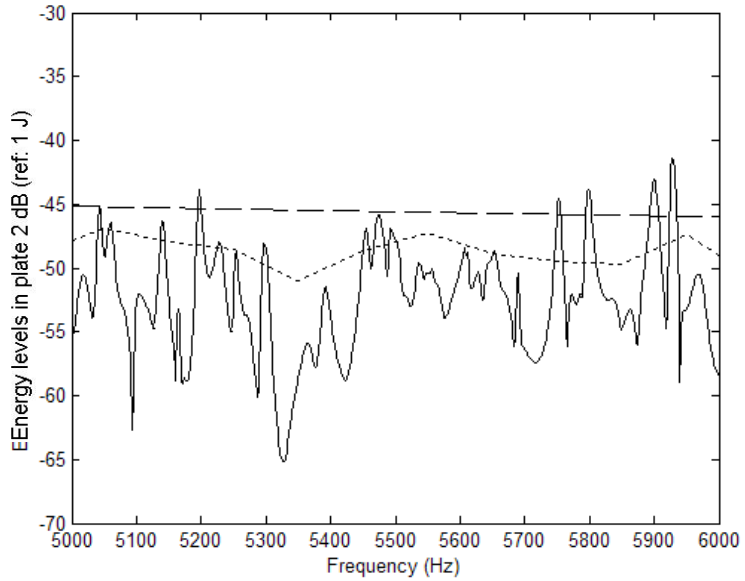

Figure 5.8. Energy levels in plate 2 of the L-shaped plate using the analytical waveguide method (solid line), SEA (dashed line), and the hybrid approach (dotted line), for a frequency range from 5 to 6 kHz.

Figures 5.9 and 5.10 show the energy levels of plate 1 and plate 2 respectively of the L-shaped plate, for a frequency range between 10 and 11 kHz. As the frequency increases, it appears that the over prediction of the mean energy levels using the conventional SEA equations also increases. The hybrid approach produces slightly better results. Previous work has shown that neglecting the in-plane modes of vibration, the energy levels can be significantly underestimated at higher frequencies [67,68]. If in-plane vibration was accounted for, the overall energy levels of the plates would increase at the higher frequencies. Therefore the SEA and the hybrid model could be expected to give more accurate results at these higher frequencies if the in-plane motion is included. Figures 5.9 and 5.10 also show that there are no distinct resonance peaks due to the significant modal overlap in the high frequency range. In addition, there is significant decrease in the variance of the amplitude of the frequency response function at high frequencies. That is, the energy levels fluctuate by around 10 dB compared with around 25 to 30 dB in the low frequency range.

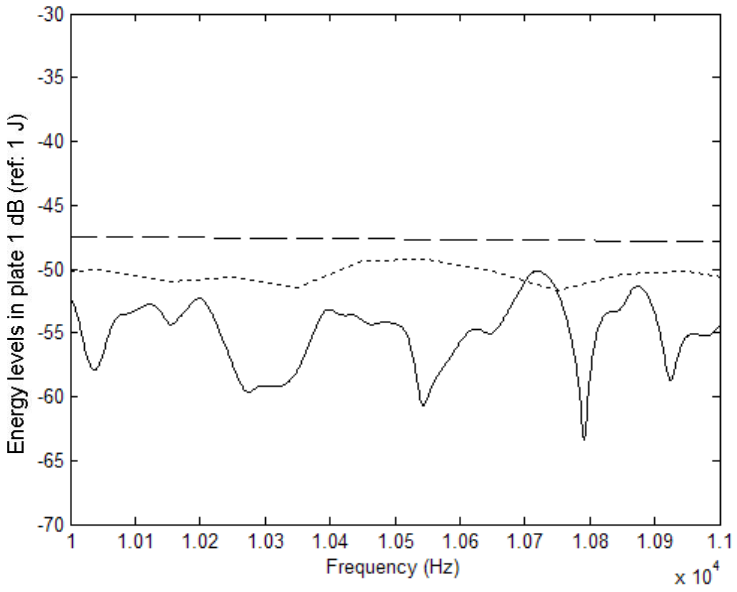

Figure 5.9. Energy levels in plate 1 of the L-shaped plate using the analytical waveguide method (solid line), SEA (dashed line), and the hybrid approach (dotted line), for a frequency range from 10 to 11 kHz.

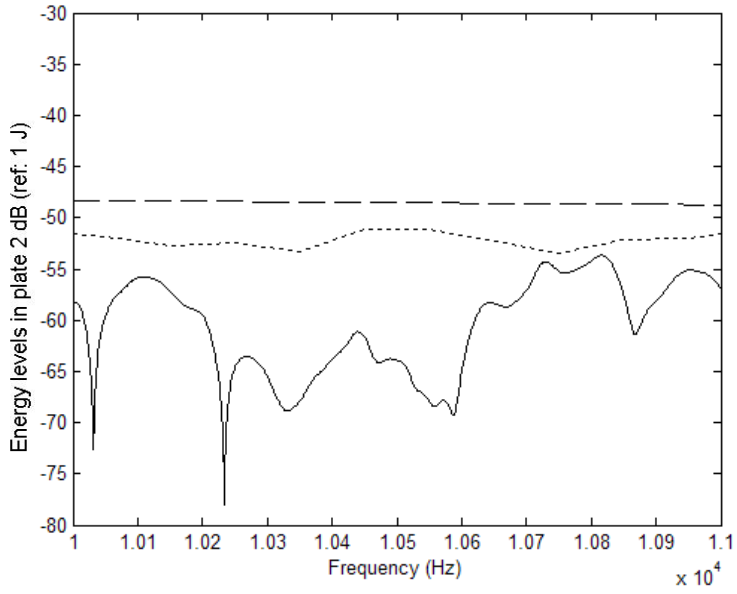

Figure 5.10. Energy levels in plate 2 of the L-shaped plate using the analytical waveguide method (solid line), SEA (dashed line), and the hybrid approach (dotted line), for a frequency range from 10 to 11 kHz.

Figures 5.11 to 5.13 show a comparison of the power transmission coefficients $\langle \tau_{12} \rangle$, calculated using the hybrid approach for the three frequency ranges with those predicted using equation (5.9). For an L-shaped structure, where the group velocities in each plate are the same, both plates are the same material, and the plate thickness ratio is unity, the transmission coefficient predicted by equation (5.9) is 0.5 and is a constant. In each case, it can be seen that the power transmission coefficient predicted using the hybrid method is slightly higher than the value presented in equation (5.9), although both values for τ_{12} are in very good agreement for all frequencies over the three frequency ranges.

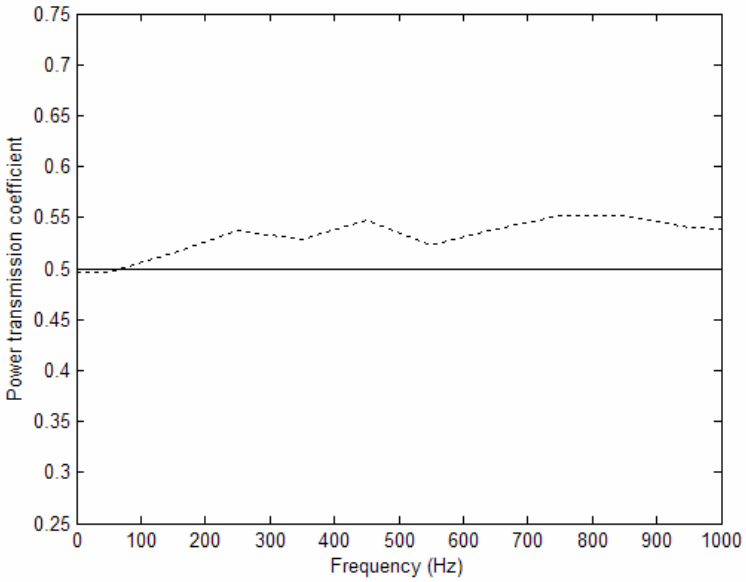

Figure 5.11. The power transmission coefficients $\langle \tau_{12} \rangle$ found using the hybrid approach (dotted line), and predicted from equation (5.9) resulting in $\tau_{12} = 0.5$ (solid line), for a frequency range from 1 Hz to 1 kHz.

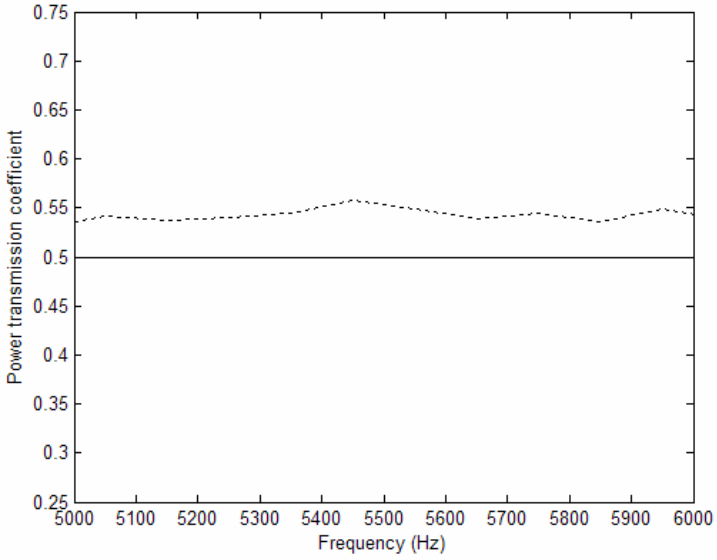

Figure 5.12. The power transmission coefficients $\langle \tau_{12} \rangle$ found using the hybrid approach (dotted line), and predicted from equation (5.9) resulting in $\tau_{12} = 0.5$ (solid line), for a frequency range from 5 kHz to 6 kHz.

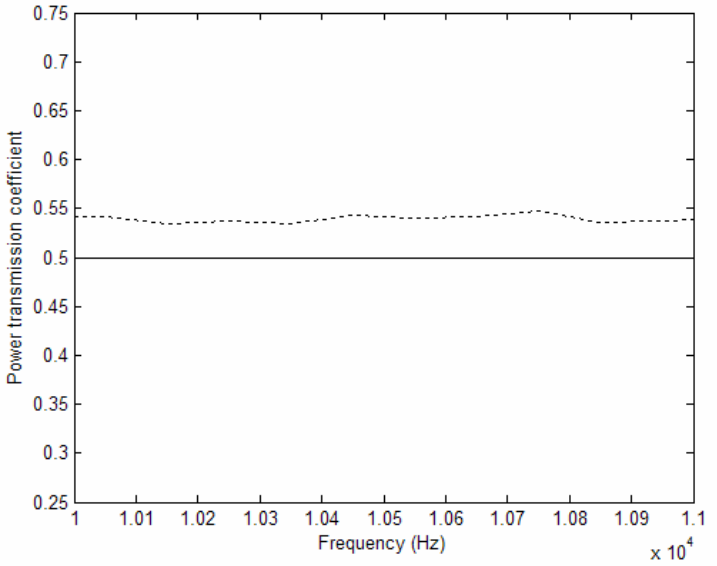

Figure 5.13. The power transmission coefficients $\langle \tau_{12} \rangle$ found using the hybrid approach (dotted line), and predicted from equation (5.9) resulting in $\tau_{12} = 0.5$ (solid line), for a frequency range from 10 kHz to 11 kHz.

5.5.2 T-shaped plate results

Figures 5.14 and 5.15 show the energy levels of plate 1 and plate 2 of the T-shaped structure respectively for frequencies up to 1 kHz. As shown with the L-shaped plate, the hybrid approach gives more accurate results over the entire frequency range. The energy levels predicted in each plate using the conventional SEA equations overestimates the mean energy levels in the plates.

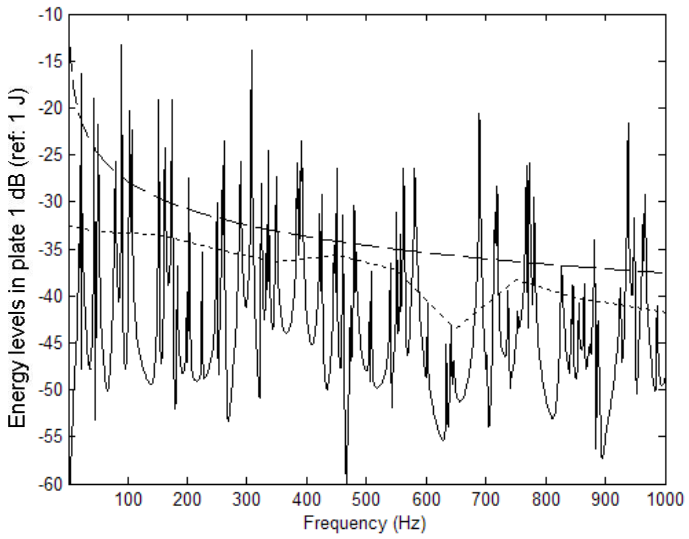

Figure 5.14. Energy levels in plate 1 of the T-shaped using the analytical waveguide method (solid line), SEA (dashed line), and the hybrid approach (dotted line), for a frequency range from 1 Hz to 1 kHz.

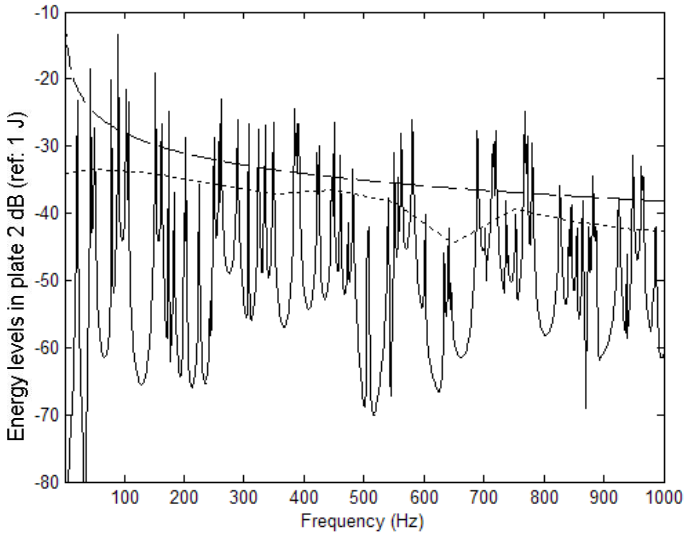

Figure 5.15. Energy levels in plate 2 of the T-shaped using the analytical waveguide method (solid line), SEA (dashed line), and the hybrid approach (dotted line), for a frequency range from 1 Hz to 1 kHz.

The energy levels of plates 1 and 2 of the T-shaped structure for a frequency range from 10 to 11 kHz are presented in Figures 5.16 and 5.17 respectively. The results show that in this high-frequency band, SEA significantly over predicts the energy levels in both plates by as much as 10 dB compared to the exact analytical waveguide method. Whilst the hybrid approach also over predicts the energy levels, slightly better results than using the conventional SEA equations are obtained. There are no distinct resonance peaks due to the significant modal overlap in the high frequency range, and there is a dramatic decrease in the variance of the energy levels obtained using the analytical waveguide method as the frequency increases.

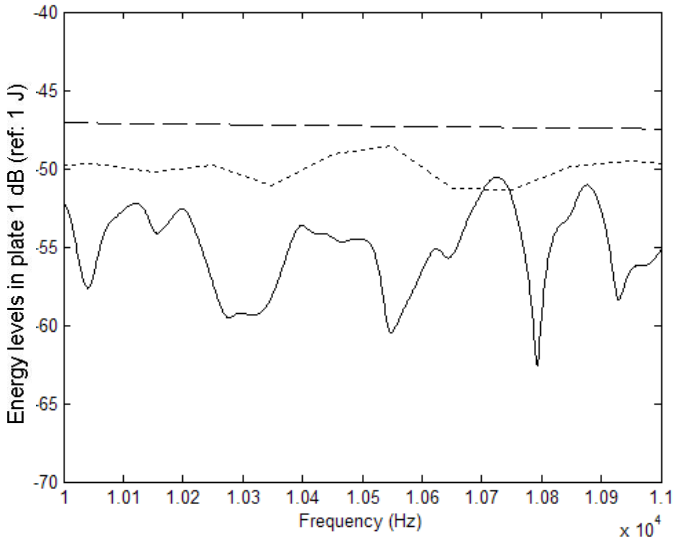

Figure 5.16. Energy levels in plate 1 of the T-shaped using the analytical waveguide method (solid line), SEA (dashed line), and the hybrid approach (dotted line), for a frequency range from 10 kHz to11 kHz.

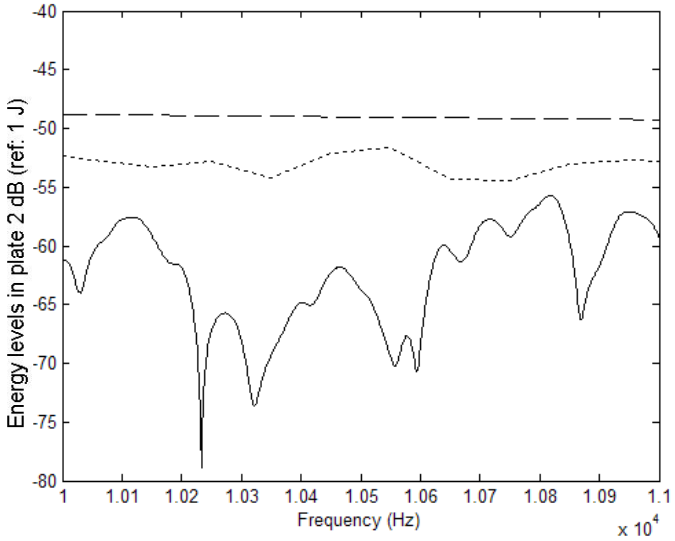

Figure 5.17. Energy levels in plate 2 of the T-shaped using the analytical waveguide method (solid line), SEA (dashed line), and the hybrid approach (dotted line), for a frequency range from 10 kHz to 11 kHz

Figures 5.18 and 5.19 present the power transmission coefficients calculated using the hybrid approach and predicted using equation (5.10), where $\tau_{12} = 0.222$ and is a constant. The frequency ranges are from 1 Hz to 1 kHz, and 10 to 11 kHz respectively. Similar to the L-shaped plate, the power transmission coefficient predicted using the hybrid method is slightly higher than that found using equation (5.10), although both values are in very good agreement.

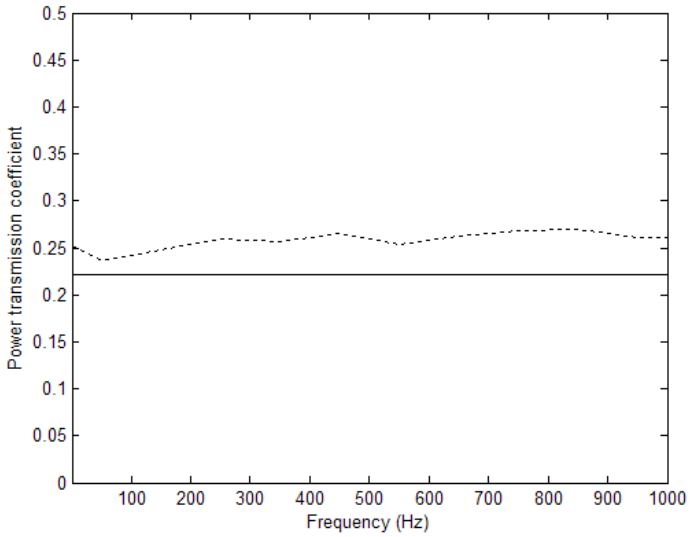

Figure 5.18. The power transmission coefficients $\langle \tau_{12} \rangle$ found using the hybrid approach (dotted line), and predicted from equation (5.10) resulting in $\tau_{12} = 0.222$ (solid line), for a frequency range from 1 Hz to 1 kHz.

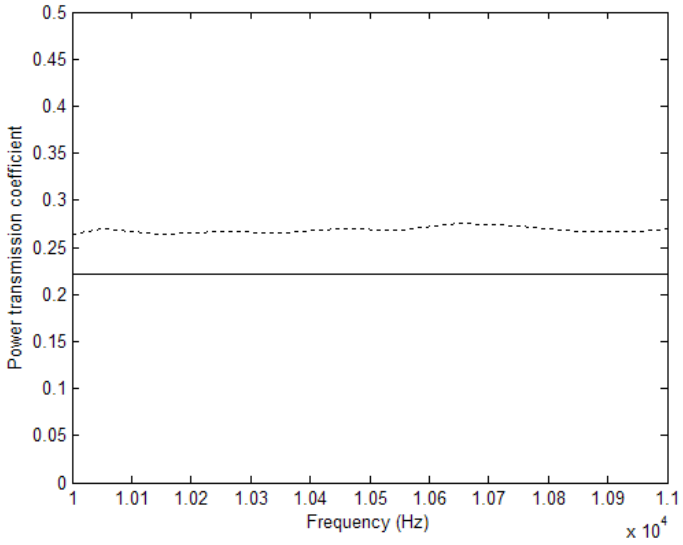

Figure 5.19. The power transmission coefficients $\langle \tau_{12} \rangle$ found using the hybrid approach (dotted line), and predicted from equation (5.10) resulting in $\tau_{12} = 0.222$ (solid line), for a frequency range from 10 kHz to 11 kHz.

5.5.3 X-shaped plate results

Figure 5.20 shows the energy levels of plate 3 of the X-shaped structure, for frequencies up to 1 kHz. The conventional SEA equations overestimate the mean energy levels in the plate while the hybrid method produces slightly better results over the entire frequency range. Figure 5.21 presents the power transmission coefficients calculated using the hybrid approach and equation (5.13), where $\tau_{12} = 0.125$ and is a contant. The power transmission coefficient predicted using the hybrid method is slightly higher than that found using equation (5.13).

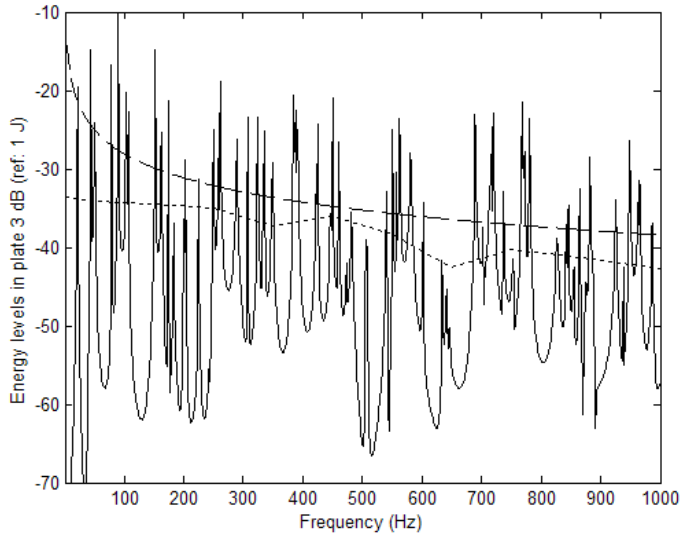

Figure 5.20. Energy levels in plate 3 of the X-shaped using the analytical waveguide method (solid line), SEA (dashed line), and the hybrid approach (dotted line), for a frequency range from 1 Hz to 1 kHz.

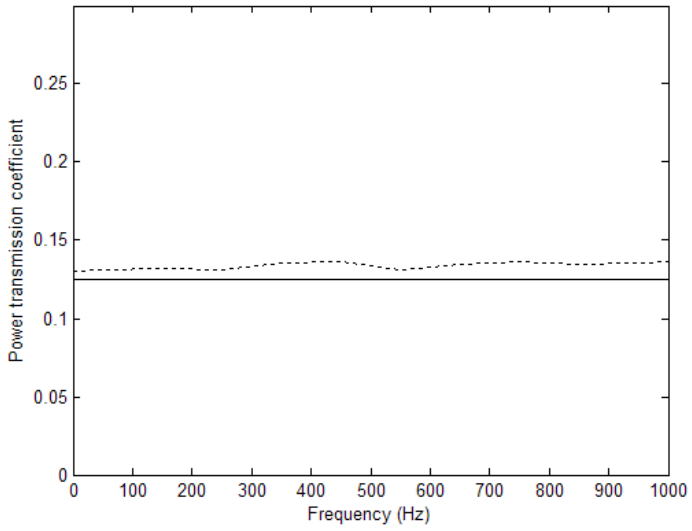

Figure 5.21. The power transmission coefficients $\langle \tau_{12} \rangle$ found using the hybrid approach (dotted line), and predicted from equation (5.13) resulting in $\tau_{12} = 0.125$ (solid line), for a frequency range from 1 Hz to 1 kHz.

5.5.4 7-plate structure results

Figures 5.22 to 5.24 present the energy levels of plates 2, 4 and 7 respectively. The energy levels were found using the hybrid approach, the waveguide analytical method and SEA techniques for a frequency range up to 1 kHz. The conventional SEA equations give a good approximation of the mean energy levels in this low frequency range, whilst the hybrid approach appears to underestimate the mean energy levels.

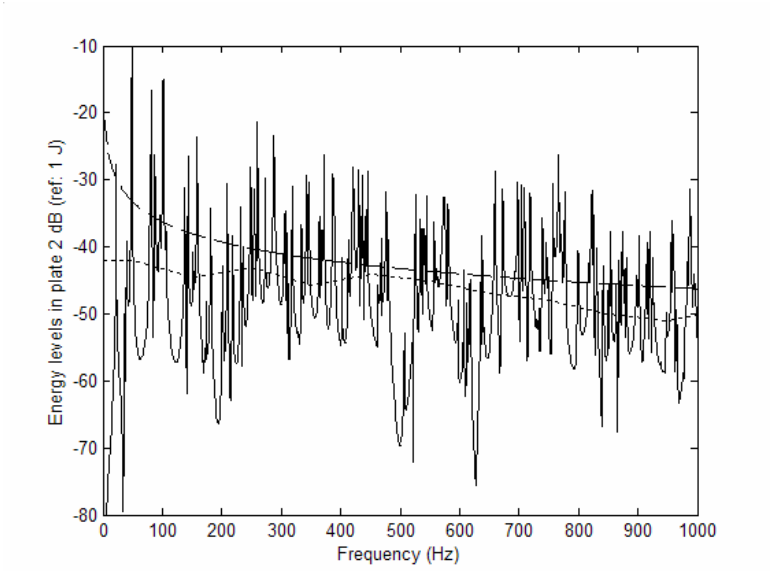

Figure 5.22. Energy levels in plate 2 of the 7-plate structure using the analytical waveguide method (solid line), SEA (dashed line), and the hybrid approach (dotted line), for a frequency range from 1 Hz to 1 kHz.

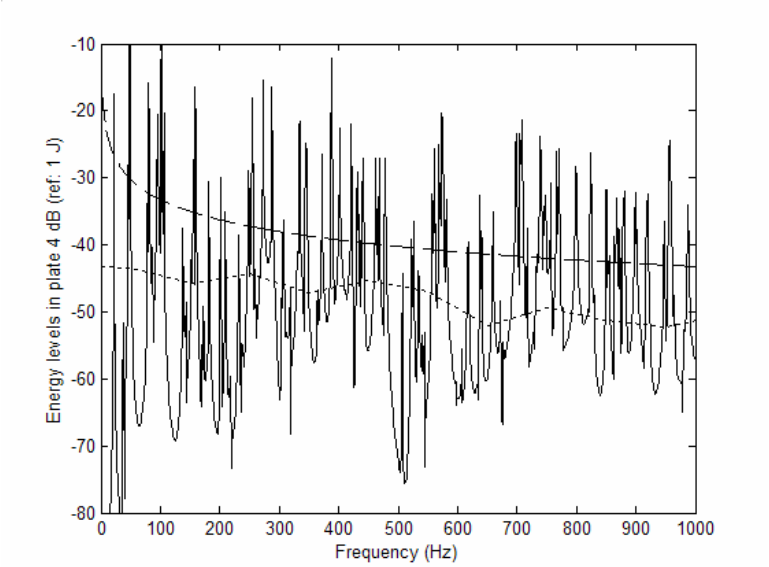

Figure 5.23. Energy levels in plate 4 of the 7-plate structure using the analytical waveguide method (solid line), SEA (dashed line), and the hybrid approach (dotted line), for a frequency range from 1 Hz to 1 kHz.

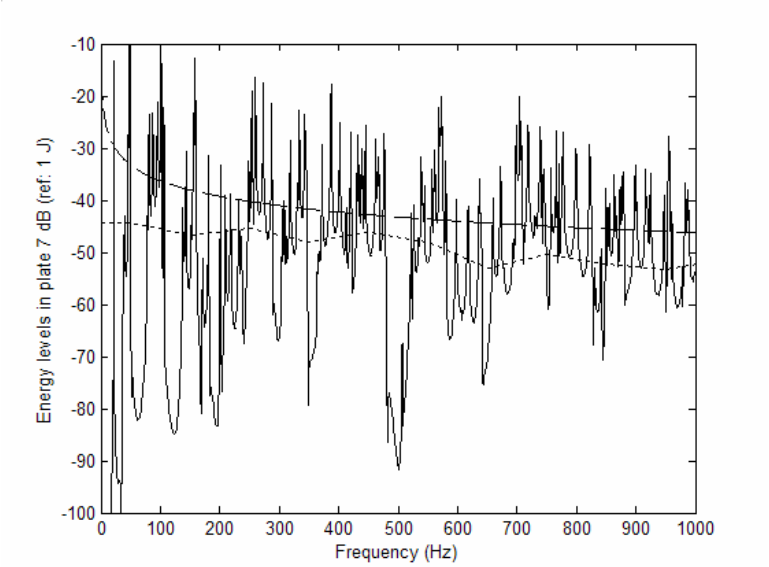

Figure 5.24. Energy levels in plate 7 of the 7-plate structure using the analytical waveguide method (solid line), SEA (dashed line), and the hybrid approach (dotted line), for a frequency range from 1 Hz to 1 kHz.

The energy levels of plates 2, 4 and 7 of the 7-plate structure for a frequency range from 5 to 6 kHz are presented in Figures 5.25 to 5.27 respectively. The results again show that in this mid frequency range, SEA tends to overestimate the energy levels in the plates. The figures also show that the energy levels using conventional SEA becomes nearly a straight line due to a greater population of modes at this frequency range. The hybrid approach clearly follows the trend of the frequency response function, although it appears to underestimate the mean energy levels in the plates.

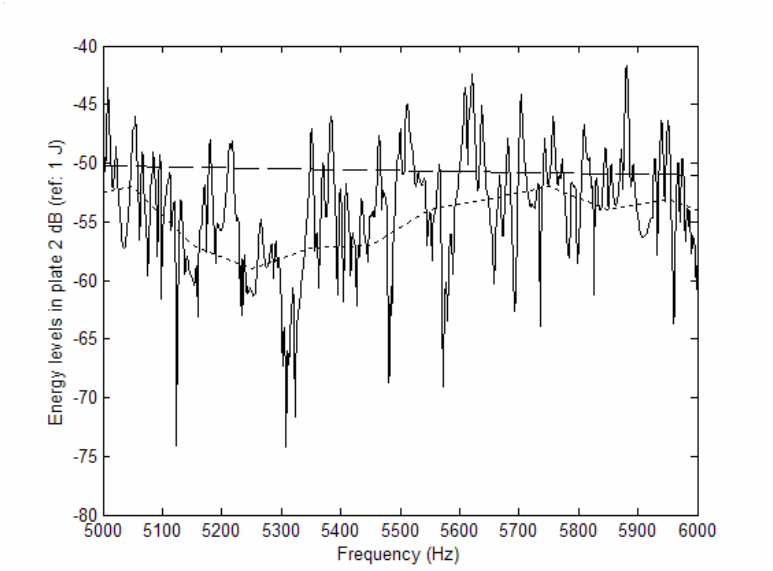

Figure 5.25. Energy levels in plate 2 of the 7-plate structure using the analytical waveguide method (solid line), SEA (dashed line), and the hybrid approach (dotted line), for a frequency range from 5 kHz to 6 kHz.

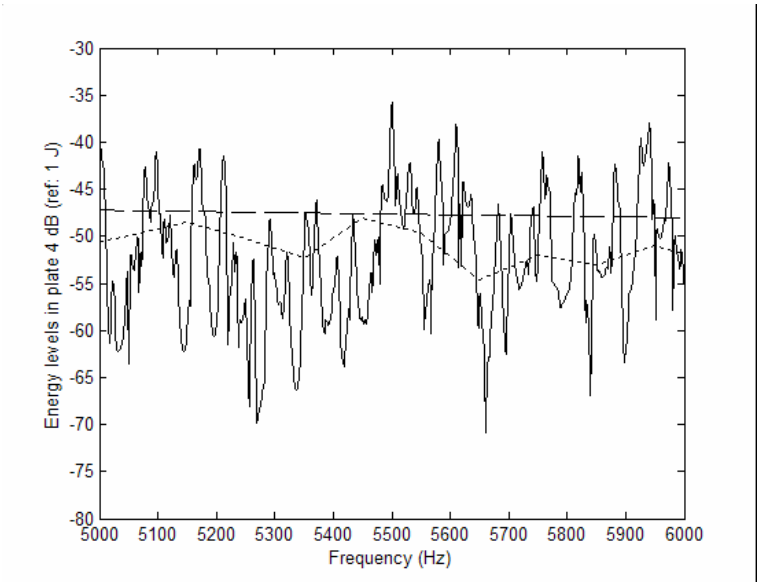

Figure 5.26. Energy levels in plate 4 of the 7-plate structure using the analytical waveguide method (solid line), SEA (dashed line), and the hybrid approach (dotted line), for a frequency range from 5 kHz to 6 kHz.

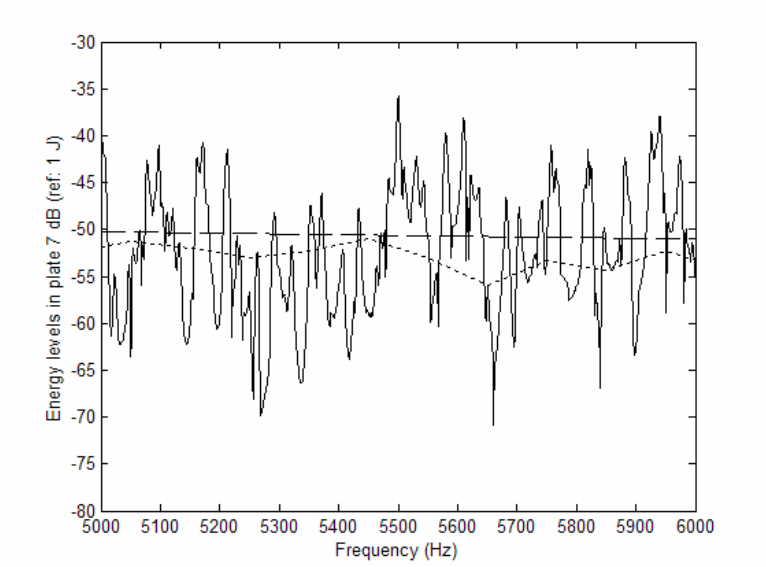

Figure 5.27. Energy levels in plate 7 of the 7-plate structure using the analytical waveguide method (solid line), SEA (dashed line), and the hybrid approach (dotted line), for a frequency range from 5 kHz to 6 kHz.

This chapter presents preliminary results obtained from a hybrid approach in which the SEA parameters corresponding to the input power and coupling loss factors were obtained from an exact analytical waveguide method. The investigation focussed on finite plates joined together at right angles. Although these structures have been extensively studied, the intention of this investigation was to initially investigate the accuracy of the hybrid approach and the SEA estimates. Further work to validate the mean energy levels using conventional SEA equations can be performed in the higher frequency range with the inclusion of in-plane vibration.

CHAPTER 6

SUMMARY AND RECOMMENDATIONS

6.1 Summary

In this thesis, the vibrational energy transfer between coupled plates is examined for L, T and X-shaped plates. An analytical waveguide method is used to model the response of the systems. A hybrid technique using the analytical waveguide method and statistical energy analysis (SEA) was developed, in order to accurately predict the plate mean energy levels at higher frequencies, and to validate the conventional SEA results. The analytical waveguide model was used to determine the SEA parameters corresponding to the input power and coupling loss factors. L, T and X-shaped plates are examined, as well as a built up structure consisting of seven plates. The mean energy levels of the individual plates predicted using SEA were compared with those modelled using the hybrid technique. Compared with the results from the hybrid approach, the energy levels predicted in each plate using the conventional SEA equations appear to overestimate the mean energy levels in the plates. At higher frequencies, the results showed that SEA produces more accurate results but still tends to overestimate the energy levels. The analytical study also showed that the hybrid approximation gave more accurate results over the entire frequency range.

In addition, analysis is performed using the analytical waveguide method to investigate active vibration control of low resonance frequencies in the structures. An analytical and

experimental investigation of the dynamic response characteristics of a series of rectangular plates coupled together at right angles and subject to point force excitation has also been conducted. The plate structures investigated included L, T and X-shaped configurations. Feedforward active control of the flexural waves in the coupled plates was investigated using single and multiple control forces and error sensors. The number and location of the control forces and error sensors to actively attenuate the frequency response was investigated. In addition, the effect of driving the control forces dependently and independently on the control performance was compared. Results indicated that using two control forces to minimise the vibrational response at two error sensors, global attenuation of the primary frequency response was achieved, as well as global attenuation of the plate structure at a discrete resonance frequency. At arbitrary force and sensor locations, higher attenuation levels were achieved using independently driven control forces compared to dependently driven control forces. Significant attenuation was also achieved when a single control force and a single error sensor were placed in a symmetrical arrangement on the coupled plates with respect to the primary force location and the simply supported boundary conditions. This corresponded to an error sensor location at the midway point along the width of the plate. Under this symmetrical control arrangement, the control force amplitude was always unity. When the control arrangement was not symmetrical with respect to the primary force location, the control force amplitude was found to vary with frequency, and the control performance deteriorated. An experimental rig was constructed, and the experimental active control results were found to be very consistent to the results obtained analytically. The results also indicate that when a practical vibration problem arises and a symmetrical one control force one error sensor control set-up is possible, it

could be assumed that the control force amplitude would equal to the primary control amplitudes at all frequencies. The signal from a primary force gauge could be used to drive the control shaker, and therefore a complex controller would not be required.

6.2 Recommendations

The mean energy levels have been calculated using conventional SEA equations and the hybrid approach. In addition to the mean energy levels, it would be of interest to investigate and compare the variance of the SEA and hybrid predictions. Future work could also involve extending the waveguide model, SEA equations and hybrid method to include in-plane motion, as in-plane vibration becomes more significant in the high frequency range, and at large distances from the source to the receiver through several intervening junctions. Future work could also include investigating more irregular structures, and experimental verification of the SEA results.

BIBLIOGRAGHY

[1] R. Szilard, (1974) *Theory and Analysis of Plates*, Classical and Numerical Methods, Prentice-Hall Inc., New Jersey.

[2] S. Timoshenko and S. Woinowsky-Krieger, (1959) *Theory of plates and shells, 2nd ed.,* McGraw-Hall Book Company, Inc., New Jersey.

[3] C. Wang, (1953) *Applied Elasticity*, McGraw-Hall Book Company Inc., New York.

[4] A. Leissa, (1993) *Vibrations of plates,* Acoustical Society of America through the American Institute of Physics, New York.

[5] S. V. Budrin and A.S. Nikiforov, (1964) "Wave transmission through assorted plate joints", *Soviet Physics – Acoustics,* **9**, 333-336.

[6] C. Boisson, J. L. Guyader, P. Millot, and C. Lesuer, (1982) "Energy transmission in finite coupled plates, Part II: Application to an L shaped structure", *Journal of Sound and Vibration,* **81**, 93-105.

[7] L. Cremer, M. Heckl and E. E. Ungar, (1988) *Structure-Borne Sound 2nd ed.* Springer-Verlag, Berlin, New York.

[8] R. S. Langley and K. H. Heron, (1990) "Elastic wave transmission through plate/beam junctions", *Journal of Sound and Vibration*, **145**, 195-215.

[9] H. Kim, H. Kang and J. Kim, (1994) "Transmission of bending waves in inter-connected rectangular plates", *Journal of the Acoustical Society of America,* **96**, 1557-1562.

[10] J. Kim, H. Kim, H. Kang and S. Kim, "Effects of inplane modes in SEA on structure-borne noise transmission in ship structures", *Proceedings of the Fourth*

International Congress of Sound and Vibration, St. Petersburg, Russia, 217-222, June 24-27 (1996).

[11] J. M. Cuschieri and M. D. McCollum, (1996) "In-plane and out-of-plane waves power transmissions through L_plate junctions using the mobility power flow approach", *Journal of the Acoustical Society of America,* **100**, 857-870.

[12] N. H. Farag and J. Pan, (1998) "On the free and forced vibration of single and coupled rectangular plates", *Journal of the Acoustical Society of America,* **104**, 204-216.

[13] B. A. T. Petersson, (1993) "Structural acoustic power transmission by point moment and force excitation, Part II: Plate-like structures", *Journal of Sound and Vibration,* **160**, 67-91.

[14] Z. H. Wang, J. T. Xing and W. G. Price, (2001) "An investigation of power flow characteristics of L-shaped plates adopting a substructure approach", *Journal of Sound and Vibration,* **250**, 627-648.

[15] P. Leug, (1936) "Process of silencing sound oscillations", US Patent 2 043 416.

[16] W. Redman-White, P. A. Nelson and A. R. D. Curtis, (1987) "Experiments on the active control of flexural wave power flow", *Journal of Sound and Vibration,* **112**, 187-191.

[17] E. F. Crawley and J. de Luis, (1989) "Use of piezoelectric actuators as elements of intelligent structures", *AIAA Journal*, **25**, 1373-1385.

[18] T. Bailey and J. E. Hubbard, (1985) "Distributed Piezoelectric-Polymer active vibrational control of a cantilevered beam", *AIAA Journal*, **6**, 605-611.

[19] J. L. Fanson and J. C. Chen, (1986) "Structural control by the use of piezoelectric active members", *Proceedings of NASA/DOD Control-Structures Interaction Conference,* NASA CP-2447, Part II.

[20] C. R. Fuller, R. J. Silcox, V. L. Metcalf and D. E. Brown, "Experiments on structural control of sound transmitted through an elastic plate", *Proceedings of American Control Conference*, Pittsburgh, Pennsylvania, 2079-2084, June 21-23 (1989).

[21] C. R. Fuller, (1990) "Active control of sound transmission/radiation from elastic plates. I. Analysis", *Journal of Sound and Vibration,* **136**, 1-15.

[22] B. T. Wang, C. R. Fuller and E. K. Dimitriadis, (1991) "Active control of noise transmission through rectangular plates using multiple piezoelectric or point force actuators", *Journal of the Acoustical Society of America,* **90**, 2820-2830.

[23] J. C. Lee and J. C. Chen, (1999) "Active control of sound radiation from rectangular plates using multiple piezoelectric actuators", *Applied Acoustics,* **57**, 327-334.

[24] C. H. Park and A. Baz, (1999) "Vibration control of the bending modes of plate using active constrained layer damping", *Journal of Sound and Vibration,* **227**, 711-734.

[25] R. L. Clark Jr. and C.R. Fuller, (1992) "Experiments on active control of structurally radiated sound using multiple piezoceramic actuators", *Journal of the Acoustical Society of America,* **91**, 3313-3320.

[26] C. Guigou, C. R. Fuller and K. D. Frampton, (1994) "Experiments on active control of acoustic radiation due to a clamped edge on a semi-infinite beam", *Journal of Sound and Vibration,* **169**, 503-526.

[27] S. J. Elliott and L. Billet, (1992) "Adaptive control of flexural waves propagating in a beam", *Journal of Sound and Vibration,* **163**, 295-310.

[28] R. L. Clark Jr, J. Pan and C. H. Hansen, (1992) "An experimental study of the active control of multiple-wave types in an elastic beam", *Journal of the Acoustical Society of America,* **92**, 871-876.

[29] X. Pan, and C. H. Hansen, (1995) "Active control of vibratory power transmission along a semi-infinite plate", *Journal of Sound and Vibration,* **184**, 585-610.

[30] N. J. Kessissoglou, (2001) "Active control of the wave transmission through an L-plate junction", *Journal of the Acoustical Society of America,* **110**, 267-277.

[31] A. J. Young and C. H. Hansen, (1994) "Active control in a beam using a piezometer actuator and an angle stiffener", *Journal of Intelligent Material Systems and Structures,* **54**, 536-549.

[32] A. J. Young and C. H. Hansen, (1996) "Control of flexural vibrations in stiffened structures using multiple piezoceramic actuators", *Applied Acoustics,* **49**, 17-48.

[33] P. Sergent and D. Duhamel, (1997) "Optimal placement of sources and sensors with the minimax criterion for active control of a one-dimensional sound field", *Journal of Sound and Vibration,* **207**, 537-566.

[34] X. Liu and J. Onoda, (1999) "Controller design for vibration suppression of slewing flexible structures", *Computers & Structures,* **70,** 119-128.

[35] H. Perez and S. Devasia, (2003) "Optimal output-transitions for linear systems", *Automatica*, **39**, 181-192.

[36] B. Jemai, M. N. Ichchou and L. Jezequel, (1999) "An assembled plate active control damping set-up: optimization and control", *Journal of Sound and Vibration,* **225**, 327-343.

[37] K. Hiramoto, H. Doki and G. Obinata, (2000) "Optimal sensor/actuator placement for active vibration control using explicit solution of algebraic riccati equation", *Journal of Sound and Vibration,* **229**, 1057-1075.

[38] S. J. Elliott, I. M. Stothers and P. A. Nelson, (1987) "A multiple error LMS algorithm and its application to the active control of sound and vibration", *IEEE Transactions on Acoustics, Speech and Signal Processing,* **ASSP-35**, 1423-1434.

[39] S. J. Elliott, M. Serrand and P. Gardonio, (2001) "Feedback stability limits for active isolation systems with reactive and inertial actuators", *Journal of Vibration and Acoustics*, **123**, 250-261.

[40] L. Benassi, S. J. Elliott and P. Gardonio, (2004) "Active vibration isolation using an inertial actuator with local force feedback control", *Journal of Sound and Vibration,* **276**, 157-179.

[41] R. H. Lyon and R. G. DeJong, (1995) *Theory and application of statistical energy analysis,* Butterworth Heinemann, Oxford, 2nd edition.

[42] M. P. Norton, (1989) *Fundamentals of noise and vibration analysis for engineers,* Cambridge University Press, Cambridge.

[43] J. Tratch Jnr, (1985) "Vibration transmission through machinery foundation and ship bottom structure", MSc Thesis in Mechanical Engineering, MIT.

[44] H. G. Davies, (1972) "Exact solutions for the response of some coupled multimodal systems," *Journal of the Acoustical Society of America,* **51**, 387-392.

[45] P. J. Remington and J. E. Manning, (1975) "Comparison of statistical energy analysis power flow predictions with exact calculations", *Journal of the Acoustical Society of America,* **57**, 374-379.

[46] B. L. Clarkson, (1991) "Estimation of the coupling loss factor of structural joints", *Journal of Mechanical Engineering Science (Proceedings of the Institute of Mechanical Engineering, Part C),* **205**, 17-22.

[47] R. S. Langley, (1990) "A derivation of the coupling loss factors used in statistical energy analysis", *Journal of Sound and Vibration,* **141**, 207-219.

[48] C. Simmons, (1991) "Structure-borne sound transmission through plate junctions and estimates of SEA coupling loss factors using FE method", *Journal of Sound and Vibration,* **144**, 215-227.

[49] J. A. Steel and R. J. M. Craik, (1993) "Statistical energy analysis of structure-borne sound transmission by finite element analysis", *Journal of Sound and Vibration,* **178**, 553-561.

[50] F. J. Fahy, (1994) "Statistical energy analysis: a critical overview", *Philosophical Transactions of the Royal Society, London* **A346**, 431-447.

[51] P. Hynnä, P. Klinge and J. Vuoksinen, (1995) "Prediction of structure-borne noise in large welded ship structures using statistical energy analysis", *Journal of Sound and Vibration,* **180**, 583-607.

[52] C. R. Fredö, (1997) "SEA-like approach for the derivation of the energy flow coefficients with a finite element model", *Journal of Sound and Vibration,* **199**, 645-666.

[53] B. R. Mace and P. J. Shorter, (2000) "Energy flow models from finite element analysis", *Journal of Sound and Vibration,* **233**, 369-389.

[54] A. C. Nilsson, (1977) "Attenuation of structure-borne sound in superstructures on ships", *Journal of Sound and Vibration,* **55**, 71-91.

[55] H. Yan, A. Parrett and W. Nack, (2000) "Statistical energy analysis by finite elements for middle frequency vibration", *Finite Elements in Analysis and Design,* **35**, 297-304.

[56] E. Luzzato and E. Ortola, (1988) "The characterization of energy flow paths in the study of dynamic systems using SEA theory", *Journal of Sound and Vibration,* **123**, 189-197.

[57] E. C. N. Wester and B. R. Mace, (1996) "Statistical energy analysis of two edge coupled rectangular plates: Ensemble averages", *Journal of Sound and Vibration,* **193**, 793-822.

[58] R. H. Lande, R. S. Langley, P. J. Shorter and J. M. Woodhouse, "Statistical energy analysis of a built-up structure excited through stiffening members", *Proceedings of the Tenth International Congress on Sound and Vibration*, Stockholm, Sweden, 1083-1090, 7-10 July (2003).

[59] B. R. Mace and J. Rosenberg, (1998) "The SEA of two coupled plates: An investigation into the effects of subsystem irregularity", *Journal of Sound and Vibration*, **212**, 395-415.

[60] R. S. Langley and P. J. Shorter, (2003) "The wave transmission coefficients and coupling loss factors of point connected structures", *Journal of the Acoustical Society of America,* **113** (4), 1947-1964.

[61] C. R. Fuller, S. J. Elliott and P. A. Nelson, (1996) *Active Control of Vibration*, Academic Press, London.

[62] J. B. Ochs and J. C. Snowdon, (1975) "Transmissibility across simply supported thin plates. 1. Rectangular and square plates with and without damping layers", *Journal of the Acoustical Society of America,* **58,** 832-841.

[63] S. D. Snyder and G. Vokalek, (1994) *EZ-ANZ User's Guide*, Adelaide Casual Systems Pty Ltd.

[64] D. G. Crighton, A. P. Dowling, J. E. Ffowcs Williams, M. Heckl and F. G. Leppington, (1992) *Modern methods in analytical acoustics*, Springer-Verlag London Ltd.

[65] B. R. Mace, (1994) "On the statistical energy analysis hypothesis of coupling power proportionality and some implications for its failure", *Journal of Sound and Vibration*, **178**, 95-112.

[66] A. J. Romano, P. B. Abraham and E. G. Williams, (1990) "A Poynting vector formulation for thin shells and plates, and its application to structural intensity analysis and source localization. Part 1: Theory", *Journal of the Acoustical Society of America,* **87**, 1166-1175.

[67] N. J. Kessissoglou, (2004) "Power transmission in L-shaped plates including flexural and in-plane vibration", *Journal of the Acoustical Society of America*, **115**, 1157-1169.

[68] A. N. Bercin, (1996) “An assessment of the effects of in-plane vibrations on the energy flow between coupled plates”, *Journal of Sound and Vibration,* **191**, 661-680.

APPENDIX A

$$
[\alpha_p]=\begin{bmatrix}
\left(-k_x^2-\nu k_y^2\right)e^{-jk_xL_{x1}} & \left(-k_x^2-\nu k_y^2\right)e^{jk_xL_{x1}} & \left(k_n^2-\nu k_y^2\right)e^{-k_nL_{x1}} & \left(k_n^2-\nu k_y^2\right)e^{k_nL_{x1}} & 0 & 0\\
jk_x\left(k_x^2+(2-\nu)k_y^2\right)e^{-jk_xL_{x1}} & -jk_x\left(k_x^2+(2-\nu)k_y^2\right)e^{-jk_xL_{x1}} & -k_n\left(k_n^2-(2-\nu)k_y^2\right)e^{-k_nL_{x1}} & k_n\left(k_n^2-(2-\nu)k_y^2\right)e^{-k_nL_{x1}} & 0 & 0\\
0 & 0 & 0 & 0 & 0 & 0\\
0 & 0 & 0 & 0 & 0 & 0\\
e^{-jk_xx_p} & e^{jk_xx_p} & e^{-k_xx_p} & e^{k_xx_p} & -e^{-jk_xx_p} & -e^{jk_xx_p}\\
-jk_xe^{-jk_xx_p} & jk_xe^{jk_xx_p} & -k_ne^{-k_xx_p} & k_ne^{k_xx_p} & jk_xe^{-jk_xx_p} & -jk_xe^{jk_xx_p}\\
-k_x^2e^{-jk_xx_p} & -k_x^2e^{jk_xx_p} & k_n^2e^{-k_xx_p} & k_n^2e^{k_xx_p} & k_x^2e^{-jk_xx_p} & k_x^2e^{jk_xx_p}\\
jk_x^3e^{-jk_xx_p} & -jk_x^3e^{jk_xx_p} & -k_n^3e^{-k_xx_p} & k_n^3e^{k_xx_p} & -jk_x^3e^{-jk_xx_p} & jk_x^3e^{jk_xx_p}\\
0 & 0 & 0 & 0 & -k_x^2-\nu k_y^2 & -k_x^2-\nu k_y^2\\
0 & 0 & 0 & 0 & -jk_x & jk_x\\
0 & 0 & 0 & 0 & 1 & 1\\
0 & 0 & 0 & 0 & 0 & 0
\end{bmatrix}
$$

$$
\begin{bmatrix}
0 & 0 & 0 & 0 & 0 & 0\\
0 & 0 & 0 & 0 & 0 & 0\\
0 & 0 & \left(-k_x^2-\nu k_y^2\right)e^{-jk_xL_{x2}} & \left(-k_x^2-\nu k_y^2\right)e^{jk_xL_{x2}} & \left(k_n^2-\nu k_y^2\right)e^{-k_nL_{x2}} & \left(k_n^2-\nu k_y^2\right)e^{k_nL_{x2}}\\
0 & 0 & jk_x\left(k_x^2+(2-\nu)k_y^2\right)e^{-jk_xL_{x2}} & -jk_x\left(k_x^2+(2-\nu)k_y^2\right)e^{jk_xL_{x2}} & -k_n\left(k_n^2-(2-\nu)k_y^2\right)e^{-k_nL_{x2}} & k_n\left(k_n^2-(2-\nu)k_y^2\right)e^{k_nL_{x2}}\\
-e^{-k_xx_p} & -e^{k_xx_p} & 0 & 0 & 0 & 0\\
k_ne^{-k_xx_p} & -k_ne^{k_xx_p} & 0 & 0 & 0 & 0\\
-k_n^2e^{-k_xx_p} & -k_n^2e^{k_xx_p} & 0 & 0 & 0 & 0\\
k_n^3e^{-k_xx_p} & -k_n^3e^{k_xx_p} & 0 & 0 & 0 & 0\\
k_n^2-\nu k_y^2 & k_n^2-\nu k_y^2 & -k_x^2-\nu k_y^2 & -k_x^2-\nu k_y^2 & k_n^2-\nu k_y^2 & k_n^2-\nu k_y^2\\
-k_n & k_n & jk_x & -jk_x & k_n & -k_n\\
1 & 1 & 0 & 0 & 0 & 0\\
0 & 0 & 1 & 1 & 1 & 1
\end{bmatrix}
$$

APPENDIX B

$$
[\alpha_p]=
\begin{bmatrix}
\left(-k_x^2-\nu k_y^2\right)e^{-jk_x L_{x1}} & \left(-k_x^2-\nu k_y^2\right)e^{jk_x L_{x1}} & \left(k_n^2-\nu k_y^2\right)e^{-k_n L_{x1}} & \left(k_n^2-\nu k_y^2\right)e^{k_n L_{x1}} & 0 & 0 & 0 & 0 \\
jk_x\left(k_x^2+(2-\nu)k_y^2\right)e^{-jk_x L_{x1}} & -jk_x\left(k_x^2+(2-\nu)k_y^2\right)e^{jk_x L_{x1}} & -k_n\left(k_n^2-(2-\nu)k_y^2\right)e^{-k_n L_{x1}} & k_n\left(k_n^2-(2-\nu)k_y^2\right)e^{k_n L_{x1}} & 0 & 0 & 0 & 0 \\
0 & 0 & 0 & 0 & \left(-k_x^2-\nu k_y^2\right)e^{-jk_x L_{x2}} & \left(-k_x^2-\nu k_y^2\right)e^{jk_x L_{x2}} & \left(k_n^2-\nu k_y^2\right)e^{-k_n L_{x2}} & \left(k_n^2-\nu k_y^2\right)e^{k_n L_{x2}} \\
0 & 0 & 0 & 0 & jk_x\left(k_x^2+(2-\nu)k_y^2\right)e^{-jk_x L_{x2}} & -jk_x\left(k_x^2+(2-\nu)k_y^2\right)e^{jk_x L_{x2}} & -k_n\left(k_n^2-(2-\nu)k_y^2\right)e^{-k_n L_{x2}} & k_n\left(k_n^2-(2-\nu)k_y^2\right)e^{k_n L_{x2}} \\
0 & 0 & 0 & 0 & 0 & 0 & 0 & 0 \\
0 & 0 & 0 & 0 & 0 & 0 & 0 & 0 \\
e^{-jk_x x_p} & e^{jk_x x_p} & e^{-k_n x_p} & e^{k_n x_p} & 0 & 0 & 0 & 0 \\
-jk_x e^{-jk_x x_p} & jk_x e^{jk_x x_p} & -k_n e^{-k_n x_p} & k_n e^{k_n x_p} & 0 & 0 & 0 & 0 \\
-k_x^2 e^{-jk_x x_p} & -k_x^2 e^{jk_x x_p} & k_n^2 e^{-k_n x_p} & k_n^2 e^{k_n x_p} & 0 & 0 & 0 & 0 \\
jk_x^3 e^{-jk_x x_p} & -jk_x^3 e^{jk_x x_p} & -k_n^3 e^{-k_n x_p} & k_n^3 e^{k_n x_p} & 0 & 0 & 0 & 0 \\
0 & 0 & 0 & 0 & jk_x & -jk_x & k_n & -k_n \\
0 & 0 & 0 & 0 & 0 & 0 & 0 & 0 \\
0 & 0 & 0 & 0 & -jk_x & jk_x & -k_n & k_n \\
0 & 0 & 0 & 0 & 0 & 0 & 0 & 0 \\
0 & 0 & 0 & 0 & j\left(k_x^3+k_p'^4/k_L\right) & -j\left(k_x^3+k_p'^4/k_L\right) & -\left(k_n^3+jk_p'^4/k_L\right) & -\left(k_n^3-jk_p'^4/k_L\right) \\
0 & 0 & 0 & 0 & -k_x^2-\nu k_y^2 & -k_x^2-\nu k_y^2 & k_n^2-\nu k_y^2 & k_n^2-\nu k_y^2
\end{bmatrix}
$$

$$
\begin{bmatrix}
0 & 0 & 0 & 0 & 0 & 0 & 0 & 0 \\
0 & 0 & 0 & 0 & 0 & 0 & 0 & 0 \\
0 & 0 & 0 & 0 & 0 & 0 & 0 & 0 \\
0 & 0 & 0 & 0 & 0 & 0 & 0 & 0 \\
0 & 0 & 0 & 0 & 0 & 0 & 0 & 0 \\
0 & 0 & 0 & 0 & \left(-k_x^2-\nu k_y^2\right)e^{-jk_x L_{x3}} & \left(-k_x^2-\nu k_y^2\right)e^{jk_x L_{x3}} & \left(k_n^2-\nu k_y^2\right)e^{-k_n L_{x3}} & \left(k_n^2-\nu k_y^2\right)e^{k_n L_{x3}} \\
-e^{-jk_x x_p} & -e^{jk_x x_p} & -e^{-k_n x_p} & -e^{k_n x_p} & \cdot jk_x\left(k_x^2+(2-\nu)k_y^2\right)e^{-jk_x L_{x3}} & -jk_x\left(k_x^2+(2-\nu)k_y^2\right)e^{jk_x L_{x3}} & -k_n\left(k_n^2-(2-\nu)k_y^2\right)e^{-k_n L_{x3}} & k_n\left(k_n^2-(2-\nu)k_y^2\right)e^{k_n L_{x3}} \\
jk_x e^{-jk_x x_p} & -jk_x e^{jk_x x_p} & k_n e^{-k_n x_p} & -k_n e^{k_n x_p} & 0 & 0 & 0 & 0 \\
k_x^2 e^{-jk_x x_p} & k_x^2 e^{jk_x x_p} & -k_n^2 e^{-k_n x_p} & -k_n^2 e^{k_n x_p} & 0 & 0 & 0 & 0 \\
-jk_x^3 e^{-jk_x x_p} & jk_x^3 e^{jk_x x_p} & k_n^3 e^{-k_n x_p} & -k_n^3 e^{k_n x_p} & 0 & 0 & 0 & 0 \\
1 & 1 & 1 & 1 & 0 & 0 & 0 & 0 \\
-jk_x & jk_x & -k_n & k_n & 1 & 1 & 1 & 1 \\
0 & 0 & 0 & 0 & 0 & 0 & 0 & 0 \\
j\left(k_x^3+k_p'^4/k_L\right) & -j\left(k_x^3-k_p'^4/k_L\right) & -\left(k_n^3-jk_p'^4/k_L\right) & \left(k_n^3+jk_p'^4/k_L\right) & -jk_x & jk_x & -k_n & k_n \\
j\left(k_x^3+k_p'^4/k_L\right) & -j\left(k_x^3-k_p'^4/k_L\right) & -\left(k_n^3-jk_p'^4/k_L\right) & \left(k_n^3+jk_p'^4/k_L\right) & -j\left(k_x^3+k_p'^4/k_L\right) & -\left(k_n^3+jk_p'^4/k_L\right) & \left(k_n^3-jk_p'^4/k_L\right) & 0 \\
-k_x^2-\nu k_y^2 & -k_x^2-\nu k_y^2 & k_n^2-\nu k_y^2 & k_n^2-\nu k_y^2 & 0 & 0 & 0 & 0 \\
 & & & & -k_x^2-\nu k_y^2 & -k_x^2-\nu k_y^2 & k_n^2-\nu k_y^2 & k_n^2-\nu k_y^2
\end{bmatrix}
$$

APPENDIX C

$$
[\alpha_p]=
\begin{bmatrix}
\left(-k_z^2-\nu k_y^2\right)e^{-jk_z z_{21}} & \left(-k_z^2-\nu k_y^2\right)e^{jk_z z_{21}} & \left(k_n^2-\nu k_y^2\right)e^{-k_n z_{21}} & \left(k_n^2-\nu k_y^2\right)e^{k_n z_{21}} & 0 & 0 & 0 & 0 & 0 & 0 & 0 & 0 & 0 & 0 & 0 & 0 \\
jk_z\left\{k_z^2+(2-\nu)k_y^2\right\}e^{-jk_z z_{21}} & -jk_z\left\{k_z^2+(2-\nu)k_y^2\right\}e^{jk_z z_{21}} & -k_n\left\{k_n^2-(2-\nu)k_y^2\right\}e^{-k_n z_{21}} & k_n\left\{k_n^2-(2-\nu)k_y^2\right\}e^{k_n z_{21}} & 0 & 0 & 0 & 0 & 0 & 0 & 0 & 0 & 0 & 0 & 0 & 0 \\
0 & 0 & 0 & 0 & 0 & 0 & 0 & 0 & 0 & 0 & 0 & 0 & 0 & 0 & 0 & 0 \\
0 & 0 & 0 & 0 & 0 & 0 & 0 & 0 & 0 & 0 & 0 & 0 & 0 & 0 & 0 & 0 \\
0 & 0 & 0 & 0 & 0 & 0 & 0 & 0 & 0 & 0 & 0 & 0 & 0 & 0 & 0 & 0 \\
0 & 0 & 0 & 0 & 0 & 0 & 0 & 0 & 0 & 0 & 0 & 0 & 0 & 0 & 0 & 0 \\
e^{-jk_z z_{21}} & e^{jk_z z_{21}} & e^{-k_n z_{21}} & e^{k_n z_{21}} & -e^{-jk_z z_{21}} & -e^{jk_z z_{21}} & -e^{-k_n z_{21}} & -e^{k_n z_{21}} & 0 & 0 & 0 & 0 & 0 & 0 & 0 & 0 \\
-jk_z e^{-jk_z z_{21}} & jk_z e^{jk_z z_{21}} & -k_n e^{-k_n z_{21}} & k_n e^{k_n z_{21}} & -jk_z e^{-jk_z z_{21}} & jk_z e^{jk_z z_{21}} & k_n e^{-k_n z_{21}} & -k_n e^{k_n z_{21}} & 0 & 0 & 0 & 0 & 0 & 0 & 0 & 0 \\
-k_z^2 e^{-jk_z z_{21}} & -k_z^2 e^{jk_z z_{21}} & k_z^2 e^{-k_n z_{21}} & k_z^2 e^{k_n z_{21}} & k_z^2 e^{-jk_z z_{21}} & k_z^2 e^{jk_z z_{21}} & -k_z^2 e^{-k_n z_{21}} & -k_z^2 e^{k_n z_{21}} & 0 & 0 & 0 & 0 & 0 & 0 & 0 & 0 \\
jk_z^3 e^{-jk_z z_{21}} & -jk_z^3 e^{jk_z z_{21}} & -k_n^3 e^{-k_n z_{21}} & k_n^3 e^{k_n z_{21}} & -jk_z^3 e^{-jk_z z_{21}} & jk_z^3 e^{jk_z z_{21}} & k_n^3 e^{-k_n z_{21}} & k_n^3 e^{k_n z_{21}} & 0 & 0 & 0 & 0 & 0 & 0 & 0 & 0 \\
0 & 0 & 0 & 0 & -jk_z & jk_z & -k_n & k_n & 0 & 0 & 0 & 0 & 0 & 0 & 0 & 0 \\
0 & 0 & 0 & 0 & 0 & 0 & 0 & 0 & 1 & 1 & 1 & 1 & 1 & 1 & 1 & 1 \\
0 & 0 & 0 & 0 & 0 & 0 & 0 & 0 & 0 & 0 & 0 & 0 & 0 & 0 & 0 & 0 \\
0 & 0 & 0 & 0 & 0 & 0 & 0 & 0 & -j\left(k_z^3-k_p^4/k_L\right) & -\left(k_z^3-jk_p^4/k_L\right) & \left(k_z^3+jk_p^4/k_L\right) & -j\left(k_z^3+k_p^4/k_L\right) & 0 & 0 & 0 & 0 \\
0 & 0 & 0 & 0 & 0 & 0 & 0 & 0 & 0 & 0 & 0 & 0 & j\left(k_z^3+k_p^4/k_L\right) & -j\left(k_z^3-k_p^4/k_L\right) & -j\left(k_z^3-k_p^4/k_L\right) & j\left(k_z^3-k_p^4/k_L\right) \\
0 & 0 & 0 & 0 & 0 & 0 & 0 & 0 & -k_z^2-\nu k_y^2 & k_n^2-\nu k_y^2 & k_z^2-\nu k_y^2 & -k_z^2-\nu k_y^2 & -k_z^2-\nu k_y^2 & k_z^2-\nu k_y^2 & k_z^2-\nu k_y^2 & -k_z^2-\nu k_y^2
\end{bmatrix}
$$

$$
\begin{bmatrix}
0 & 0 & 0 & 0 & 0 & 0 & 0 & 0 & 0 & 0 & 0 & 0 & 0 & 0 & 0 & 0 \\
0 & 0 & 0 & 0 & 0 & 0 & 0 & 0 & 0 & 0 & 0 & 0 & 0 & 0 & 0 & 0 \\
\left(k_n^2-\nu k_y^2\right)e^{-k_n z_{21}} & \left(k_n^2-\nu k_y^2\right)e^{k_n z_{21}} & 0 & 0 & 0 & 0 & 0 & 0 & \left(k_n^2-\nu k_y^2\right)e^{-k_n z_{21}} & \left(k_n^2-\nu k_y^2\right)e^{k_n z_{21}} & 0 & 0 & 0 & 0 & 0 & 0 \\
-k_n\left(k_n^2-(2-\nu)k_y^2\right)e^{-k_n z_{21}} & k_n\left(k_n^2-(2-\nu)k_y^2\right)e^{k_n z_{21}} & 0 & 0 & 0 & 0 & 0 & 0 & k_n\left(k_n^2-(2-\nu)k_y^2\right)e^{-k_n z_{21}} & -k_n\left(k_n^2-(2-\nu)k_y^2\right)e^{k_n z_{21}} & 0 & 0 & 0 & 0 & 0 & 0 \\
0 & 0 & \left(-k_z^2-\nu k_y^2\right)e^{-jk_z z_{21}} & \left(-k_z^2-\nu k_y^2\right)e^{jk_z z_{21}} & \left(k_n^2-\nu k_y^2\right)e^{-k_n z_{21}} & \left(k_n^2-\nu k_y^2\right)e^{k_n z_{21}} & 0 & 0 & 0 & 0 & \left(-k_z^2-\nu k_y^2\right)e^{-jk_z z_{21}} & \left(-k_z^2-\nu k_y^2\right)e^{jk_z z_{21}} & \left(k_n^2-\nu k_y^2\right)e^{-k_n z_{21}} & \left(k_n^2-\nu k_y^2\right)e^{k_n z_{21}} & 0 & 0 \\
0 & 0 & jk_z\left\{k_z^2+(2-\nu)k_y^2\right\}e^{-jk_z z_{21}} & -jk_z\left\{k_z^2+(2-\nu)k_y^2\right\}e^{jk_z z_{21}} & -k_n\left\{k_n^2-(2-\nu)k_y^2\right\}e^{-k_n z_{21}} & k_n\left\{k_n^2-(2-\nu)k_y^2\right\}e^{k_n z_{21}} & 0 & 0 & jk_z\left\{k_z^2+(2-\nu)k_y^2\right\}e^{-jk_z z_{21}} & -jk_z\left\{k_z^2+(2-\nu)k_y^2\right\}e^{jk_z z_{21}} & -k_n\left\{k_n^2-(2-\nu)k_y^2\right\}e^{-k_n z_{21}} & k_n\left\{k_n^2-(2-\nu)k_y^2\right\}e^{k_n z_{21}} & 0 & 0 \\
0 & 0 & 0 & 0 & 0 & 0 & 0 & 0 & 0 & 0 & 0 & 0 & 0 & 0 & 0 & 0 \\
0 & 0 & 0 & 0 & 0 & 0 & 0 & 0 & 0 & 0 & 0 & 0 & 0 & 0 & 0 & 0 \\
0 & 0 & 0 & 0 & 0 & 0 & 0 & 0 & 0 & 0 & 0 & 0 & 0 & 0 & 0 & 0 \\
0 & 0 & 0 & 0 & 0 & 0 & 0 & 0 & 0 & 0 & 0 & 0 & 0 & 0 & 0 & 0 \\
0 & 0 & 0 & 0 & 0 & 0 & 0 & 0 & 0 & 0 & 0 & 0 & 0 & 0 & 0 & 0 \\
k_n & -k_n & 0 & 0 & 0 & 0 & 0 & 0 & -k_n & k_n & 0 & 0 & 0 & 0 & 0 & 0 \\
-k_n & k_n & jk_z & -jk_z & k_n & -k_n & 0 & 0 & k_n & -k_n & jk_z & -jk_z & 0 & 0 & -k_n & k_n \\
0 & 0 & -jk_z & jk_z & -k_n & k_n & 0 & 0 & -k_n & k_n & -jk_z & jk_z & 0 & 0 & k_n & -k_n \\
0 & 0 & 1 & 1 & 1 & 1 & 0 & 0 & 1 & 1 & 0 & 0 & 0 & 0 & 0 & 0 \\
1 & 1 & 0 & 0 & 0 & 0 & 0 & 0 & 1 & 1 & 0 & 0 & 1 & 1 & 1 & 1 \\
0 & 0 & -j\left(k_z^3-k_p^4/k_L\right) & j\left(k_z^3+k_p^4/k_L\right) & \left(k_n^2+jk_p^4/k_L\right) & -\left(k_n^2-jk_p^4/k_L\right) & 0 & 0 & -j\left(k_z^3-k_p^4/k_L\right) & j\left(k_z^3+k_p^4/k_L\right) & \left(k_n^2+jk_p^4/k_L\right) & -\left(k_n^2-jk_p^4/k_L\right) & 0 & 0 & -\left(k_n^2-jk_p^4/k_L\right) & \left(k_n^2-jk_p^4/k_L\right) \\
-\left(k_n^2-jk_p^4/k_L\right) & \left(k_n^3+jk_p^4/k_L\right) & 0 & 0 & 0 & 0 & 0 & 0 & -k_z^2-\nu k_y^2 & k_z^2-\nu k_y^2 & -k_z^2-\nu k_y^2 & k_z^2-\nu k_y^2 & k_z^2-\nu k_y^2 & -k_z^2-\nu k_y^2 & k_z^2-\nu k_y^2 & -k_z^2-\nu k_y^2
\end{bmatrix}
$$

PUBLICATIONS ORIGINATING FROM THIS THESIS WORK

J. Keir, N. J. Kessissoglou, and C. J. Norwood, "Active control of connected plates using single and multiple actuators and error sensors", *Journal of Sound and Vibration*, *in press, available on-line* (2004).

J. Keir, N. J. Kessissoglou, and C. J. Norwood, "An analytical investigation of single actuator and error sensor control in connected plates", *Journal of Sound and Vibration*, **271**, 635-649 (2004).

J. Keir and N. J. Kessissoglou, "An analytical investigation on active control of connected plates using multiple actuators and error sensors", *Proceedings of the Tenth International Congress on Sound and Vibration*, Stockholm, Sweden, 7-10 July 2003, 8 pages CD.

J. Keir and N. J. Kessissoglou, "Active control of T and cross shaped plates", *Proceedings of the Ninth International Congress on Sound and Vibration,* Florida, USA, 8-11 July 2002, 8 pages CD.

N. J. Kessissoglou and J. Keir, "A hybrid approach to predict the vibration transmission in ship structures using a waveguide method and Statistical Energy Analysis", *Proceedings of ACOUSTICS 2004, Australian Acoustical Society Annual Conference*, Gold Coast, 3-5 November 2004, pp. 587-592.